Impact of Uncertainties on the Climate-Optimized Aircraft Design

P. A. Bos (BSc)

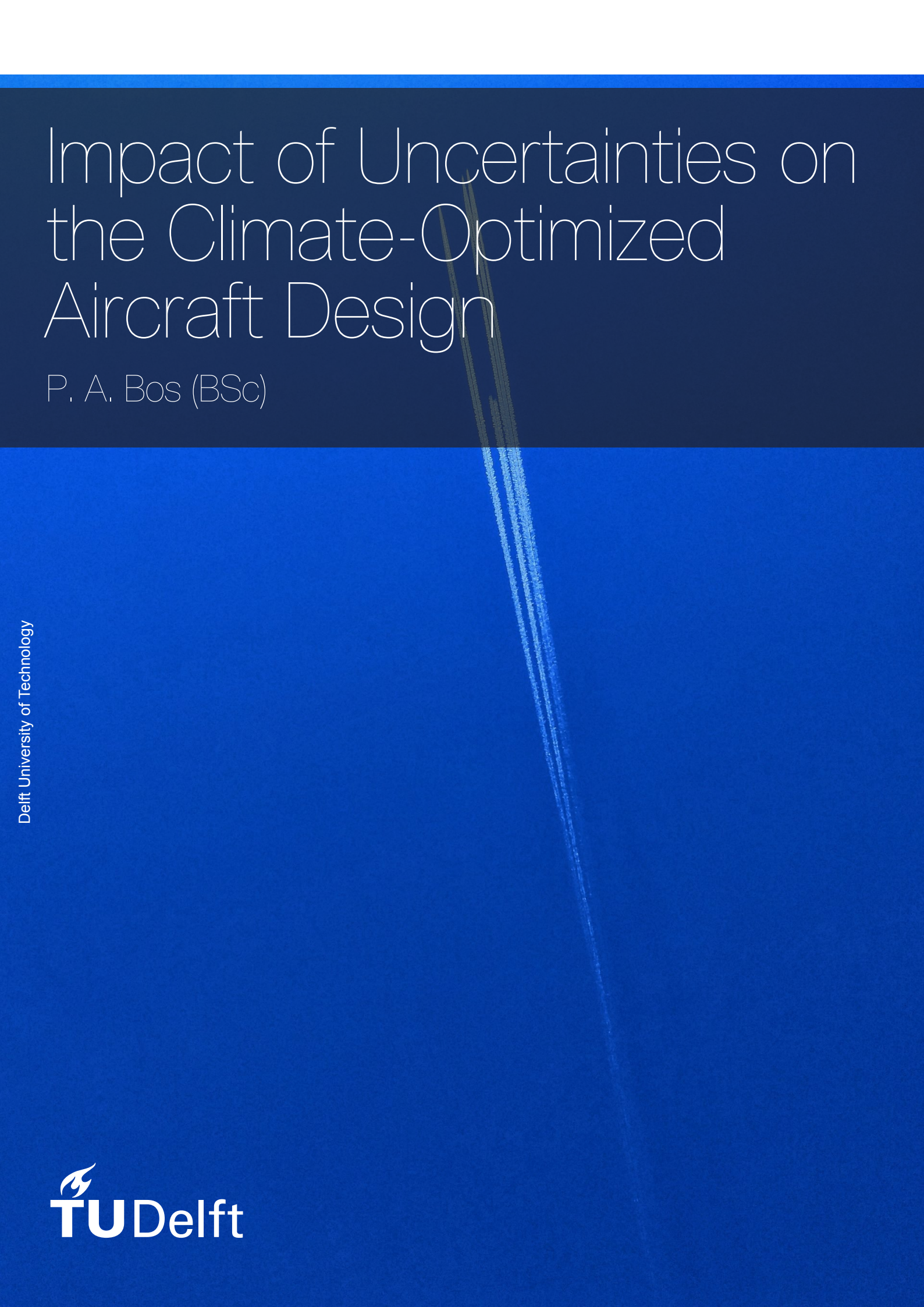

Delft University of Technology

TU Delft

Impact of Uncertainties on the Climate-Optimized Aircraft Design

by

P. A. Bos (BSc)

to obtain the degree of Master of Science
at the Delft University of Technology,
to be defended publicly on Friday March 18, 2022 at 9:00 AM.

Student number: 4438043

Thesis Committee:

Dr. G. La Rocca,	TU Delft, chair
Dr. R. Vos,	TU Delft, supervisor
P. Proesmans, M.Eng.,	TU Delft, supervisor
Dr. F. Yin,	TU Delft, examiner

An electronic version of this thesis is available at http://repository.tudelft.nl/.

TU Delft

Abstract

This report covers the investigation of impact of uncertainties on the multidisciplinary design optimization of a medium-range single-aisle turbofan aircraft for minimum global warming impact. The employed workflow for the investigation is a five step process, starting with the implementation of the deterministic climate impact model and carrying out of the design optimization for minimal climate impact. The second step involves the characterisation of uncertainties, where the uncertainties within the climate impact model are identified and quantified. The third step involves the uncertainty analysis, where Monte Carlo simulations are performed to estimate the variability in the average temperature reduction potential of the climate-optimized aircraft with respect to the cost-optimized aircraft. In the fourth step, a robust design optimization is carried out using a non-sorted genetic algorithm to minimize both the average temperature response and variability in average temperature response potential. The sensitivity analysis is carried as the last step using the Morris and variance-based Sobol methods, to identify what the key uncertain parameters are towards the uncertainty in climate impact of the aircraft designs.

Scientific uncertainty is identified within the linear climate impact model for the carbon impulse response function parameters, species radiative efficiencies, the NO_x and contrail altitude forcing factors, methane lifetime, species efficacies, and are all assigned a probabilistic description. Scenario uncertainty is identified in the future average global CO_2 atmospheric concentration projection, for which different realistic future scenarios are characterised. Carrying out the uncertainty analysis has shown that the average temperature response reduction potential of the climate-optimized aircraft is highly uncertain, having a 90% likelihood ranging between 17 and 98 % of the average temperature response of the cost optimized aircraft. This is primarily due to large variability in the estimation of contrail average temperature response. Although the robustness-based optimization did not allow to find any significant improvement in robustness for the climate-optimized aircraft, it did allow to identify an array of robust climate-optimized design solutions. From the sensitivity analysis, it was found that the uncertain parameters showing predominant influence on the output variability are the contrail-related radiaitive efficiency and forcing factors. Additionally, a variability of $\pm 50\%$ in average temperature response apportioned to CO_2 emissions was identified due to uncertainty related to future average global CO_2 concentration projections.

Acknowledgements

What has been a rich and eventful growth experience as a student at the TU Delft, will come to an end with the completion of this thesis. I hereby would like to give a token of appreciation to those who have helped me succeed throughout this journey.

First and foremost, I would like to thank my day-to-day supervisor, Pieter-Jan Proesmans. He has been there for me at all times, and his patient guidance and has been invaluable. A special thank you also goes to Roelof Vos for making this thesis possible, and for the feedback and guidance throughout the entire process.

Next I want to say thank you to Mom and Dad. Their unwavering support and love has kept my boat afloat at all times. I surely would not be where I am today without them.

And of course I must express my appreciation to all those who have been close to me throughout my student life in Delft... thank you. The boys at the library (my second home), they know who they are... Thanks for keeping my head high. Thank you also to my roommates at the KM. Although their sense of humour is dubious they never failed to brighten me up after long working hours. Thank you Tante Maaike, ever since I arrived to the Netherlands I never felt too far from home thanks to her presence. Also shout out to the entire Punch Basketball community. Hooping alongside these these wonderful people allowed me to keep my sanity. Thank you also to the ASH gang for being a second family during the integral time of my studies in Antwerp. My gratitude also goes to my fellow study mates from the FPP track, their support has been absolutely indispensable.

P. A. Bos (BSc)
Delft, March 2022

Contents

Nomenclature

Latin Symbols

cr	Cruise
h	Altitude [m]
H_0	Specific humidity [yrs]
k	Number of uncertain input parameters
M	Mach number
n	Monte Carlo sample size
p	Number of discrete levels in Morris One-At-A-Time method
r	Number of sample replications in Morris One-At-A-Time method
S	Wing area [m^2]
S_1	Sobol first-order sensitivity index
S_T	Sobol total-order sensitivity index
t_0	Initial year of climate impact evaluation
V	Velocity [m/s]
W	Weight [kN]
w	Fuel consumption [$g/kg - 1$]

Greek Symbols

χ_{CO2}	CO2 global atmospheric concentration
η	Propulsive Efficiency
μ	Mean
μ^*	Elementary effect of Morris method
σ	Standard deviaiton
$\tilde{\mu}$	Skeweness

Sub- and Superscripts

.25	Measured at quarter-chord
0	Sea-level condition or initial value
cr	Cruise
TO	Take-off condition

Acronyms

(TET	Turbine entry temperature [k]
ATR	Average Temperature Response
ATRRP	Average Temperature Response Reduction Potential
BPR	Bypass ratio
CDF	Cumulative Density Function
COC	Cash Operating Costs
CV	Coefficient of Variation
DI	Distribution index
DOC	Direct Operating Costs
ECCP	Experimental Clean Combustor Program
EI	Emission index of species [kg/kg]
EU	European Union
GA	Genetic Algorithm
GCAM	Global Change Assessment Model
GCM	Global Climate Model
GRA	Gray Relational Analysis
GSA	Global Sensitivity Analysis
HPC	High Pressure Compressor
IAM	Integrated Assessment Models
IPCC	Intergovernmental Panel of Climate Change
ISA	International Standard Atmosphere
LCM	Linear Climate Model
LOSU	Level Of Scientific Understanding
LPC	Low Pressure Compressor
LSA	Local Sensitivity Analysis
LTR	Linear Temperature Response Models
MCS	Monte Carlo Simulation
MDO	Multidisciplinary Design Optimization
MTOW	Maximum Take Off Weight [kg]
NSGA	Non-Sorted Genetic Algorithm
OPR	Overall pressure ratio
PDF	Probability Density Function
PR	Pressure ratio
QOI	Quantity Of Interest
RBDO	Robustness Based Design Optimization
RCP	Representative Concentration Pathway
RF	Radiative Forcing
RPK	Revenue Passenger Kilometer
SWV	Stratospheric Water Vapour
TOPSIS	Technique for Order of Preference by Similarity to Ideal Solution
UA	Uncertainty Analysis
UMDO	Uncertainty-Based Design Optimisation
UQ	Uncertainty Quantification
XDSM	Extended Design Structure Matrix

List of Figures

List of Tables

1

Introduction

The commercial aviation sector has experienced significant growth in the period between 1960 and 2018, with the revenue passenger kilometers growing from 109 to 8269 billion $kmyr^{-1}$ [37]. In 2018, the aviation emissions contributed to approximately 2.5% of annual global CO_2 emissions, and is predicted to reach to 22% by the year 2050 if no mitigation strategies are employed [3]. Due to the fast pace of growth of the aviation sector, aviation induced emissions are as well expected to increase significantly in the future. This growth is expected to have large impact on climate change, as both aviation CO_2 and the sum of non-CO_2 emissions lead to increased surface temperatures [38]. Hence, mitigation strategies for reducing the climate impact of novel aircraft technology and operation are increasingly relevant although commercial air traffic is today nearly exclusively cost driven [11]. When assessing new aircraft technology options, climate models allow for evaluating the associated marginal climate impact. Climate impact metrics are set as design objectives in the aircraft Multidisciplinary Design Optimization (MDO) study, thereby finding the optimal set of engine, air-frame and operational design variables that minimize the climate impact of the aircraft fleet.

Kroo et al. (2005) explored the possibility of using the climate impact in the MDO objective by using the cumulative CO_2 emissions (in kg) as the climate impact metric. NO_x emissions in landing and take off conditions are also considered as an additional objective, however are not considered in cruise conditions [35]. Metrics such as the Average Temperature Response (ATR) look a step further in the causal sequence from emission to climate impacts, and therefore are more relevant to policy makers. Dallara & Kroo (2011) incorporates the ATR in a aircraft climate optimization study, where the climate forcing impacts of NO_x and contrail cirrus are also considered. It was found that the climate impact is reduced considerably when the design cruise altitude and mach number are reduced. The minimal fuel design has little to no climate impact reduction compared to minimal direct operating cost (DOC) design, mainly as it flies in region where contrail formation is more probable [65]. Hence the benefit of using the ATR as a climate impact metric over the fuel consumption was proven. The study by Koch et al. (2016) performed a similar study using a more sophisticated climate model (AirClim) that also takes into account the location (longitude and latitude) of the emissions, and focuses on the route-specific trade-off between the climate impact reduction and increased DOC by varying cruise speeds and cruise flight altitudes[11]. The study by Proesmans (2021) further verifies the finding that using fuel burn as design objective does not give same results as setting minimal ATR in the MDO, and extends the studies by Dallara & Kroo and Koch by additionally incorporating engine design variables such as the overall pressure ratio (OPR) and turbine inlet temperature (TIT), as well as the contrail formation criteria [52].

The climate models used in the aforementioned aircraft optimization studies incorporate significant uncertainties. The uncertainties are mainly classified as scientific uncertainties that arise due to lack of scientific knowledge and inexact modelling of climate impacts [79]. These uncertainties affect the robustness of the optimization results obtained by Dallara & Kroo, Koch, and Proesmans ([11, 52, 65]) and hence affect the reliability in the Climate Impact Reduction Potential ($ATRRP$) compared to the minimal Direct Operating Cost (DOC) design. It has been shown that climate impact optimization is a conflicting design objective with respect to cash operating cost, through Pareto front representations in the study by Dallara & Kroo, Koch and Proesmans [11, 52, 65]. Hence in order for aircraft designers

to perform an effective and well-informed trade-off between cash operating cost and climate impact, it is important to know the extent in which the uncertainties affect the aircraft climate optimization. This knowledge also holds societal relevance, as the level of impact of uncertainties is an important point of consideration in the evaluation of feasibility of policy measures by aviation's regulatory bodies. Such policy measures include, for example, the inclusion non-CO_2 emissions in the Emissions Trading System of the EU, or the management of flight trajectories to avoid highly contrail-sensitive regions [1].

The investigation of impacts of uncertainties on the climate impact model output variation is also known as *Uncertainty analysis (UA)*. *Monte Carlo (MC)* simulations are carried out, where the deterministic climate impact evaluation is repeatedly performed on randomly sampled values of the uncertain inputs [72]. The aircraft optimization studies by Dallara & Kroo (2011) and Koch et al. (2016) both take uncertainties into consideration [11, 65]. Dallara & Kroo assumes probability distribution for input parameters of the climate model and performs a Monte Carlo analysis using the climate-optimized aircraft design to measure the probability distribution of the ATR reduction with respect to the cost optimized aircraft design. All model parameters and forcing factor functions are assumed to be uncertain [65]. Koch et al. similarly performs a Monte Carlo simulation using the AirClim tool to find the reliability of climate impact mitigation strategies, using probabilistic description of model parameters as outlined by Grewe & Stenke (2008) [18]. However, the uncertainty in the dependency of radiative forcing of the emission species on flight altitude is not taken into account [11]. The aforementioned studies use best estimate and uncertainty values of model parameters from literature that are not updated according to the the most recent changes in scientific understanding. This calls upon the need to produce a detailed summary of the most up to date best estimate and uncertainty values of the climate model parameters, together with the correlation factor and dependencies between model parameters. This highlights the first knowledge gap.

Using parameter best estimate and uncertainty quantification based on present day level of scientific understanding would also allow for carrying out sensitivity analysis where the importance of uncertain parameters are quantified. The use of the Global Sensitivity Analysis (GSA) method allows for quantifying individual parameter importance as well as the influence of parameter interactions on the output uncertainty. The utility of GSA is shown by the extensive application in a wide range of scientific research fields, including that of aviation climatic impact. Stettler et al. (2013) carried out Sobol' variance based SA to compute the contribution of each input parameter in the estimation of the UK airport emission inventory due to aircraft landing and takeoff operations [69]. Zhu et al. (2021) similarly performed GSA in the assessment of sources of uncertainty of aircraft pollutant emissions due to landing and takeoff operations around the Baiyun International Airport [84]. The application of GSA in the study of uncertainties in aircraft climate optimization has however not been performed to date. This highlights the second knowledge gap.

The integration of the uncertainty analysis within the multidisciplinary optimization framework (UMDO), looks at minimising the output sensitivity to variations (robustness-based UMDO) or looks at maximising the likelihood of performing a certain function [58]. Robustness-based optimization would allow for finding the design that has both maximal climate impact reduction potential and maximal probability of achieving that potential. For aircraft climate optimization this is relevant as the study by Koch et al. (2016) observed the inverse relationship between the ATR reduction and its variance in the Pareto front between ATR and DOC. This is because minimising the climate impact looks specifically at reducing the impact of emission species such as NO_x and contrails which both have a high degree of uncertainty [11]. Robustness-based design optimisation (RBDO) would therefore allow for more robust optimized conceptual designs to be further traded-off against other design objectives such as operating costs. UMDO application to aircraft climate-optimization has not been previously performed and hence highlights a further knowledge gap that this study aims to uncover.

In summary, previous research that has applied UA in the study of climate impact performance of conceptual aircraft designs consider uncertainty values that are not updated according to the the most recent changes in scientific understanding. Secondly, although the use of GSA has been applied in the study of emission inventories of aviation, it has not been applied in field of aircraft climate impact evaluation or optimization. A third identified knowledge gap is the inclusion of output uncertainties in the set of objective functions in the design optimisation framework. To address these knowledge gaps, this paper will seek to answer the following research questions and sub-questions:

1. Based on present day level of scientific understanding, what is the uncertainty in ATRRP of the climate optimized aircraft design?

   (a) What is the 90% likelihood range in the normalized ATRRP of the climate optimized aircraft design?
   (b) What is the confidence interval of the emission species normalized ATRRP for the climate optimized aircraft design?
   (c) How does the confidence interval in ATRRP vary throughout the different Pareto-optimal aircraft designs in the trade-off between ATR and DOC?

2. What aircraft design modifications can be made to improve the robustness of the climate optimized aircraft design?

   (a) For the set of Pareto optimal solutions of the multidisciplinary optimization of ATR and ATRRP standard deviation, what is the relationship between design variable values and the ATRRP variability?
   (b) What robust design solutions would provide optimal performance when further traded off with DOC?

3. What are the most relevant sources of uncertainty to the performance of the climate optimized aircraft design?

   (a) What is the composition percentage of the variance in ATR reduction attributed to the different uncertain inputs?
   (b) What is the sensitivity to variation in average global atmospheric CO_2 concentration projections within the year 2100?

Report Structure In Chapter 2, a background overview is provided of climate impact modelling, the sources of uncertainties associated with it, and their quantification methods. Chapter 3 outlines the general workflow delineated for the investigation of uncertainties, designed to methodically answer the aforementioned research questions. This chapter also contains a description of the deterministic multi-objective aircraft design optimization framework developed by Proesmans & Vos (2021) [52], upon which the current uncertainty study is based on. Chapter 4 provides an overview of the linear climate model employed in the evaluation of marginal climate impacts of the aircraft fleet, together with the comprehensive uncertainty characterisation where uncertainties within the climate model are identified and quantified. Chapter 5 outlines the methodology employed in the investigation of uncertainties, which is then verified in Chapter 6. The results of the uncertainty investigation are provided in Chapter 7, and finally the conclusions and a discussion is provided in Chapter 8

2

Overview of Climate Impact Modelling and Uncertainties

This chapter will serve as an introduction to the topic of climate impact modelling, and to the sources of uncertainties associated with it. It is to be emphasized that the area of focus is climate impact of kerosene powered commercial aviation. Section 2.1 gives an overview of the causal sequence from aviation emission to impacts, and discusses different metrics for quantifying those impacts. Section 2.2 looks more in detail at the individual emission species, and how they are assessed for a given fleet. Thirdly, Section 2.3 looks more broadly at the topic of sources of uncertainties in climate modelling, their different characterisations, and the framework used to quantify them.

2.1. Climate Impacts of Aviation Emissions

Throughout the optimization of the aircraft fleet performed in this study, one of the objectives is to minimize climate impact. The climate impact can measured at different stages of the causal sequence of aviation emissions to damages to environment and society as given in Figure 2.1 [79]. Initially aircraft emissions are quantified and changes in radiative forcing are measured. Changes in the climate are thereafter derived and lastly the environmental and social economic impacts. At every stage of the sequence, climate impact metrics can be formulated. Latter stages of the sequence hold higher relevance for policy makers, whilst it also becomes more difficult to accurately quantify the impacts and hence uncertainty also grows [65].

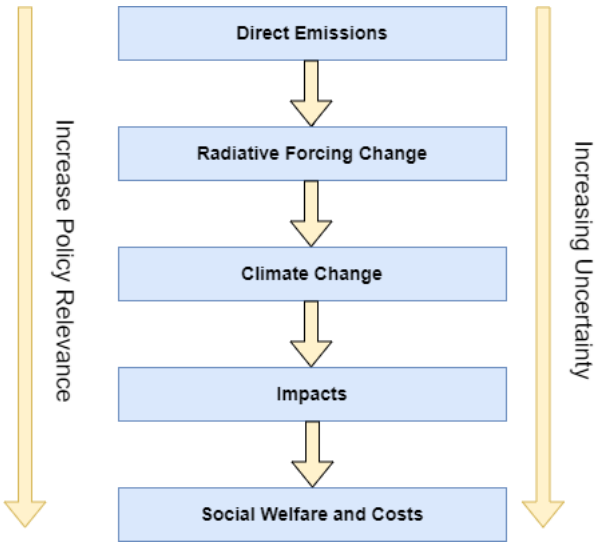

Figure 2.1: Causal Sequence of Emissions to Climate Impact [79]

The quantification of emissions is the first step of the causal sequence. The emissions alone are informative of the climate impact, however provide very incomplete picture thereof. The radiation balance is affected through different mechanisms according to the emission species. Species such as CO_2 and H_2O are referred to as 'direct greenhouse gases' as they absorb the radiation in the infrared range, and re-radiates it back to earth, increasing the net irradiance at the tropopause [44]. Species such as NO_x enhances the ozone and reduces methane atmospheric concentrations, both of which are direct greenhouse gases and hence affect the radiative balance. Therefore NO_x is considered an 'indirect greenhouse gas'. Another mechanism in which emission species affect the climate forcing is through the 'direct aerosol effect'. This occurs through the change in particle concentrations in the air due presence of particles in emissions such as soot and sulphate aerosols. Lastly, the radiative budget is affected via the aviation induced cloudiness, simply referred to as contrails. The presence of particles also affects the life cycle of clouds and hence affects the overall impact of clouds towards climate forcing [19]. Further discussion on each emission species is made in Section 2.2.

The second step in the causal sequence is the radiative forcing (RF) change. Radiative forcing can be defined as the change in net irradiance at the boundary between troposphere and stratosphere (i.e. the tropopause) caused by changes in atmospheric composition due to aviation emissions [19]. The use of radiative forcing concept is commonly used, including in the reports by the Intergovernmental Panel of Climate Change (IPCC), being the body of the United Nations dedicated to scientific research in the field of climate change [70]. Whilst the RF gives a direct indication of the magnitude of temperature change in the global mean context, the forcing from different species may not produce the same magnitude of temperature change, due to differences in the species' spatial distribution [79]. The RF concept alone works for well-mixed greenhouse gases with long perturbation lifetimes such as CO_2. For short-lived species, such as ozone, perturbation lifetime is small and the climate is directly affected on a more local scale. This characterises the main disadvantage of RF as a climate impact metric [19].

In order to consider impacts of both short and long-lived species, the Kyoto Protocol makes use of the GWP. The GWP compares the 100-year integrated RF for a given emission scenario and compares that to the forcing due to an equal mass of CO_2 emission. Its limitation lies in the fact that some emissions, in specific contrails, are not solely function on the amount of emissions alone. Short lived emissions are also less effectively evaluated using the GWP due to their very short lifetimes [79].

Computing the temperature change from the computed radiative forcing allows to go a step further in the causal sequence of emission to impacts. The temperature response depends on the spatial distribution of the radiative forcing. For example, for NO_x-induced methane or contrails, the radiative forcing is highly spatially heterogeneous. The temperature change may also be affected by the atmospheric adjustments that take place due to the emission species, such as aerosols causing rapid cloud coverage changes. In order to take into consideration the climate impact of of both short and long term emission species, the study by Proesmans & Vos utilize the Average Temperature Response (ATR) as the climate metric. This is defined as the average surface temperature response over 100 years by Grewe and Stenke (2016) [21]. This is expressed inEquation 2.1:

$$\text{ATR} = \frac{1}{H}\int_0^H \Delta T_s(t)dt \tag{2.1}$$

t is the time period in years after t_0, being the initial year when climate impact of the fleet is evaluated. The ATR metric has the advantage over the previously mentioned metrics such as the GWP as it limits the influence of the time horizon on the resultant climate impact. This is relevant to the current study as a balanced valuation of short and long term climate impact over the lengthy 100 year time horizon is looked for [52].

Quantifying societal costs and damages of impacts of climate change (4th and 5th stages of the causal sequence shown in Figure 2.1) provides a more comprehensive evaluation for policy makers by allowing for cost-benefit analysis of proposed policy measures. For the analysis of novel technology to introduce to the market, such as a new aircraft at a fleet-wise level, it would also allow for performing cost-benefit analysis when comparing with the fleet's operating cost. Current studies investigating the impact and damages however show large sensitivity to modelling uncertainty. Marais et al. (2008) [43] looks at damages of climate impact in six categories: agriculture, sea level rise, health, human settlements and ecosystems, other market sections affected by climate change, and non-market impacts. Limitations are identified arising from the overall complexity of the problem and difficulties of measuring impacts not commonly expressed in monetary terms. Mahashabde et al. (2010) [42] similarly estimates

the health and welfare costs of aviation through damage functions. Emphasis is however again made on the significant uncertainties present in the evaluation. Schwarz-Dallara (2011) furthermore mentions the challenge to quantify damages and the significant magnitude of the problem, in addition to the thin base of empirical studies [65]. For the aforementioned reasons, the study by Proesmans & Vos (2021) decides to no include the evaluation of cost of damages [52].

2.2. Emission Species

When looking at emission species of kerosene-fueled aviation, both CO_2 and non-CO_2 species are taken under consideration. The main non-CO_2 species of interest in terms of contribution to the global RF are NO_x, water, sulphate and soot aerosols, and contrail-induced cloudiness [37]. The formation and RF characteristics of each species is further discussed in this section.

CO_2 CO_2 is the most abundant carbon containing species emitted from the aircraft [38]. One of the main differences between CO_2 and non-CO_2 species is that the perturbation lifetime of CO_2 is in the order of decades, whilst for non-CO_2 species this is significantly shorter (e.g. hours for contrails, months for ozone, and years in the case of induced methane changes) [46]. As CO_2 is considered a well-mixed greenhouse gas, the climate impact is not considered to vary with emission altitude. CO_2 emissions cause a positive RF [38]. Calculating the CO_2 concentrations over time produced by a given emission scenario requires the use of a global carbon-cycle model. These range from high degrees of complexity for comprehensive Earth System Models (ESM) to Simple Climate Model (SCM), which approximate the results from the ESM using an impulse response function [37].

NO_x Nitrogen oxide emission cause photochemical effects, resulting in short term atmospheric increase in ozone and a long term decrease in lifetime and abundance of methane. The resultant long term methane reduction additionally induces a decrease in ozone and stratospheric water vapour levels (SWV). The short term NO_x effects induce a positive RF whilst the long term effects induce a reduction in RF. Overall, a net warming effect is produced, however the magnitude of this warming is less significant compared to CO_2 and contrails. Other effects from NO_x emissions include the short-term formation of nitrate aerosols and enhancement of sulphate aerosols, however due to the large number of uncertainties in studies regarding these effects, models typically omit them [37]. The RF efficiency of NO_x is shown to be strongly correlated with cruise altitude, hence flying at lower altitudes reduces the climate impact for a given amount of emissions. Furthermore, climate impacts can be reduced by lowering the amount of NO_x emissions, achieved by lowering engine core temperature. This would also decrease the thermal efficiency and hence requires a trade-off between fuel burn and NO_x emission. Predicting the RF response to NO_x emissions involves the use of Global Atmospheric Chemistry/Climate models to simulate the photochemical effects taking place. Such models prove particular sensitivity to NO_x levels in the background troposphere. It is as-well shown that significant correlations are present between long term and short term NO_x RFs, that can be represented by a correlation factor (p=-0.7) [37].

Water The emission of water vapour affects the background humidity levels in the lower stratosphere and thereby changes the radiative balance, making it a direct greenhouse gas. Water emissions overall have a warming effect on the climate. The water vapor RF is complicated due to sensitivity to altitude, latitude, seasonal changes in tropopause altitude, and the short perturbation lifetimes, thereby complicating its estimation [38]. At higher altitudes, larger water vapour has a longer residence time, making its impact more weighty. However as the overall contribution to aviation RF is relatively small, the altitude dependency is typically omitted in the simple climate models used to calculate the water RF.

Soot and Sulphate Aerosols (aerosol-radiation interaction) Particles in the form of soot, being a mixture of black carbon (BC) and organic carbon (OC), are directly emitted by the engines as a product of the condensation of unburnt hydrocarbons in the combustor. The soot aerosol emission works to contribute to a positive RF (warming effect) by absorbing short wave radiation. Sulfate aerosol form from the oxidation of sulfur in the ambient atmosphere after emission. Sulphate aerosols are formed from the oxidation of the sulfur in the fuel, and hence is function of the Fuel Sulfur Content (FSC). An FSC of 600 ppm is often assumed in calculations. The majority of the sulphate aerosols are emitted as SO2, whilst a small percentage is emitted as H2SO4 [37]. The percentage of conversion is quantified

by the conversion efficiency. Sulfate aerosol contributes to negative RF as it scatters incoming short wave radiation. Computation of aerosol RF are performed by different global aerosol models [37].

Soot and Sulphate Aerosols (aerosol-cloud interaction) Another radiative forcing mechanism which aerosols emission may potentially contribute to is through interaction with clouds. The formation of clouds is influenced by the nucleation of cloud droplets and ice crystals on aerosol particles. Best estimate of the RF of aerosol-cloud interaction are not considered in present-day evaluations of aviation climate impact, mainly due to the very large uncertainties in the model estimates. The source of uncertainty largely comes from the lack of knowledge of the ice nucleating capability of the aerosol particles. Studies do however indicate a net negative RF for the aerosol-cloud effects [37]. The distribution of a constant amount of cloud water over the more larger number of aerosol nuclei results in more, smaller cloud droplets. This increases the cloud droplet surface area, thereby increasing the albedo of the cloud and generating a negative RF [6].

Contrails Contrail cirrus, consisting of both persistent linear contrails and cirrus cloudiness arising from them, are clouds that form at high altitudes. These are composed of ice crystals that evolve in so called 'ice supersaturated regions'. Ice supersaturation refers to the condition where the water partial pressure lies above saturation level of ice. This requires sufficiently cold and moist atmospheric conditions [29]. Contrails are formed predominantly in the 8-13 km altitude range where ice supersaturation conditions are most frequent. The increase in cloudiness arising from persistent contrails contribute to radiative forcing. Overall, a net cooling effect is estimated for short wave radiation, while for long wave radiation a net warming effect is estimated. The effect at night is considered to only be warming [37]. Global Climate Models (GCMs) employ process-based contrail cirrus parameterizations are used to estimate magnitude of contrail climate impact. The cirrus life-cycle in these models is simulated from the persistent contrail formation and their spread, to the point where they become indistinguishable from natural cirrus [37]. Ice-supersaturated conditions along a flight track are variable in space and time in the troposphere and tropopause region, making the estimation of contrail formation difficult. Line-shaped contrails can be evaluated through direct observations in various regions of the world, similarly for regional cirrus clouds. This allows for correlations to be drawn between regional air traffic trends and contrail formation [54].

2.2.1. Assessment of Aviation Emissions

When assessing the climate impact of a past aviation pattern, the amount and location of each emitted species must be quantified. This allows for input to be generated for the climate model. The assessment of emissions has previously been done with the use of 'emission inventories', being three-dimensional gridded databases of aviation emissions compiled for given years. In addition, the gridded flown kilometers can be used as input for the contrail/cirrus models [38]. These inventory models take into account the global pattern of scheduled commercial flights and provide estimation of aircraft fuel burn and emissions on a global scale, using non-proprietary databases and methods [32]. Widely used emission inventories are AERO2K providing emissions for the year 2002 (Eyers et al. [14]), SAGE for years 2002-2005 (Kim et al., 2007 [32], and AEDT for year 2006 (Barrett et al. [4]). The three emission inventories are briedly described below:

- **SAGE**: CO, HC, and NO_x emission indices are modelled using the Boeing Fuel Flow Method 2 (BFFM2). BFFM2 is a comprehensible method developed based on experimental performance data obtained via full-scale engine tests at ground level [39]. On the other hand, CO_2, H_2O, and SOx emissions are modelled based on fuel composition using Boeing-derived emissions indices. The values derived by SAGE reflect the fleet-wide global averages between the years 2000 and 2005 [32].
- **AERO2k**: Emission indices are computed using publicly available engine data, for the year 2002.Special consideration is made on the particulate number in emission. Together with the distance flown parameter, offers foundation for estimation of the climate impact of contrail cirrus. CO_2 and H20, similarly to SAGE are modelled using fuel composition of Jet A-1 fuel. The EI of NO_x is estimated by means of fuel flow correlation method. This is done by means of measurements at various inlet conditions, provided by the ICAO emissions data bank. Similar correlation methods are employed for the EI of soot [14].

- **AEDT**: Aircraft fuel burn and emissions on a flight-by-flight basis, covering the majority of civil aviation computed for the year 2006. Similar to previously stated methods, CO_2 and H20 EIs are found making use of fuel composition values. For soot emissions, AEDT distinguishes the emission index below and above 3000ft. Hence includes altitude dependence. Sulphate aerosol emissions estimated using the Fuel Sulphur Content (FSC). The best estimate for the EI for SO4 made assuming a FSC is 600 ppm [4].

Emissions from CO_2, H_2O, sulphate aerosols scale directly with fuel burn and hence can be quantified with the use of Emission Indices (EIs), linearly relating the two components. This is because these species are solely based on the fuel composition of Jet A-1 Kerosene, the jet fuel predominantly used in commercial aviation. Emissions of NO_x, CO (soot) and HCs however do not scale directly with fuel burn because it depends also on the way the combustion is controlled. Different methods are therefore used. One option is the use of fuel flow correlation algorithms. For NO_x, these include the DLR-2 fuel flow method or the Boeing Fuel Flow Method-2. These algorithms are developed based on experimental performance data obtained via full-scale engine tests [39]. Fuel flow correlation algorithms are useful because they do not require access to proprietary information of the engine, as the only parameter used is the fuel flow at altitude, which is a 'nonproprietary' indicator of the engine thrust setting [10]. If access to engine proprietary information is available, simple empirical analytical functions are available as predictors for EI. The total pressure and total temperature measured at ground level is correlated with EI. A correction for difference in inlet pressure at ground level and at altitude is included with the presence of correction terms. In the case of the expression developed by the NASA Clean Combustor Program, the specific humidity is used as a correction term, as it varies with altitude [65].

2.2.2. Assessment of Contrail Formation

To predict contrail formation, the use of Schmidt-Appleman criteria is used. Contrail form when hot engine exhaust reaches saturation with respect to water vapour (meaning maximum amount of water vapour is contained for the given temperature) during the mixing process with ambient air. The mixing process involves a drop in temperatures and water vapour pressure, following a gradient G, according to the research Schumann (1996) [64]. This gradient is a function of the total pressure p, specific heat capacity c_p, ratio of molar masses of water and air, emission index of water vapour, EI_{H_2O}, propulsive efficiency η_p and specific combustion heat, Q [63]. The points used to evaluate if the criteria is fulfilled are the point at the end of the mixing line, T_{amb}, and the point where the vapour saturation line intersects with the critical mixing line, denoted T_{cf}. The critical mixing line represents the critical conditions for contrail formation [5]. The Schmidt-Appleman criteria states that contrail formation takes place if T_{amb} is smaller than T_{cf} [5].

For contrails to be persistent, the Schmidt-Appleman criteria is not sufficient. Persistence takes place if the condensed particles do not evaporate by time the exhaust is fully mixed. This is predicted by estimating whether the partial pressure of the mixed exhaust lies above the threshold of saturation of ice. This condition is namely called 'ice supersaturation'. Figure 2.2, from the study by Whelan et al. (2009) [78] visually show the mixing line, the vapour and ice saturation lines, the region where contrail formation takes place, and where contrail remains persistent.

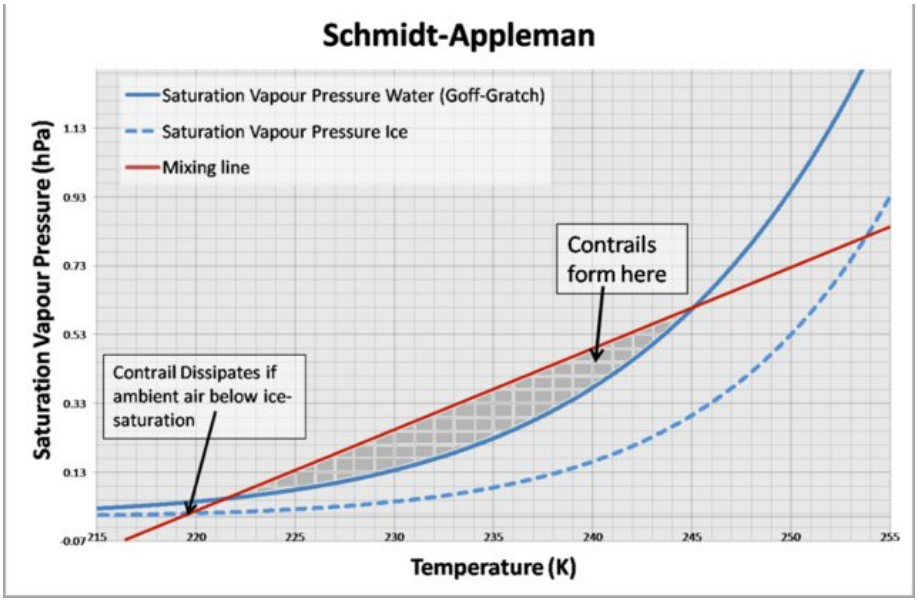

Figure 2.2: Schmidt-Appleman Criterion for contrail formation. Mixing line given in red, representing the mixing process of engine exhaust with ambient air. Saturation line of water vapour and ice given by bold and dotted blue lines respectively (Whelan et al. [78])

2.3. Uncertainties in Climate Impact Modelling

The uncertainty existing in the estimation of climate impacts can be characterised by the different sources of the uncertainty. Schwarz & Dallara (2011) [65] identify the three main sources to be scientific uncertainty, valuation uncertainty, and scenario uncertainty, each one elaborated below:

- **Scientific Uncertainty** is the main focal point of this study, and deals with the lack of scientific knowledge and inexact modelling of the climate impacts. The current scientific understanding of the potential effects on climate from aviation emissions can be expressed using the 'Level Of Scientific Understanding' (LOSU), appointing a subjective range from 'good', 'fair', 'poor' and 'very poor'. Wuebbles et al. (2010) determines the LOSU to be 'good' for long-lived carbon dioxide emissions, to 'fair', for the atmospheric chemistry and radiative effects from emissions of shorter-lived gases such as nitrogen oxides and water vapor, to 'poor' for the climate effects of cirrus clouds [79]. It must be noted that though the level of scientific understanding may be considered 'good', the confidence intervals may still be very large. This is the case as there is inherent variability in the system that is not captured by the Global Climate Models (GCMs)([61]. Further modelling uncertainty is induced by the inability of GCMs to resolve small, sub-grid scale features such as precipitation and evaporation, surface wind variability, jet streams, cloud physics and local atmospheric circulation patterns [16]. Alternatively, scientific understanding is quantified using a more objective framework by assigning numerical uncertainties using probability distribution functions (PDFs) [37].
- **Valuation Uncertainty** deals with the temporal weighing of emission impacts, and evaluates the relative importance of short term and long term impacts [79]. The use of the ATR climate metric averages out both short and long term effects, if a sufficiently long integration period is taken under consideration. Hence the valuation uncertainty has little significance for the climate assessment.
- **Scenario Uncertainty** refers to the uncertainty around the future climate responses to emissions. The most significant scenario uncertainty is the change in CO_2 background concentration over the next century, as this directly affects the forcing due to a unit CO_2 emission. Other sources of scenario uncertainty lie in the future forcing mechanisms and the species' radiative efficiencies. [79]. The future change in aero-engine technology or fuel composition is also a source of such uncertainty, however this study assumes the technology to be fixed throughout the operational lifetime of the fleet.

2.3.1. Modelling Uncertainty

As going further down the causal sequence from emissions to climate impacts, more comprehensive Gand computationally expensive modelling approaches are required. For evaluating the CO_2 concentration change, carbon cycle models are simulated using 'Earth System Models'. For the computation of radiative forcing due to emission species such as NO_x, contrails, 'Global Climate Models' are utilized, which simulate the microphysical processes taking place throughout the spread and interaction with the background atmosphere. The mean surface temperature change given a perturbation in the atmosphere's net solar irradiance requires the use of a comprehensive energy balance model. These models take into account the in-homogeneity of the climate forcer and the atmospheric responses to the emission species [37].

The usage of comprehensive climate models is accompanied by extremely large computational cost, making climate impact assessment on supercompters require weeks. This makes the forwards looking assessment of climate impact of aviation emissions prohibitive. Simplifications of the fully comprehensive climate models using using linearised relations are known as Linear Climate Models (LCMs) or Linear Response Models. LCMs significantly reduce the computational budget and allow for forwards looking climate assessment to be integrated in climate optimization studies. As only first-order effects are captured, they greatly simplify the physics and chemistry of aircraft-induced climate change. Effects of varying background concentrations, latitude and longitude, timing, and interaction with other pollutants not measured [65]. Hence additional modelling uncertainty is to be considered.

2.3.2. Quantification of Climate Model Input Parameters

Methods to quantify uncertainties in the input of a model vary according to the nature of the uncertainty. Uncertainty is mathematically classified as either 'Aleatory' or 'Epistemic'. Aleatory uncertainty is defined to be due to the inherent variation of system or environment under consideration. If an uncertainty is fully due to the inherent variation, it can be considered an irreducible uncertainty, meaning a higher level of scientific understanding would not reduce the level of uncertainty. As one theoretically has full knowledge of the variability of the system, aleatory uncertainty is typically modelled using a probabilistic framework. Epistemic uncertainty on the other hand is due to the inaccuracy present from lack of scientific knowledge. This is a subjective or reducible uncertainty and may include uncertainties about the model used to describe reality. Such uncertainties are typically modelled using uncertainty ranges with an upper and lower bound, without specifying a probability distribution [72].

Literature covering uncertainties in linear climate model parameters, summarised throughout the uncertainty characterisation performed Section 4.2, shows that although the nature of the uncertainty is both aleatory and epistemic, the probabilistic framework is predominantly used to describe the uncertainties. Hence this section will give further overview into classical probability theory. Expressing uncertainty in inputs using probabilistic framework allows for outputs to be represented similarly by a random variable, allowing statistics of the output to be estimated such as the expectation and variance after performing a forwards uncertainty propagation. Usage of probabilistic framework has its limitation in the fact that it theoretically impossible to model epistemic uncertainty using a PDF as it requires full knowledge of probability of outcomes. Inaccuracies in modelling the PDF will propagate into uncertainties in the resultant output uncertainties. In addition, knowledge is generally derived from several conflicting sources [72]. Hence, the use of probability theory can give a false sense of exactness [58].

Classical Probability Theory Probability of an event is defined as the number of cases the event occurred, over the total number of possible outcomes. An uncertain variable is represented as a *random variable*, being a measurable function from probability space into the real numbers [8]. The probability distribution of a continuous random variable, X, is expressed using the density function, $f(\cdot)$, defined as follows:

$$\mathbb{P}(a \leq X \leq b) = \int_a^b f_X(x)dx \tag{2.2}$$

Cumulative Density Function of X, $F_X(\cdot)$, is then written as:

$$F_X(x) = \int_{-\infty}^{x} f_X(u)du \tag{2.3}$$

Table 2.1 lists the probability density functions for different continuous distributions utilized in the uncertainty characterisation, later outlined in Chapter 4 [49]:

Type of Distribution	PDF	Parameters
Uniform	$f_X(x) = \frac{1}{b-a}$	a=lower bound b=upper bound
Normal	$f_X(x) = \frac{1}{\sqrt{2\pi\sigma^2}} exp\left[-\frac{1}{2}(\frac{x-\mu}{\sigma})^2\right]$	$\mu \in (-\infty, +\infty)$ σ > 0
Log normal	$f_X(x) = \frac{1}{x\sigma\sqrt{2\pi}} exp\left(-\frac{1}{2}(\frac{ln(x)-\mu}{\sigma})^2\right)$	$\mu \in (-\infty, +\infty)$ $\sigma > 0$

Table 2.1: Description of Common Probability Distribution Functions

For the log-normal distribution, the random variable, X, is written in terms of the standard normal variable, Z as follows:

$$X = e^{\mu+\sigma} \tag{2.4}$$

Hence μ and σ indicate the mean and standard deviation random variable's natural logarithm. Not to be mistakes with the mean and expectation of X as it is.

Joint Probability Distributions When one wishes to sample from input random variables U_1 and U_2 that are correlated, it is convenient to define a joint probability distribution, $f(u_1, u_2)$ such that:

$$P((X,Y) \in A) = \int\int_A f_U(u1, u_2) du_1 du_2 \tag{2.5}$$

The function of the joint probability distribution is to predict or control one random variable from another. The correlation between two random variables is often expressed in terms of the correlation coefficient, ρ. When ρ is zero, the variables are uncorrelated. The larger is ρ, the stronger is the linear correlation. The join probability distribution can be written out in terms of this correlation factor as well as random variable moments. For example, for two normally distributed correlated random variable the 'bivariate PDF' can be expressed as [15]:

$$f(u_1, u_2) = \frac{1}{2\sigma_1\sigma_2\pi\sqrt{1-\rho^2}} exp\left(-\frac{1}{2(1-\rho^2)}\left[\left(\frac{u_1-\mu_1}{\sigma_1}\right)^2 + \left(\frac{u_2-\mu_2}{\sigma_2}\right)^2 - 2\rho\frac{x_1-\mu_1}{\sigma_1}\frac{u_2-\mu_2}{\sigma_2}\right]\right) \tag{2.6}$$

The bivariate log-normal can be converted to the bivariate normal distribution by taking the natural log of each random variable [71].

2.3.3. Uncertainty Analysis in Aviation Climate Impact Mitigation Studies

Studies have been carried in the topic of climate impact mitigation potential for aviation, while also quantifying the uncertainties. Studies by Mahashabde et al. (2010), Dallara & Kroo (2011) [65], Koch et al. (2016) [11] and Dahlmann et al. (2016) look at policy options (e.g. climate-optimized aircraft design), and compare with baseline/reference scenarios [11, 27, 42, 65]. The uncertainty is quantified by looking at the probability distribution of the climate impact reduction compared to the reference case. For example in the study by Dallara & Kroo, the climate impact of the climate optimized aircraft design is compared with the minimum operating cost design (i.e. the standard case). Uncertainty analysis is carried out by looking at the probability distribution of the ATR reduction ($ATR_{ref} - ATR$), approximated using Monte Carlo sampling approach. Quantification of uncertainty in the ATR reduction is preferred over quantifying the absolute ATR of each design, as only the uncertainty relative to the difference between the different designs is represented [65].

When performing uncertainty analysis by comparing climate impact with baseline case, a Monte Carlo sampling of the output of both the baseline and reference case is required. Mahashabde et al. (2010) suggests making use of the paired sampling approach for the Monte Carlo simulation. This approach uses the same draw for both the baseline and policy option. Double counting uncertainties

is avoided, as the uncertainty is common to the climate impact of both the baseline and policy option. Hence uncertainty of the climate impact reduction is reduced [42].

3

Uncertainty Investigation Framework

This study aims to investigate the impact of the uncertainties on the climate impact optimisation. The three main steps of the investigation are the uncertainty analysis (UA), the robustness-based optimisation (RBDO), and the sensitivity analysis (SA). The general workflow combining the characterisation of uncertainties, the deterministic climate impact model, and the different steps of the uncertainty investigation is provided in Section 3.1. The investigation of uncertainty is performed on the conceptual aircraft design of a single-aisle medium-range turbofan aircraft optimized for minimal climate impact using the deterministic optimization framework. The multi objective optimization framework utilized in the study by Proesmans & Vos [52] is directly implemented in this research. Section 3.2 gives the outline of this deterministic optimization framework.

3.1. General Workflow

The general workflow employed for the uncertainty investigation in this study is shown in Figure 3.1. Step A includes defining the deterministic model used for evaluating the ATR for the given aircraft design. Step B looks at identifying the uncertain parameters in the climate impact model, and assigning a description of the probability that allows the uncertainty to be quantified. This allows the uncertainty quantification of inputs to be integrated together with the deterministic climate impacts model in the uncertainty analysis (UA) in step C, where statistics about the output are inferred. The output of interest is average temperature reduction potential (ATRRP), being the difference in ATR of the optimized aircraft with respect to the Direct Operating Cost (DOC)-optimized aircraft (given in Equation 3.1. This metric assumes the cost-optimized aircraft to be the reference aircraft, used to compare the performance of the climate-optimised aircraft. Both the climate- and cost- optimized conceptual aircraft designs are obtained using the deterministic multi-objective optimization framework described in Section 3.2.

$$\text{ATRRP} = \text{ATR}_{\text{cost-optimized}} - \text{ATR}_{\text{climate-optimized}} \tag{3.1}$$

With the uncertainty propagation model at hand, the robustness-based design optimization (RBDO) is performed next in step D, where solution having low sensitivity to variability in the system is aimed for. The RBDO is hence concerned with minimizing both the mean and the variability about the mean due to the uncertainties of the climate impact model. Robust solution are looked for because they are more likely to meet the climate impact target as level of scientific understanding increases over time, avoiding expensive redesigns [58]. Finally the sensitivity analysis can be performed on both the climate-optimized and the robust design solutions, to quantify the contribution of the individual sources of uncertainty towards the variability in climate impact reduction potential.

The workflow is cyclic, as the last step, the sensitivity analysis, directly informs about which of the characterised uncertainties have most influence on the uncertainty in the output of the system, and hence informs about where further uncertainty reduction work would most benefit aircraft design. After uncertainty reduction work is carried out, the uncertainty characterisation, uncertain analysis and robustness based design optimization can once again be repeated. Uncertainty reduction effort is however is outside the scope of the current study, hence only single iteration of the cyclic workflow is carried out. Section 3.2 will provide insight into the deterministic climate optimization framework,

being the first step of the general workflow, and is hence lays the foundation for the further uncertainty investigation.

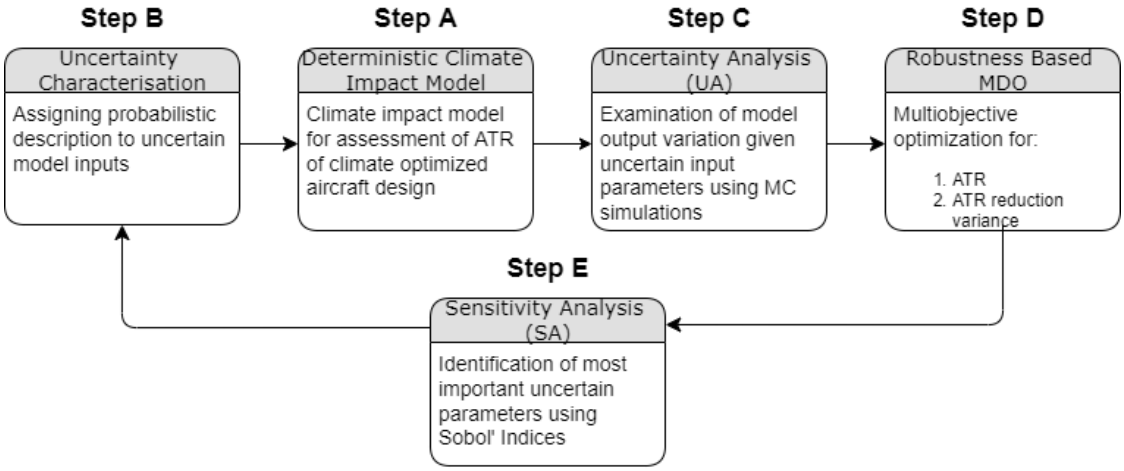

Figure 3.1: General workflow used for uncertainty investigation of the climate-optimized aircraft design (inspired by Mavromatidis et al. [47])

3.2. Deterministic Climate Optimisation Framework

This research works with the multiobjective optimization framework developed in the study by Proesmans & Vos (2021) [52], concerned with the conceptual design optimization for minimal climate impact design and costs of a single-aisle medium-range turbofan aircraft. The climate impact is quantified using the ATR, defined in Equation 2.1, and the cost is quantified using the DOC. The study by Proesmans & Vos [52] utilizes methods by Roskam [59] to compute the DOC. The operating costs are categorized into five components. The first is flight-related costs, including fuel, crew salary, and insurance. The second category is maintenance costs, including labor costs of airframe and engine engineers, and spare engine and airframe units. The third category is depreciation costs. Fourthly is the financing costs, assumed proportional to the DOC, and lastly is the operational fees, assumed proportional to the MTOW.

Both the ATR and the DOC are estimated for an envisioned time period of 65 years of fleet operation, between the years 2020 and 2085. A fixed productivity level is defined for each year. Productivity is quantified by the Revenue Passenger Kilometers per year (RPK), and is defined constant for the given year. The fleet size in a given year i, $N_{\text{AC, i}}$ is then derived from the productivity, RPK_i, according to the annual utilization of the aircraft, U_{Ann}, the block time of the mission, t_{bl}, the number of passengers per flight, and the block range according to Equation 3.2 [52]. A single aircraft is assumed an operational lifetime of 35 years.

$$N_{\text{AC, i}} = \frac{\text{RPK}_i}{\text{Capacity [pax/flight]} \cdot r_{\text{bl}}\text{[km]}} \cdot \frac{t_{\text{bl}}\text{[hrs]}}{\text{U}_{\text{Ann}}\text{[hrs]}} \tag{3.2}$$

Design Problem Formulation The single-objective optimization problem, for minimal climate impact or operating cost, is defined in Equation 3.3

$$
\begin{aligned}
\min_{\mathbf{x}} \quad & F(\mathbf{x}) = ATR(\mathbf{x}) \text{ or } DOC(\mathbf{x}) \\
\text{s.t.} \quad & W/S \leq \frac{1}{2}\rho_0 \left(\frac{V_{\text{app}}}{1.23}\right)^2 C_{L_{\text{max}}}, \\
& b \leq b_{\text{max}}, \\
& \text{TET}_{\text{TO}} \leq \text{TET}_{\text{TO,max}}, \\
& C_{L_{\text{cr}}} \leq \frac{C_{L_{\text{buffet}}}}{1.3} = \frac{0.86 \cdot \cos \Lambda_{0.25}}{1.3}, \\
& C_{L_{\text{max}}} \leq 2.8 \cdot \cos \Lambda_{0.25}, \\
& x_i^L \leq x_i \leq x_i^U \qquad \text{for} \quad i = 1, 2, ..., 10
\end{aligned}
\tag{3.3}
$$

The 10 design variables of the optimization are related to the conceptual design of the airframe, the engine, and the aircraft operation. The airframe design variables are the wing loading (W/S), the aspect ratio (A) and the maximum lift coefficient ($C_{L_{max}}$). The engine design variables are the bypass ratio (BPR), the fan, LPC and HPC pressure ratios ($\Pi_{fan}, \Pi_{\text{LPC}}, \Pi_{\text{HPC}}$), and the turbine entry temperature (TET). The operational design variables are the initial cruise altitude (h_{cr}) and the cruise Mach number (M_{cr}). The XDSM of the deterministic optimisation is shown in Figure 3.2. This allows the interfaces among components to be visualized by showing the data exchange, as well as the order in which the components are run, to be visualized.

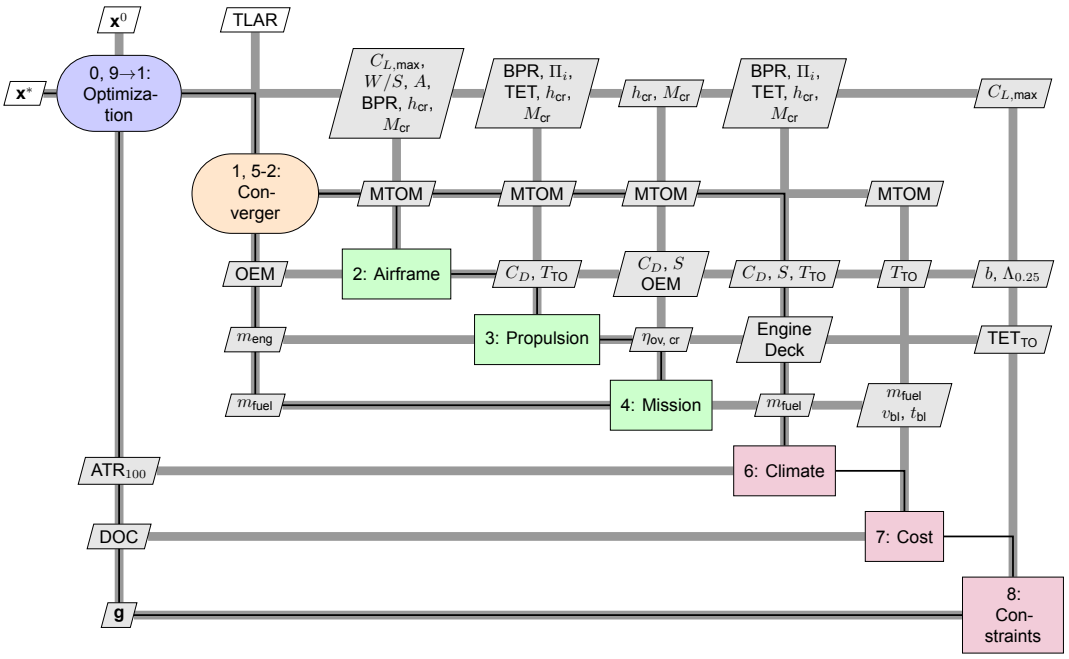

Figure 3.2: The extended design structure matrix of the deterministic conceptual aircraft design optimisation for minimal climate impact and cost as adapted from the study by Proesmans & Vos [52]

4

Climate Impact Model Uncertainty Characterisation

The first step in the investigation of uncertainties is the uncertainty characterisation. This involves the identification of uncertainties and the assignment of quantitative description. In order to do so, an overview of the Linear Climate Model (LCM) used to perform the climate impact evaluation of the aircraft fleet is firstly provided in Section 4.1. A summary of best estimate and uncertainty quantification of parameters identified in the LCM then follows in Section 4.2 follows.

4.1. Climate Impact Model Overview

The climate impact metric used for assessing the marginal climate impact of aviation operation of the proposed aircraft design is the Average Temperature Response (ATR), defined as the average global surface temperature response over the specified time horizon [20]. The ATR metric is advantageous for it provides balanced valuation of short and long term effects is not limited by the influence of time horizon [39]. A time horizon of 100 years is utilized, between the years 2020 and 2120. This is sufficient to capture the long term climate effects of the envisioned 65 years of fleet operation.

The forwards looking assessment of the ATR is performed using the LCM utilized in the study by Proesmans & Vos (2021) [52]. The model replicates first order globally averaged effects as computed using more comprehensive of the Global Climate Models (GCMs). Hence it assumes that the new fleet will have a spatially distributed routing similar to present-day commercial air traffic, which is largely concentrated in northern hemisphere mid-altitudes [27]. Dependency of the climate impact of NO_x-induced short- and long-lived O_3 as well as contrails on the emission altitude is directly incorporated. Effects of varying background concentrations, latitude and longitude, timing, and interaction with other pollutants however is not measured [65]. The emission species taken into consideration are CO_2, NO_x, H_2O, SO_4, soot, and contrails. The indirect emission species are the NO_x-induced CH_4, long- and short- lived O_3, and Stratospheric Water Vapour (SWV). This differs from the study by Proesmans & Vos (2021), where the inclusion of SWV as an indirect emission species was not considered. The inclusion of SWV was made possible by the quantification of its radiative efficiency, A_{SWV}, and species efficacy, f_{SWV}, in the study by Lee et al. (2021) [37]. An overview of the assumptions employed in the employed LCM are as follows:

- Constant background CO_2 level concentration.
- A constant methane lifetime [73]. As the key driver to the methane lifetime is methane itself, this implicitly assumes a constant methane background concentration.
- For short lived species, a perturbation lifetime of one year is assumed.
- Linear relationship between emissions and atmospheric concentration changes of species.
- Flight trajectory representative of global spatial average of historical global commercial flight pattern
- Physical climate responses will not change in the future, or in other words, that climate feedback mechanisms and all species' radiative efficiencies remain constant.

- Full knowledge of engine thermodynamic performance.
- Same aero-engine technology used on aircraft throughout operational lifetime.
- No degradation in aircraft performance over operational lifetime.
- Constant fuel composition throughout operational lifetime.
- Emissions during ground operations not accounted for.

The first step in the LCM is the mission analysis, where the amount of each emission species at each year of operation is computed, based on the mission profile, engine performance, and fuel consumption of the fleet. Section 4.1.1 gives insight into the methods employed in the mission analysis. The next step involves the computation of RF throughout the time horizon under consideration, as elaborated in Section 4.1.2, and finally the evaluation of the average global surface temperature change, summarized in Section 4.1.3.

4.1.1. Mission Analysis

The first step of the climate impact assessment is the mission analysis, where based on the flight envelope and fuel consumption at the different stages therein, the emissions are computed for each emission species. For CO_2, water vapour, and soot and sulphate aerosol emissions, this is assumed proportional to the fuel burn w_{fuel} and is evaluated via a constant emission index, EI, as shown in Equation 4.1:

$$\text{EI}_i = \text{EI}_i W_{\text{fuel}} \tag{4.1}$$

NO_x emission does not scale linearly with fuel burn. Instead, it is estimated using the semi-empirical analytical expression developed by NASA's Experimental Clean Combustor Program (ECCP) given in Equation 4.2. These correlations are designed to predict the EI for the engines of the GE90 engine family. The engine is representative of modern high bypass ratio, high overall pressure ratio turbofan [65]. The EI is correlated with power setting by measurement of NO_x emission at various throttle settings, thereby varying the total pressure and temperature ahead of the engine. The specific humidity factor, H_0 varies with altitude and hence serves as an altitude correction factor, allowing the expression to be used at every point in the mission profile [41].

$$\text{EI}_{NOx} = 0.0986 \cdot \left(\frac{p_{T3}}{101325}\right)^{0.4} - e^{T_{T3}/194.4 - H_0/53.2} \tag{4.2}$$

Contrail Formation Assessment At every point of the mission profile, whether a linear contrail is formed, and whether it persists, is assessed according the criteria explained in Section 2.2.2. Firstly is the Schmidt-Appleman criterion, met if the hot exhaust air reaches saturation with respect to water during the mixing process with the ambient air. This determines whether contrail formation takes place. Secondly is whether the static ambient temperature lies below 235 Kelvin. Thirdly, for contrail to be persistent, and hence for them to affect the earth's radiative budget, the partial pressure of the mixed exhaust air must lie in between the thresholds of saturation above ice and below that of water vapour [52].

4.1.2. Radiative Forcing Computation

After the mission analysis, the change in global radiative budget for the given amount of emission at every year of operation of the aircraft fleet is computed. The methodology used to obtain the RF response for the different species is summarised below.

Carbon Dioxide To compute the CO_2 concentration change and respective RF change due to CO_2 emission, the Simple Climate Model (SCM) by Sausen-Schumann (2000) [62] is used. This LTR model approximates the comprehensive carbon-cycle model by Maier-Raimer and Hasselmann (1987) by use of a Finite-amplitude Impulse Response Model (FaIR) [37]. This model is also referred to as the 'LinClim' model in literature. Firstly the concentration change of atmospheric CO_2 is computed from the emissions is a given year, E_{CO_2} according to Equation 4.3:

$$\delta\chi_{CO_2}(t) = \int_{t_0}^{t} G_{\chi_{CO_2}}(t-t') \cdot E_{CO_2}(t')dt', \text{ where } G_{\chi_{CO_2}}(t) = \sum_{i=1}^{5} \alpha_i \cdot e^{-t/\tau_i} \tag{4.3}$$

$G_{\chi_{CO_2}}$ represents the impulse response function based on coefficients τ_i and α_i representing the perturbation lifetime and strength of the response modes. The values of these parameters are provided by Sausen & Schumann (2000) [62]. The concentration change translates to the normalized RF change according to Equation 4.4, where $\chi_{CO_2,0}$ is the global CO_2 background concentration (in ppm).

$$\mathsf{RF}^*(t) = \frac{1}{\ln 2} \cdot \ln\left(\frac{\chi_{CO_2,0} + \delta\chi_{CO_2}(t)}{\chi_{CO_2,0}}\right) \tag{4.4}$$

Nitrogen Oxides For long-term NO_x effects, namely a depletion in methane and ozone, the RF is modelled according to Equation 4.5. The formulation includes a 'forcing factor' $s_i(h)$, which accounts for the altitude dependency of the species, further explained in Equation 4.1.2. The parameter τ_i is the perturbation lifetime of the species and A_i is coined the term 'radiative efficiency' and represents the change in RF per unit emission species, in this case being NO_x. For the effect of NO_x on long term Stratospheric Water Vapour (SWV) radiative forcing, Equation 4.5 can also be used, even-though not previously accounted for in the studies by Proesmans (2021) or Schwarz-Dallara (2011) [52] [65]. In addition, there is no estimation available for the forcing factor in literature for the RF of SWV.

$$\mathsf{RF}_i(t,h) = s_i(h) \int_{t_0}^{t} G_i(t-t') \cdot E_{NO\mathsf{x}}(t')dt', \text{ where } G_i(t) = A_i e^{-t/\tau_i} \text{ for } i = CH_4, O_{3\mathsf{L}} \tag{4.5}$$

For short-lived NO_x species, ozone level in troposphere and lower stratosphere is increased. The perturbation is assumed to only be active in the year of the emission. The RF response is then formulated as follows, where $\frac{\mathsf{RF}_{ref}}{E_{NO\mathsf{x}}}$ represents the radiative efficiency due to short-term ozone concentration changes:

$$\mathsf{RF}_{NO\mathsf{x}-O_{3,SL}}(t,h) = s_i(h)\left(\frac{\mathsf{RF}_{ref}}{E_{ref}}\right)_{NO\mathsf{x}-O_{3,SL}} E_{NO\mathsf{x}}(t)dt \tag{4.6}$$

Water, Soot and Sulphate Water, soot and sulphate all are short lived species and therefore their RF can be represented the same way as for short term NO_x effects in Equation 4.6. However in the case of water, soot and sulphate, the forcing factor $s_i(h)$ is equal to 1, as the altitude dependency is not included.

Contrails RF response for persistent contrails, consisting of linear contrails and cirrus cloudiness arising from them is formulated in Equation 4.7. RF forcing is expressed as a function of total stage contrail length, $L(t)$, a radiative efficiency parameter, $\frac{\mathsf{RF}_{\mathsf{ref}}}{\mathsf{L}_{\mathsf{ref}}}$, relating the RF to the distance flown, and once again a forcing factor $s_{contrails}(h)$. The total stage contrail length, $L(t)$, is evaluated during the mission analysis by assessing whether contrail formation takes place at each point throughout the mission profile. The criteria for contrail formation, as explained in paragraph 4.1.1, must all be satisfied in order for contrail formation to be assumed.

$$\mathsf{RF}_{contrails}(t,h) = s_{contrails}(h) \cdot \left(\frac{\mathsf{RF}_{\mathsf{ref}}}{\mathsf{L}_{\mathsf{ref}}}\right)_{AIC} L(t) \tag{4.7}$$

Forcing Factors The forcing factor, $s_i(h)$, is an altitude dependence unitless parameter defined for NO_x-induced short- and long-lived ozone and methane as well as contrails. This term accounts for the variation in RF per unit emission at a particular altitude, normalized by the fleet-wide average RF [65]. These functions are derived from measurements of the RF change due to perturbing air traffic by a small amount at each height in turn. This factor is derived for NO_x species, i, by normalizing its RF per emission as function of altitude, $\frac{\mathsf{RF}_i}{\mathsf{E}_{NO\mathsf{x}}}(h)$, by the distance-weighted RF per emission by applying Equation 4.8:

$$s_i(h) = \frac{\frac{\mathrm{RF}_i}{E_{NO_x}}(h)}{\int_0^\infty \frac{\mathrm{RF}_i}{E_{NO_x}}(h) l(h) dh} \tag{4.8}$$

$RF/E_{NO_x}(h)$ is estimated from data of global RF per unit emission at various altitudes in the study by Kohler et al. (2008). The RF computations are performed for a fleet having the same air traffic pattern as commercial aviation in the year 2002 according to the AERO2K emission inventory [33]. This same air traffic pattern is used to compute $l(h)$, being the ratio of the distance flown at given altitude to the total distance flown by the air traffic. Data is not available below 16,500 ft, therefore the forcing factor is assumed constant between ground level and at altitude of 16,500 ft. For contrails, Equation 4.8 is similarly applied, however by expressing the RF per unit distance flown ($\mathrm{RF}_{\mathrm{AIC}}/\mathrm{L}_{\mathrm{ref}}(h)$), instead of emissions. This is expressed in Equation 4.9. RF per distance flown as function of altitude, $\mathrm{RF}_{\mathrm{AIC}}/\mathrm{L}_{\mathrm{ref}}(h)$, is estimated by data from Radel and Shine (2008) [56].

$$s_{AIC}(h) = \frac{\frac{\mathrm{RF}_{\mathrm{AIC}}}{\mathrm{L}_{\mathrm{ref}}}(h)}{\int_0^\infty \frac{\mathrm{RF}_{\mathrm{AIC}}}{\mathrm{L}_{ref}}(h) l(h) dh} \tag{4.9}$$

The forcing factor as function of altitude is plotted in Figure 4.1, using the data from the studies by Radel and Shine (2008), and Kohler et al. (2008) [33, 56].

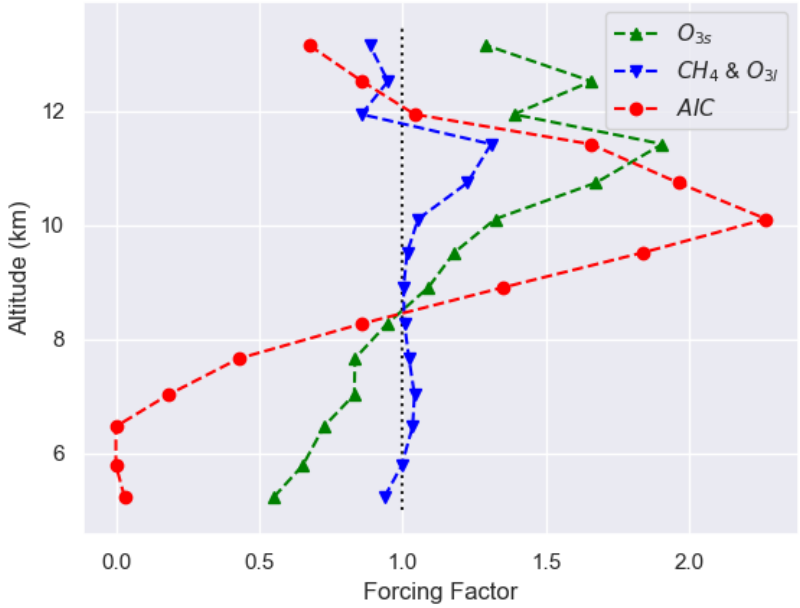

Figure 4.1: Forcing factor for NO_x and contrails based on data from Radel and Shine (2008), and Kohler et al. (2008) [33, 56]

4.1.3. Temperature Response Computation

The temperature change is the final step considered in the causal sequence from emission to impacts. The ATR metric is computed using Equation 2.1, as the time integral of the surface temperature change, ΔT_s, divided by the time horizon. The computation of $\Delta T_S(t)$ for each year is performed using Equation 4.10.

$$\Delta T_S(t) = \int_{t_0}^{t} G_T(t - t')\mathrm{RF}^*(t')dt', \text{ where } G_T(t) = \frac{2.246}{36.8} e^{-t/36.8} \tag{4.10}$$

The normalized RF, RF^*, is equal to 1 if the carbon dioxide change is equal to a doubling compared to pre-industrial times [52]. The total RF^* is the sum of the RF^* of each individual species, $\mathrm{RF}*_i$, which

in turn is a function of the RF, the species efficacy, f_i, and the actual RF concentration equal to doubling of CO_2 concentration, $RF_{2\times CO_2}$:

$$RF^*(t)_i = f_i \cdot \frac{RF_i(t)}{RF_{2\times CO_2}} \tag{4.11}$$

The species efficacy is equal to the ratio between climate sensitivity parameter of the species and that of CO_2.

4.2. Uncertainty Characterisation

The first step in the general workflow of investigation of uncertainties as presented in Chapter 3, is the uncertainty characterisation. Key sources of uncertainties in the forward looking assessment of emission impact on the Average Temperature Response (ATR), are identified and assigned a quantitative description. The first type uncertainty that this study will focus on is scientific uncertainty, which deals with the lack of scientific knowledge and inexact modelling of climate impacts. This type of uncertainty is characterised using a probabilistic framework. This is done by obtaining a description of the probability distribution and best estimate value of the uncertain parameter from scientific literature. Moments of the particular probability distribution are thereafter derived. A summary of the quantitative uncertainty estimates provided by various scientific literature is provided in Table A. The sources that best reflect present day level of scientific understanding are selected and used to perform the uncertainty characterisation in this section. The second type of uncertainty treated in this study is scenario uncertainty, related to the sensitivity to assumptions about future-related parameters used in climate model. Uncertainty in design variable values within the multidisciplinary modelling system are not taken into consideration and hence are not characterised. Hence, this study will solely focus on uncertainties in the climate impact model.

For scientific uncertainty, the first uncertain input parameter group are the uncertainty in direct emissions, identified in the emission index parameters, EI. An overview of these uncertainties is provided in Section 4.2.1. The second parameter group is the CO_2 impulse response function parameters. Namely, the coefficients and time scales $(\alpha_{CO_2}, \tau_{CO_2})$, discussed in Section 4.2.2. Next are the parameters related to the radiative forcing response, namely the radiative efficiencies A_i, forcing factors s_i, and methane lifetime τ_n. These uncertainties are discussed in Section 4.2.3, Section 4.2.4, and Section 4.2.5 respectively. Lastly are the uncertainties in temperature response modelling, identified in the species efficacies f_i of all emission species, and the 'RF due to doubling of CO_2 concentrations since pre-industrial times' parameter, RF_{2xCO_2}. Scenario uncertainty, on the other hand, is identified in the uncertainty around projected global background atmospheric CO_2 concentration. These are discussed in Section 4.1.3. This is further elaborated in Section 4.2.7.

4.2.1. Direct Emission Uncertainty

The direct emissions are computed as function of the emission index (EI), as described in Section 4.1.1. Table 4.1 summarizes the best estimates and respective uncertainty based on present day level of scientific understanding. The uncertainty in the direct emission ofCO_2, NO_x, H_2O, SO_4 and CO are quantified here. For uncertainty around persistent contrail formation, the uncertainty in the three criteria used determine the probability of persistent contrail formation, described in Section 2.2, would be required. This is however deemed outside the scope of this research, and hence is not quantified in this section.

Table 4.1: Emission Index Uncertain Parameter Values and Distributions

Emission Index (Section 4.2.1)	Parameter Description	Best Estimate	Probability Representation
EI_{CO_2}	Carbon dioxide emission index	3.16 [37]	Uniform Distribution: U$(0.99\mu, 1.01\mu)$ [37]
EI_{NO_x}	Nitrogren oxides emission index	Semi-emipirical analytical expression (NASA ECCP program) for the GE90-85B engine [41]	Normal Distribution: N$(\mu, 0.091\mu)$ [37]
EI_{H_2O}	Water vapour emission index	1.23 [4]	Uniform Distribution: U$(0.98\mu, 1.02\mu)$ [4]
EI_{SO_4}	Sulphate emission index	1.20 [37]	Uniform Distribution: U$(0.33\mu, 2.33\mu)$ [4]
EI_{CO}	Soot emission index	0.030 [37]	Uniform Distribution: U$(0.92\mu, 1.25\mu)$ [4]

CO_2 Emission Index The emission index for CO_2 as reported by Lee et al. (2021) [37], gives the value found from the AERO2K emission inventories. The associated uncertainty is additionally very small. According to expert judgement in the most recent study by Lee et al. (2021), the uncertainty is stated to be within 1 % [37]. The basis for this uncertainty is the variability in C:H mass ratio found in jet fuel [4].

Nitrogen Oxides Emission Index As explained in Section 4.1.1, the emission index for NO_x is estimated using the semi-empirical analytical expression developed by NASA's Experimental Clean Combustor Program (ECCP) for the GE90-85B engine [65]. It is used to predict the EI for the GE90 engine family, representative of modern high bypass ratio, high overall pressure ratio turbofan [65]. The EI is correlated with power setting by measurement of emission of NO_x emission at various throttle settings, thereby varying the total pressure and temperature ahead of the engine. The specific humidity factor, H_0, varies with altitude and hence serves as an altitude correction factor, allowing the expression to be used at every point in the mission profile. One source of uncertainty is that the expression refers to conditions ahead of the combustor, and hence does not account for changes in and downstream of the combustor. There is however little change in emission levels due to kinetics occurring downstream of the combustor, hence is is not significantly expected to vary results [41]. As the expression is derived from direct correlation of emission performance at ground level, variability in predictions occurs for the engine at altitude. Study by Schumann et al. (1997) [63] estimates this variability to be ± 18% on average when such semi-empirical expression are used. Correlations specifically formulated for a particular engine, as is the case for the ECCP expression for GE-90 engine family, are however more accurate [41]. As further uncertainty must be still be accounted for due to the variability of the engine performance within the GE90 engine family, it is reasonable to assume an uncertainty range of 15%. The value of EI is treated as being normally distributed around the value obtained using the deterministic semi-empirical analytical expression.

Water, Soot and Suphate Emission Indices Values for EI_{H_2O} is SAGE emission inventory by Kim et al. (2007) [32]. The with uncertainty range being within 2 %. Similarly to the case with carbon dioxide, the main source of uncertainty lies in variation in fuel composition values. The best estimates for CO EI provided by Lee et al. (2021) [37] makes reference to values provided AEDT emission inventories respectively. The EI of soot is evaluated using a constant value, although it is known that it does not solely depend on fuel composition but also on the way the combustion is controlled. Hence, altitude dependency and effect of engine operating conditions are ignored, incurring the larger uncertainties. Eyers et al. (2004) [14] analyses the errors that arise in the estimation of soot production (in estimation used in the AEO2K inventory), referring to its complexity and limited available scientific knowledge. Specific areas of uncertainty are the non-homogenous flow and temperature field in combustion chamber, the variation in influences of different injection systems and combustor technologies, and the influence of type of fuel [14]. Similar to the case with carbon dioxide and water, the EI for sulphate aerosol is solely dependant on the fuel composition. The EI for emission is derived from the fuel sulfur content (FSC), and considering a molar ratio of 2:1 in the conversion of sulfur (S) to sulphate ($SO2$). A conversion

efficiency, close to 100%, additionally defines the percentage of FSC converted to sulphate. The most recent best estimate used in the report by Lee et al. (2021) uses an FSC of 600 ppm used in the AEDT emission inventory and assumes a 100% conversion to sulphate [38]. Uncertainties in the emission indices are considerably large. Sources of uncertainty identified by Lee et al. (2010) are the lower cut-off size of the particle counters, the plume age, the variation in FSC, the conversion efficiency and the number of chemi-ions (CIs) available from the engine. Barrett et al. (2010) [4] quantifies the uncertainty by setting the interval of [400,800] about the best estimate of 600 ppm for the FSC and of [0.5,6] about the best estimate of 2 % mole conversion ratio of sulfur as S^{VI}. Hence applying uncertainty propagation rules, this allows for setting the uncertainty intervals on the best estimates from Lee et al. (2021) [37].

4.2.2. Carbon Dioxide Impulse Response Function

The Simple Climate Model (SCM) by Sausen-Schumann (2000) [62], expressed in Equation 4.3, is utilized to compute the CO_2 concentration response due to CO_2 emission. This model does not employ a single radiative efficiency or perturbation time parameter, instead it models the response as a linear superposition of various response modes with differing perturbation lifetimes. To quantify the uncertainty of the system, the variability in response between different SCM is used. As the SCM are designed to approximate the results from fully comprehensive comprehensive global carbon cycle models, the variation in response between different SCM highlights the variability in those global carbon cycle models. This in turn give an quantification of the level of uncertainty due to lack of scientific knowledge and inexact modelling.

Lee et al. (2021) compares the response of the currently used SCM model with results from two other SCM; the CICERO-2 SCM proposed by Fuglestvedt and Berntsen (1999) and the FaIR SCM by Skeie et al. (2017). The variability in CO_2 concentration responses vary by less than 15 %. Hence, each coefficient α_i and τ_i in Equation 4.3 is described as a normally distributed random variable with a 90 % likelihood of being within 15% of its nominal value. A main area of scientific uncertainty in the global carbon cycle models is the magnitude of ocean and land carbon uptake, especially for land [70]. Based on these estimates, the probabilistic representation for the α_i and τ_i parameters is given in Table 4.2.

Further source of uncertainty in the use of SCMs for the CO_2 response modeling is that linearized models are applicable only for certain ranges of concentrations and emission scenarios [62]. The physics in the carbon cycle model is non-linear, and the effect of the non-linearities begins to take more significant effect after 50-60 years. After this time horizon, CO_2 concentration start to affect the ground and ocean re-uptake and hence the use of the SCMs becomes less applicable, as shown in the comparison with more sophisticated carbon-cycle model, MAGICC 6.0 in the study by Lee et al. (2021) [37]. The impact on the uncertainty is however not quantified in the current study.

Table 4.2: CO_2 Impulse Response Function Uncertain Parameter Values and Distributions

Carbon Impulse Response Function Parameters (Section 4.2.2)	Parameter Description	Best Estimate	Probability Representation
α_i	Coefficients of CO_2 concentration change impulse response function	Table I in Sausen and Schumann (2000) [62]	Normal Distribution: N($\mu, 0.061\mu$) [37]
τ_i	Perturbation lifetime of response modes of CO_2 concentration change impulse response function	Table I in Sausen and Schumann (2000) [62]	Normal Distribution: N($\mu, 0.061\mu$) [37]

4.2.3. Radiative Efficiency

The RF is correlated with the emissions using the radiative efficiency parameter. The literature source providing best estimate and uncertainty ranges of the radiative efficiency based on present day level of scientific understanding is the report by Lee et. al.([37, 38]). The study quantifies the total RF due to commercial aviation in the year 2018, by assimilating estimates from various different studies which employ different comprehensive GCMs. The cumulative emissions of global aviation between the years 1940 and 2018 are taken into account. The provided uncertainty ranges and probability distributions are based on variability in the quantified RF estimates, and observed spread thereof. The uncertainty

estimates hence incorporate the inter-model variability of GCMs, as well as uncertainty in emission inventories used to evaluate the emissions from the recorded air traffic data. The radiative efficiency uncertainty for different emission species are all assumed independent, except for the uncertainty between short-lived NO_x effects, namely short-term ozone, and long-lived NO_x effects, i.e. long term O_3, CH_4, and SWV. The radiative efficiencies of short- and long- term NO_x effects are hence modelled according to bivariate distribution, for which the probability distribution is written out in terms of correlation factor, ρ. The best estimate and probabilistic representation of radiative efficiencies are summarised in Table 4.3.

Table 4.3: Radiative Efficiency Uncertain Parameter Values and Distributions

Species Radiative Efficiencies (Section 4.2.3)	Parameter Description	Best Estimate	Probability Representation
$A_{O_{3S}}$	Radiative efficiency of O_{3S} (Wm^{-2}/Tg)	7.64 [37]	Lognormal Distribution: LN($-0.43\mu, 0.29\mu$) [37]
$A_{O_{3L}}$	Radiative efficiency of O_{3L} (Wm^{-2}/Tg)	-0.200 [37]	Lognormal Distribution: LN($-0.09\mu, 0.44\mu$) [37]
A_{CH_4}	Radiative efficiency of CH_4 (Wm^{-2}/Tg)	-0.401[37]	Lognormal Distribution: LN($-0.09\mu, 0.44\mu$) [37]
A_{SWV}	Radiative efficiency of SWV (Wm^{-2}/Tg)	-0.0710 [37]	Lognormal Distribution: LN($-0.09\mu, 0.44\mu$) [37]
A_{H_2O}	Radiative efficiency of H_2O (Wm^{-2}/Tg)	0.00520 [37]	Normal Distribution: N($\mu, 0.44\mu$) [37]
A_{SO_4}	Radiative efficiency of SO_4 (Wm^{-2}/Tg)	-19.9 [37]	Lognormal Distribution: LN($-0.56\mu, 1.54\mu$) [37]
A_{CO}	Radiative efficiency of CO (Wm^{-2}/Tg)	101 [37]	Lognormal Distribution: LN($-0.27\mu, 0.74\mu$) [37]
A_{AIC}	Radiative efficiency of AIC (Wm^{-2}/km)	1.82 $\cdot 10^{-12}$ [37]	Normal Distribution: N($-0.43\mu, 0.43\mu$) [37]

NO_x Radiative Efficiencies Best estimate and uncertainty is based on the reported values by Lee et al. (2021) [37], which estimates the RF due to NO_x-induced O_{3S}, O_{3L}, CH_4 and SWV using results from 20 studies as assessed based on 18 different global atmospheric chemistry/climate models (GCMs). A wide range of present-day aviation emission inventories are additionally utilized [37]. The variation in results is indicative of the differences in the available GCMs/CCMs, and is therefore a measure of the present modelling uncertainty. The spread of global RF from the array of different studies is utilized to formulate the likelihood ranges for the radiative efficiencies. The correlation between the observed short- and long- lived RF amongst the 20 studies is additionally used to estimate the correlation factor ρ of 0.7.

Long-lived NO_x Effects The radiative forcing for long-lived NO_x species is modelled according to an exponential decay function, as expressed in Equation 4.5. The radiative efficiency parameter hence represents the radiative forcing per unit NO_x emission at t_0, being the first year emission. The radiative efficiency values provided by Lee et al. (2021) [37] are in terms of $mWm^{-2}(Tg(N)yr^{-1})^{-1}$. The provided values hence represent the time-integrated radiative forcing divided by the cumulative NO_x emission. The radiative efficiency parameter, to be expressed in terms of $mWm^{-2}(Tg(NOx))^{-1}$, hence requires the time-integrated quantity provided by Lee et al. (2021) to be divided by the methane perturbation lifetime, τ_{CH_4}, according to the relation given in Equation 4.12. τ_{CH_4} is assumed to be equal to 12 years. Additionally, numbers presented by Lee et al. (2021) are normalized to Tg(N) rather than 1 Tg(NO_x). Assuming composition mainly of NO_2, the reported values are reduced by a factor of

(46/14), being the molar ratio of NO_2 to that of N. An important scientific understanding change giving smaller likelihood range estimates for the radiative efficiency of long-lived O_3 compared to previous studies is the ability of present-day GCMs to directly model the long-term ozone depletion [37]. Another important scientific understanding change is of the climate impact of stratospheric water vapour (SWV). Namely, its depletion resulting from NO_x induced reduction in methane abundance results in a cooling effect. Estimates of RF of SWV were not provided in the previous report by Lee et al. in 2009 [36].

$$\int_0^T RF_i^{ref}(t_0)e^{-\frac{t}{\tau_i}}dt \approx RF_i^{ref}(t_0)\cdot\tau_i \tag{4.12}$$

Water, Soot, Sulphate Radiative Efficiency The study by Lee et al. (2021) uses wide variety of GCMs to obtain the RF best estimates; 10 estimates across 8 models were used to evaluate soot and sulfate aerosol normalized RFs, while water vapor effects are assessed using results from nine studies. The radiative efficiency is expressed in terms of integrated radiative forcing over the perturbation lifetime ($RF\cdot yrs$). This is assumed equal to the radiative efficiency as it is assumed that effects are only present during the year of emission. The uncertainty is quantified from the variability in RF estimates from range of studies. This degree of uncertainty is smaller compared to the previous estimates by IPCC (1999) [53], due to the larger number of available studies and more detailed physics used in the GCMs [37]. Overall, the LOSU remains low due to limited amount of studies and large uncertainty in the emission inventories accounted for in the uncertainty in RF response.

Contrail Radiative Efficiency Lee et al. (2021)[37] provides best estimates of contrail radiative efficiency, with the use of process-based simulation models. Due to the small number of independent estimates of contrail RF, the uncertainty is estimated from the sensitivities of the underlying processes, parameters and fields. The uncertainties associated with the processes were fitted to a single uncertainty range using a Monte Carlo analysis with a normal distribution. The processes fall into two groups; those connected with the upper tropospheric water budget and the contrail cirrus scheme (including uncertainty in number of soot particles emitted, uncertainty in upper tropospheric ice-supersaturation frequencies, ice nucleation within the plume) and those connected with the change in radiative transfer due to the formation of contrail cirrus [37].

4.2.4. Forcing Factor

The forcing factor term, s_i, of NO_x-induced short- and long-lived O_3 and CH_4 is derived from the estimates of RF per unit emission as function of altitude, ($\frac{RF_{CH_4}}{E_{NO_x}}(h)$), from the study by Kohler et al. (2008) [33]. The same study quantifies the uncertainty of $\frac{RF_{CH_4}}{E_{NO_x}}(h)$ to be normally distributed with a 66% likelihood of being within 15 % of the published values [33]. As as the CH_4, O_{3S} and O_{3L} radiative forcing estimates are not available at altitudes below 16,500 ft, $\frac{RF_{CH_4}}{E_{NO_x}}(h)$ is assumed constant between ground level and at altitude of 16,500 ft.

For contrails, the forcing factor is derived from the estimates of RF per distance flown as function of altitude, ($\frac{RF_{AIC}}{L_{(ref)}}(h)$), from the study by Radel & Shine (2008) [56]. Radel & Shine estimate the uncertainty in these estimates to be normally distributed with a 90% likelihood that the value is within 70% of the reported values. The source of uncertainty highlighted by Radel includes the annual variability of upper tropospheric humidity, assumed ice crystal radiative parameters and the neglect of three-dimensional radiative transfer in used GCMs. These uncertainties are also included in the RF efficiency uncertainty quantification, covered in Section 4.2.3. Further sources of uncertainty include the neglect of the impact of variation in engine parameters, and the empirical choice of the relative humidity threshold at which persistent contrails form. The RF per distance flown estimates are uncertain with a 90% likelihood that the value is within 70% of published values, according to Radel and Shine (2008) [56].

Value of forcing factor at a given altitude is likely to be correlated with that at nearby altitudes. To account for this correlation, the approach used in study by Schwarz & Dallara (2011) [65] is utilized. Uncertainties in RF per emission (or per distance flown in the case of contrails) are assumed independent at 2.5 km intervals in altitude. Specifically, uncertainties are independent at 17,500ft, 25,500ft, 33,500ft, and 41,500ft, and a linear variation between the altitudes is assumed for the uncertainty between these levels. Table 4.4 summarises the defined uncertain parameters and their probability descriptions.

Table 4.4: Radiative Efficiency Uncertain Parameter Values and Distributions

Forcing Factors (Section 4.2.4)	Parameter Description	Best Estimate	Probability Representation
CH_4 altitude forcing 1	CH_4 radiative efficiency at h=17500 ft ($mW/m^2/Tg(N)/a$)	Table 1 in Kohler et al. (2008) [33]	Normal Distribution: N($\mu, 0.16\mu$) [33]
CH_4 altitude forcing 2	CH_4 radiative efficiency at h=25500 ft ($mW/m^2/Tg(N)/a$)	Table 1 in Kohler et al. (2008) [33]	Normal Distribution: N($\mu, 0.16\mu$) [33]
CH_4 altitude forcing 3	CH_4 radiative efficiency at h=33500 ft ($mW/m^2/Tg(N)/a$)	Table 1 in Kohler et al. (2008) [33]	Normal Distribution: N($\mu, 0.16\mu$) [33]
CH_4 altitude forcing 4	CH_4 radiative efficiency at h=41500 ft ($mW/m^2/Tg(N)/a$)	Table 1 in Kohler et al. (2008) [33]	Normal Distribution: N($\mu, 0.16\mu$) [33]
O_{3S} altitude forcing 1	O_{3S} radiative efficiency at h=17500 ft ($mW/m^2/Tg(N)/a$)	Table 1 in Kohler et al. (2008) [33]	Normal Distribution: N($\mu, 0.16\mu$) [33]
O_{3S} altitude forcing 2	O_{3S} radiative efficiency at h=25500 ft ($mW/m^2/Tg(N)/a$)	Table 1 in Kohler et al. (2008) [33]	Normal Distribution: N($\mu, 0.16\mu$) [33]
O_{3S} altitude forcing 3	O_{3S} radiative efficiency at h=33500 ft ($mW/m^2/Tg(N)/a$)	Table 1 in Kohler et al. (2008) [33]	Normal Distribution: N($\mu, 0.16\mu$) [33]
O_{3S} altitude forcing 4	O_{3S} radiative efficiency at h=41500 ft ($mW/m^2/Tg(N)/a$)	Table 1 in Kohler et al. (2008) [33]	Normal Distribution: N($\mu, 0.16\mu$) [33]
AIC altitude forcing 1	AIC radiative efficiency at h=17500 ft ($mW/m^2/Tg(N)/a$)	Table 1 in Radel & Shine (2008) [56]	Normal Distribution: N($\mu, 0.43\mu$) [56]
AIC altitude forcing 2	AIC radiative efficiency at h=25500 ft ($mW/m^2/Tg(N)/a$)	Table 1 in Radel & Shine (2008) [56]	Normal Distribution: N($\mu, 0.43\mu$) [56]
AIC altitude forcing 3	AIC radiative efficiency at h=33500 ft ($mW/m^2/Tg(N)/a$)	Table 1 in Radel & Shine (2008) [56]	Normal Distribution: N($\mu, 0.43\mu$) [56]
AIC altitude forcing 4	AICe radiative efficiency at h=41500 ft ($mW/m^2/Tg(N)/a$)	Table 1 in Radel & Shine (2008) [56]	Normal Distribution: N($\mu, 0.43\mu$) [56]

4.2.5. Species Lifetime

The long-lived non-CO_2 emission species relevant to the analysis of climate impact of aviation are the long-lived NO_x effects. The atmospheric concentration decay is modelled according to an exponential function parameterized using an e-folding time. This parameter is characterised as the methane perturbation lifetime, for which the 2007 IPCC report gives an uncertainty estimate of 90% likelihood of being within 15 % of the reported best estimate of 12 years [68]. The probability distribution is assumed normal.

Table 4.5: Species Lifetime Uncertain Parameter Values and Distributions

Species Lifetimes (Section 4.2.5)	Parameter Description	Best Estimate	Probability Representation
τ_{CH_4}	Methane perturbation lifetime (yrs)	12 [68]	Normal Distribution: N($\mu, 0.09\mu$) [68]

4.2.6. Temperature Response Model Parameters

The relation between the radiative forcing and temperature response is modelled using the species efficacy parameter, f_i, being the ratio of climate sensitivity of the species to that of carbon dioxide. The climate sensitivity is uncertain and its estimates differ considerably among different atmospheric models [43]. This introduces uncertainty into the species efficacy parameter. Uncertainties are represented as normal distributions, except for f_{soot}, which is represented using a log-normal distribution. The second identified uncertain parameter in the temperature change response model is the RF due doubling of CO_2 atmospheric concentration since pre-industrial times (year 1750), RF_{2xCO_2}. The 2007 IPCC report

gives an uncertainty estimate of 90% likelihood of being within 10 % of the reported best estimate [68]. Again, the distribution is assumed normal. Table 4.6 gives an overview of the temperature response model parameters and uncertainty ranges provided by literature.

Table 4.6: Temperature Response Uncertain Parameter Values and Distributions

Temperature Change Model (Section 4.2.6)	Parameter Description	Best Estimate	Probability Representation
$f_{O_{3S}}$	Short lived ozone species efficacy	1.37 [55]	Normal Distribution: N($\mu, 0.32\mu$) [18]
$textf_{O_{3L}}$	Long lived ozone species efficacy	1.18 [37]	Normal Distribution: N($\mu, 0.32\mu$) [18]
$textf_{CH_4}$	Methane species efficacy	1.18 [55]	Normal Distribution: N($\mu, 0.10\mu$) [18]'
$textf_{SWV}$	Stratospheric water vapour species efficacy	1.18 [37]	Normal Distribution: N($\mu, 0.32\mu$) [18]
$textf_{H_2O}$	Water vapour species efficacy	1.14 [55]	Normal Distribution: N($\mu, 0.32\mu$) [18]
$textf_{SO_4}$	Sulphate aerosol species efficacy	0.9 [68]	Normal Distribution: N($\mu, 0.33\mu$) [68]
$textf_{CO}$	Soot aerosol species efficacy	0.7 [68]	Lognormal Distribution: N($-0.43\mu, 0.93\mu$) [68]
$textf_{AIC}$	Aicraft-induced cloudiness species efficacy	0.59 [37]	Normal Distribution: N($\mu, 0.10\mu$) [18]
RF_{2xCO_2}	Radiative forcing due to doubling of atmospheric CO_2 concentration compared to pre-industrial times (W/m^2)	3.7 [68]	Normal Distribution: N($\mu, 0.06\mu$) [68]

4.2.7. Scenario Uncertainty

Scenario uncertainty is characterised in the form of sensitivity to assumptions about future-related parameters used in the climate model. The identified source of scenario uncertainty is the global background CO_2 concentration $\chi CO_2, 0$, which accompanies the forward looking CO_2 RF response modelling. As is shown in Equation 4.4, the RF response for CO_2 is dependant on the background CO_2 levels, in ppm. In the study by Proesmans & Vos (2021), this value is set equal to 380ppm [52] and assumed constant. However according to different anthropogenic emission forecasts, this background CO_2 value between the year 2030 and 2100 is predicted with high confidence to increase [48]. This affects the CO_2 RF response as a larger background concentration would imply a smaller fractional increase in CO_2 due to a given emission perturbation. Fuglestvedt et al. (2003) [17] quantifies this effect: for a CO_2 concentration increase of 1ppb at 365 ppm background concentration, the forcing is 0.015 Wm^{-2}/ppm, while for a background concentration of 450 ppmv this is reduced to 0.013 Wm^{-2}/ppm.

This scenario uncertainty is investigated by implementing different realistic future global anthropogenic CO_2 emission scenarios, and quantifying the sensitivity to the variation in resultant ATR. The four CO_2 emission projections for the 21st century, i.e. Representative Concentration Pathways (RCPs), outlined by Meinhausen et al. (2011) [48], are used as representations of realistic future scenarios. These represent the emission projections by four different Integrated Assessment Models (IAMs) for 2005–2100. The projections include the 'RCP2.6' [74], the 'RCP4.5' [9], the 'RCP6.0' [45], and lastly the 'RCP8.5', also known as the 'business-as-usual' scenario [57]. Each RCP is detailed below:

- **RCP2.6** Assessment by Van Vuuren et al. (2011) [74] explores the 'low end' global emission scenario, exploring the possibility to keep global mean temperature increase below 2 degrees relative to pre-industrial times. Deemed to be technically feasible assuming participation of all countries, and requires the cumulative emissions of greenhouse gases from 2010 to 2100 to be reduced by 70% compared to a baseline scenario that assumes current historical trends to continue throughout the 21st century. It assumes a concentration of 450ppm in the year 2050, and a decline to 405ppm by the year 2100.

- **RCP4.5** Assessment by Thompson et al. (2011) [9] explores the scenario that the global RF stabilizes at 4.5 W/m^{-2} in the year 2100. This scenario would demand significant changes in the energy system, such as switch to electricity greener emissions energy technologies and the deployment of carbon capture and geologic storage technology. The harmonized RCP4.5 CO_2 concentration in 2100 is 526 ppm. The stabilisation of CO_2 concentration is assumed to be reached in the year 2080.
- **RCP6** Assessment by Masui et al. (2011) [45], explores the scenario that global RF reaches 6 W/m^{-2} in the year 2100. The greenhouse gas emission mitigation measures are less rigorous compared to the RCP2.6 and RCP4.5 scenarios. A stabilisation in RF and CO_2 concentration is assumed by the year 2100 to be at 660 ppm.
- **RCP8.5** Assessment by Riahi et al. (2011) [57] surveys the 'high emission scenario', where the RF reaches 8.5 W/m^{-2} by the year 2100. This model draws assumptions about large population growth and slow income growth, together with modest rate of technological advancement. An exponential growth in CO_2 concentrations sees a level of 560ppm in the year 250 and 950ppm in the year 2100.

The CO_2 global atmospheric concentration change projected by different RCPs are plotted in Figure 4.2. As the time window of interest for this study is between the year 2020 and 2120, trends are further linearly extrapolated between the year 2100 and 2120.

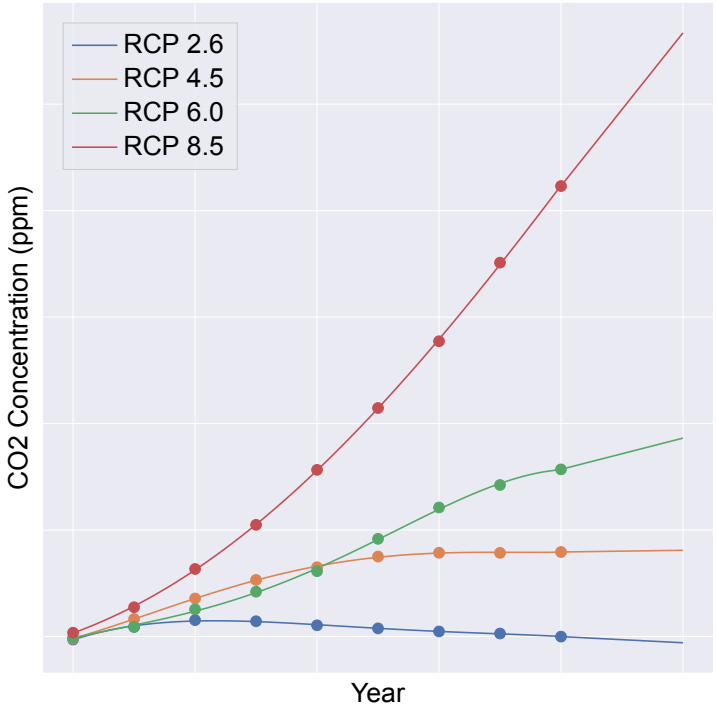

Figure 4.2: Atmospheric CO_2 Representative Concentration Pathways (RCPs) 2.6, 4.6, 6 & 8

5

Methodology for Uncertainty Investigation

The uncertainty investigation comprises of the uncertainty analysis (UA), the robustness-based design optimization (RBDO), and the sensitivity analysis (SA). This corresponds to the steps C to E in the general workflow for uncertainty investigation given in Chapter 3. In the UA, the statistics about the output ATR reduction potential (ATRRP) are inferred for the climate optimized aircraft design. In the RBDO, a robust solution is aimed form, having both minimal ATR and minimal variability in the ATRRP. Finally, the sensitivity analysis is to be performed on both the climate-optimized and the robust design solutions, to quantify the contribution of the individual sources of uncertainty towards the variability in climate impact reduction potential. This chapter serves to provide a detailed overview of the methods used within the each step of the outlined uncertainty investigation.

5.1. Uncertainty Analysis

In the uncertainty analysis, it is aimed to quantify the uncertainty in the ATRRP of the ATR-optimized aircraft design with respect to the minimal DOC-optimized aircraft design. A set of requirements are to be met in order to conduct the UA. Firstly, converged ATR-optimized and cost-optimized aircraft designs are necessary. This is obtained by conducting the single-objective optimization for minimal ATR- and DOC- using the updated set of climate impact model parameter best estimate values outlined in Section 4.2. The multidisciplinary optimization framework used in the study by Proesmans & Vos (2021) [52], as explained in Section 3.2, is directly applied for this task. The design vector of the ATR- and DOC- optimized aircrafts are given in Section 7.2. Furthermore, an uncertainty propagation method is required. The Monte Carlo Simulation (MCS) method is chosen, which further explained in Section 5.1.1. The implementation of the MCS is the further elaborated on in Section 5.1.2.

5.1.1. MCS Methodology Overview

Standard MC relies on random sampling according to the probability distributions of the random variable. This process requires sufficient information about the probability distribution of of the inputs to be known. The uncertainty characterisation of the climate impact model in Section 4.2 shows the necessary information is indeed available. Random samples are 'independent', meaning the generation of a sample is not correlated with the generation of any of the other samples [23]. Each set of random input samples independently and randomly generates an output through running the deterministic computational model. After repeating the process multiple times, the output data is combined to estimate the variability of the stochastic system outputs. After generating n number of output samples, the expected value of the output, $s = \mathbb{E}[\mathcal{Y}]$, is estimated by taking the average of output values:

$$\hat{s_n} = \frac{1}{n} \sum_{i=1}^{n} y_i \tag{5.1}$$

The MC estimator is considered an *unbiased estimator* as according to the strong law of large

numbers, the average converges almost certainly to the true expected value s. The variance of the MC estimator of $\hat{s_n}$ is expressed as:

$$\mathbb{V}[\hat{s_n}] = \mathbb{E}[(s - \hat{s_n})^2] = \frac{\sigma^2}{n} \tag{5.2}$$

Hence, the Root Mean Squared Error (RMSE) for $\hat{s_n}$ is σ/n^2. The convergence rate of the estimator is in the order of $n^{-\frac{1}{2}}$. The variance of the output, defined as $\mathbb{V}[Y] = \sigma^2$ can be estimated directly from the sample values, y_i, as follows:

$$\zeta^2 = \frac{1}{n-1}\sum_{i=1}^{n}(y_i - \hat{s_n})^2 \tag{5.3}$$

The estimator given above is unbiased as $\mathbb{E}[\zeta^2] = \sigma^2$ for $n > 2$ [82].

The described methodology for standard MC shows its effectiveness and accuracy in evaluating statistical moments of the output, and is very easy to implement. The most important advantage of standard MC is that the convergence rate is not dependant on the dimensionality of the problem. When a non-intrusive approach to MCS is used, only evaluations of the original deterministic model are performed, allowing the simulation model to be treated as a black box. This is advantageous, for one must not modify the original model, and hence is more straightforwards and easy to implement. A disadvantage of MCS, in particular for non-intrusive approaches, is the large computational effort due to the required large number of samples for convergence of the error. This can make standard MC infeasible for high-fidelity simulations [82]. However, the linear climate model used in this study employs linearised relations between input and output space and does not have significant computational cost. Therefore the large computational effort is not a limiting factor. Alternatively, intrusive MCS approaches can be utilized, which typically rely on the usage of surrogate models. Surrogate models reduce computation burden of having to repeatedly evaluate the deterministic model. Surrogate model prediction with high-dimensional input space however is prone to accumulation of modelling prediction error [25]. In addition this would eliminate the advantage of ease of implementation of non-intrusive MCS.

Quasi Monte Carlo Quasi-random Monte Carlo (QMC) offers a sampling methodology for the MCS to overcome the limitation of slow convergence rate of the standard MC approach. Quasi-random sampling is performed using quasi-random sequences, which aim to uniformly cover the unit interval, $[0, 1]$. The sequences are designed to sample each region of the sample space with the same likelihood [23]. The 'discrepancy' of the sequence is a measure of the deviation from this uniformity. The usage of quasi-random sequences implies that unlike random samples, quasi-random samples are not independent from each other. The MC estimator, $\hat{s_n}$, is computed in the same manner as in a standard MCS, as expressed in Equation 5.1. For QMC however, the RMSE of the estimator, $\hat{s_n}$, is now in the order of $log(n)^d/n$, with d being the size of the input sample space [50]. For small dimensionality of the problem, this is more favorable than standard MC. Therefore the low discrepancy of quasi-random sequence can potentially improve the convergence speed of the propagated output uncertainty.

5.1.2. Monte Carlo Simulation Implementation

The uncertain parameters included in the UA are the CO_2 impulse response function coefficients and time scales $(\alpha_{CO_2}, \tau_{CO_2})$, the radiative efficiencies A_i of all species, the forcing factors s_i for short- and long- lived NO_x effects, the CH_4 lifetime, τ_{CH_4}, the efficacy parameter for all species, f_i, and the 'RF due to doubling of CO_2 concentrations since pre-industrial times' parameter, RF_{2xCO_2}. The emission indices are not treated as uncertain parameters/variables as the uncertainty in radiative efficiency already incorporates uncertainty in the quantification of emissions. The uncertain input parameters are treated as quasi-random variables according to the assigned probability distribution as described in Section 4.2, using the Sobol sequence. Quasi-random variables have the property of not being statistically independent, the way random variable are. Each region of the input sample space has the same likelihood of being sampled, thereby favoring convergence of the MCS [23]. This is further verified in Section 6.1. The Sobol sequence is chosen over other quasi-random sequences as it produces least error and is most stable for high-dimensional problems [50]. This applies to this case study as a total of 32 uncertain parameters are identified.

A sample matrix is generated by sampling from the Sobol sequence for each of uncertain parameter. Sobol sequences are sequences in base 2, hence a sample size of base 2 is required to maintain accuracy [51]. A sample size of 2^{14} (=16384) was used for the uncertainty analysis. The Sobol sequence generates uniformly distributed points on the unit hyper cube, $[0,1]^k$. The first point of the sequence is always at the point $(0,0)$. Transformation to Gaussian distribution makes the point infinite, which leads to large error. Although a common option is to skip this point, the applied method is to *scramble* the points and maintain the full set. *Scrambling* randomly distributes the Sobol sequence on the unit hyper cube, while still maintaining the space-filling property, and hence accuracy, of the original sequence. This circumvents the drawback of inferior rate of convergence brought about when transforming to Gaussian distribution [51]. The uniformly distributed samples are transformed to the uncertain parameter's distribution using the inverse cumulative density function (CDF). This applies to all parameters, except when the distribution is bivariate, which is the case for the short- and long- term radiative efficiencies of NO_x. The Sobol sequence is not able to account for correlated uncertainties, hence the parameters are separately sampled using standard random sampling. For n number of samples of the k uncertain parameters, the sample matrix is generated as follows:

$$\mathbf{X} = \begin{bmatrix} x_{1,1} & x_{2,1} & \cdots & x_{k,1} \\ x_{1,2} & x_{2,2} & \cdots & x_{k,2} \\ \vdots & \vdots & \ddots & \vdots \\ x_{1,n} & x_{2,n} & \cdots & x_{k,n} \end{bmatrix} \tag{5.4}$$

After the samples are generated, n MC evaluations are performed. Each row of the sample matrix is inputted into the function evaluating the ATRRP, referred to as $f(x)$. This function computes the ATR of the climate-optimized aircraft, ATR_{ATR}, and cost optimized aircraft, ATR_{DOC}, by executing the climate impact model on the design vector of each aircraft design respectively. ATRRP is then equal to $ATR_{DOC} - ATR_{ATR}$. The same set of input parameter samples is used for evaluating ATR of both optimized aircrafts, hence uncertainties are not double counted. n output ATRRP samples are obtained, from which variability and statistical moments are computed:

$$\begin{bmatrix} ATRRP_1 \\ ATRRP_2 \\ \vdots \\ ATRRP_n \end{bmatrix} = \begin{bmatrix} f(x_{1,1}, x_{2,1}, \cdots, x_{k,1}) \\ f(x_{1,2}, x_{2,2}, \cdots, x_{k,2}) \\ \vdots \\ f(x_{1,n}, x_{2,n}, \cdots, x_{k,n}) \end{bmatrix} \tag{5.5}$$

5.2. Robustness-Based Optimization

A robust design solution is one whose performance has minimal variability about the mean due to the uncertainties in the climate impact modelling system. The main elements of RBDO as identified by Zaman et al. (2011) are as follows [81]:

1. **Objective Robustness**: Relates to maintaining robustness in the objective function.
2. **Estimating variance of the objective function:** This relates to the estimation of uncertainty, via uncertainty propagation methods.
3. **Multi-objective Optimization:** Robustness-based optimization considers two objectives: optimizing the mean of the objective function and minimizing its variability.

The first element, objective robustness, requires a metric for quantifying the robustness in objective function. The standard deviation σ of the ATRRP is utilized. Directly related to the first element, is the estimation of variance of the objective function. Hence, at every design point evaluated by the optimizer, uncertainty propagation needs to be performed to quantify the $ATRRP\sigma$. This is carried out utilizing the methodology employed in the UA (outlined in Section 5.1. A MCS using Sobol quasi-random sampling of all uncertain input parameters as summarized in Section 4.2 is performed. The MC sample size is set at 2048. Verification of convergence of the ATRRP σ estimate was carried out in Section 6.4, to ensure the MC sample size is sufficient to ensure MCS estimation error is below 0.5%. To avoid the burdensome computational cost associated with quantifying uncertainty at various iterations of the optimizer, numerous existing RBDO studies implement surrogate model instead of the full deterministic model, to propagate uncertainty [24, 26, 31, 66]. Again however, the climate model

employed in this study makes use of first order approximation of more comprehensive models global climate models, and has limited computational cost. Therefore, usage of surrogate modelling for the RBDO is not implemented.

The third element of RBDO is multi-objective optimization. This applies given both minimal ATR, the deterministic objective, and minimal ATRRP σ, the robustness objective, is searched. The two objectives are conflicting, signifying that no optimal solution has absolute superiority over the other [34]. This requires the employment of Pareto optimization methods. Two types of Pareto Optimization methods exist. The first are classical methods, that convert the problem to a series of single-optimization problems by operating on one candidate solution at a time. The second are population-based methods, which operate on a set of candidate solutions at the same time [34]. Population-based methods are particularly advantageous when seeking for a dense set of solutions, in order to give designers a full picture of the trade-off.

Genetic algorithms (GA) are heuristic methods, which operate on a set of candidate solutions simultaneously (population-based method). These exhibit significant advantage over classical methods which operate on a single solution at a time, as they concurrently search different regions of the design space. Obtaining a large and diverse set of optimal solutions therefore becomes more computationally efficient. Secondly, their applicability extends also to non-convex or discontinuous solution spaces, for which classical methods do not always promise convergence [2]. Thirdly, being a heuristic method, GAs do not require the computation of gradient of objective function or constraints the way gradient-based optimization methods would. This is troublesome for the robustness objective, as σ is estimated using a MCS, and thereby is itself a random variable with a degree of variability. To ensure convergence of a gradient-based algorithm would hence require a very large MCS sample size requirement, making the cost prohibitive if a large set of solutions is desired. The use of GAs is therefore the most widespread method to robustness-based Pareto optimization problems, especially in the field of uncertainty-based design optimization. This is verified through the literature covering Pareto optimization in the field of UMDO [28, 30, 31, 66]. The literature additionally verifies in specific the extensive applicability of the NSGA-II algorithm, which is designed for high efficiency and a well distributed set of solutions, in particular for low-dimensional optimisation problems [80].

Section 5.2.1 serves to further explain the workings of genetic algorithms and in specific for the Non-Dominated Sorting Genetic Algorithm II (NSGA-II), whilst Section 5.2.2 elaborates more on the implementation of the NSGA-II for the current study.

5.2.1. Genetic Algorithm Methodology

GA apply the mechanisms that evolutionist theory uses to explain the emergence of species. Weak, 'unfit' species go extinct, whilst strong, 'fit' species are most likely to reproduce and pass their genes to the next generation. Random changes can occur, which are preserved in case the change gives additional fitness to the population [34]. In terminology used within GAs, a solution vector is referred to as a *population* and each solution is an *individual* or *chromosome*. Each individual is composed of *genes*, which determine features of the individual. The operators used to generate a new population are crossover and mutation. In crossover, two parent chromosomes are selected to have their genes combined to generate new offspring chromosomes. Parent chromosomes are chosen with proclivity towards fitness. Mutation on the other hand puts forth random variations to the chromosomes. Mutation operator introduces diversity into the population and allows for unexplored regions of the design space to be evaluated. This avoids having the algorithm being stuck in local optima [34].

The Figure 5.1 from the depicts the three main steps taken, from left to right, within the inner loop of the NSGA-II algorithm. The creating of offspring using the crossover and mutation operators is the first step. In the second step, each individual of the combined offspring and parent populations is ranked using a non-dominated sorting approach. This involves identifying the first front as the individuals not dominated by any other individuals. The second front is then identified by repeating the process after subtracting individuals from first front. As there will be a situation where a front needs to be split because not all individuals are allowed to survive, the crowding distance sorting is used. Hence the last front is split according to the crowding distance of the points, being a measure of how close each point is to other individuals in the objective function space. Individuals with larger crowding distance are selected for the next generation. This ensures that the points are uniformly distributed and diverse [76].

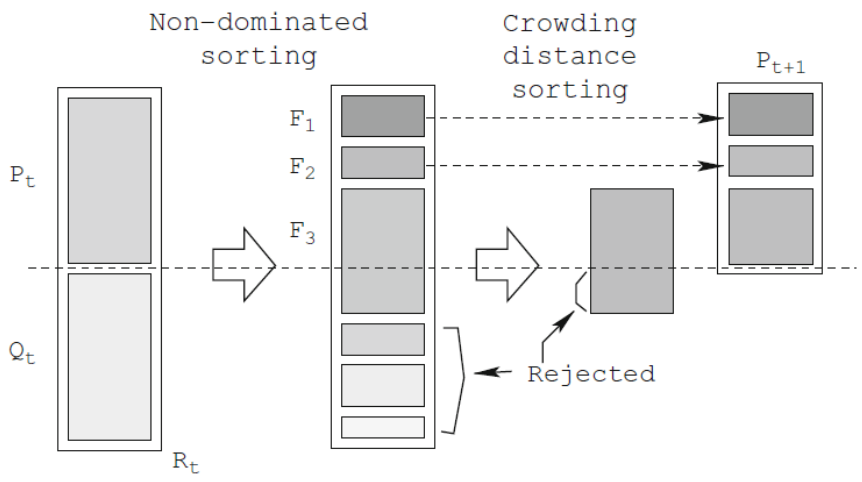

Figure 5.1: The procedure of non-dominated sorting algorithm (NSGA-II). Source [12]

The parameters of NSGA-II are described in Table 5.1:

Table 5.1: Main parameters of NSGA-II algorithm and respective descriptions

Parameter	Description
Population Size	Size of population.
Number of generations	Number of generations over which NSGA2 will evolve. Larger number ensures better convergence. Convergence rate declines significantly with increasing generation number [75]
Crossover probability	Controls the chance of each chromosome undergoing crossover process [75]
Mutation probability	Controls the chance of each chromosome undergoing mutation process. Contributed to prevent population being trapped in local optima [75]
Crossover Distribution index (DI_c)	Determines probability distribution of the value of genes of offspring around their parents' during crossover operation. Large value of DI_c keeps offspring similar to parents [22]
Mutation Distribution index (DI_m)	Determines probability distribution of the value of genes of offspring around their parents' during mutation operation Large value of DI_m keeps children similar to the parents [22]

5.2.2. NSGA-II Implementation

Table 5.2 presents the specifications of the implemented NSGA-II. As population size is the most important parameter in the hierarchy of impacts imposed by GA parameters, special attention was made in order ensure that it is large enough to capture a sufficiently diverse set of genes at the start of the optimization, and such that the density of solutions of the Pareto front is sufficient to obtain convergence. The generation size was likewise calibrated in order to allow for sufficient iterations of the algorithm to be carried out for the computed Pareto optimal set of solutions to converge to the actual Pareto front. This is further verified in Section 6.5. The *pymoo* multi-objective optimization library is utilized for the Python implementation of the NSGA-II.

Table 5.2: Specification of NSGA-II

Population Size:	No. of Generations:	Crossover Probability:	Mutation Probability:	Crossover DI:	Mutation DI:
50	15	0.9	0.1	15	20

5.2.3. Optimal Solution Selection

Methods for selection of optimal solution from the array of Pareto optimal solutions are reviewed by Wang et al. (2017) [77]. Considering the method's number of required user inputs, simplicity of method and applicability, *TOPSIS* and *GRA* are found most suitable. *TOPSIS* looks at identifying the solution with smallest Euclidean distance from the ideal solution and largest Euclidean distance from the negative-ideal solution. The 'ideal solution' is defined as the combination of the best value of each objective in the set of Pareto solutions. Instead, the 'negative-ideal' is defined as the combination of the worst value of each objective. Weighting parameters are included, representing the relative importance of each objective function in the selection of the optimal solution. The *GRA* method, on the other hand, computes the optimal solution with use of the Gray Relational Coefficient (GRC), being a measure of the similarity between the objective values and the ideal solution. Being free from decision maker inputs, this method has very straight forward implementation and hence is additionally utilized [77].

5.3. Sensitivity Analysis

The sensitivity analysis is carried out in two distinct steps. Firstly, the global sensitivity analysis (GSA), and secondly, the local sensitivity analysis (LSA). The GSA measures the contribution of uncertain climate model parameters to the output variance. This includes the full range of uncertain input parameters as implemented in the UA (described in Section 5.1.2). The LSA is conducted in order to quantify the sensitivity in ATRRP of the climate-optimized aircraft designs around the assumed projections of future anthropocentric growth scenarios. Specifically, the sensitivity with respect to the global background atmospheric CO_2 concentration, $\chi_{CO_2,0}$, around the currently assumed constant background concentration scenario is investigated. The GSA and LSA in combination allow the identification of most influential inputs on the uncertainty of the ATRRP for the climate-optimized aircraft designs.

For the GSA, a two-step approach is implemented. Firstly, a Morris analysis is conducted, where parameters are varied one-at-a-time. This allows to qualitatively rank the parameters according their influence towards output variability, at a low computational cost. For a selection of most influential parameters identified from the Morris analysis, a Sobol sensitivity analysis is carried out. This gives a quantitative measure of the importance of parameters, which includes parameter interaction effects [83]. A brief overview of both Morris and Sobol methods are given in Section 5.3.1 and Section 5.3.2 respectively, after which the overall implementation of the SA methods is described in Section 5.3.3.

5.3.1. Morris Method

The Morris method is a qualitative analysis which has its advantage over the quantitative counterpart due to its lower required number of model evaluations. Qualitative methods are based on the discretization of input space to identify which input parameters have largest impact on the output variability [8]. Each uncertain input parameter effect on output is defined as either negligible, linear and additive, or nonlinear. It is an efficient and simple method for SA for interval analysis [58].

Morris method varies one parameter at a time while keeping the rest at a baseline value. Considering the best estimate values of the input uncertain parameters, x_j as a baseline for the model $f(\cdot)$, Morris method is performed by varying one of the inputs within the defined uncertainty interval while the other input parameters are frozen. The k number of intervals are first split into p levels, giving p discrete values within each interval and a grid of pk points. An r number of repetitions are measured for each variable, with r requiring to be at least equal to p. Influence of variation in input on the output is called the elementary effect, $\mu_j^*(i)$ and is computed for the j^{th} input variable for the i^{th} repetition as follows:

$$e_{j(i)} = \frac{f(x_j(i) + \delta_j) - f(x_j(i))}{\delta_j} \tag{5.6}$$

, with δ_j being a step variation in the input variable. In the end, the standard deviation, σ_j and mean μ_j^* is computed of the elementary effects of each variable. Large value of mean shows an important influence on output, and a large standard deviation shows a large nonlinear effect and interaction with other elements [72].

Ranking according to the elementary effect allows for most influential parameters to be identified. This ranking shall only be regarded qualitatively, as it does not provide quantitative information of how

much more one parameter is influential over another [47]. The Morris method does not accurately quantify the total sensitivity when various distribution types of inputs are considered. Also, interactions between inputs are not captured by the elementary effects [40]. $r(k+1)$ MCS evaluations, with r being the number of repetitions, are required. r is required to be at least as large as the number of levels, p, in which the uncertainty interval is split into [8].

5.3.2. Sobol Method

Sensitivity analysis using Sobol Indices is a 'variance-based technique', a quantitative approach opposed to the previously discussed Morris method. Variance based methods aim to understand how the output variance is attributed to individual input variables and the interaction between them. First order effect of a given input parameter X on output Y is formulated as follows:

$$\frac{Var_X[E(Y \mid X)]}{Var(Y)} \tag{5.7}$$

, where $Var_X[E(Y \mid X)]$ denotes the variance of Y due to fixed value of X, and $Var(Y)$ denotes the total output variance. The Sobol method looks to quantify the sensitivities via the Sobol Indices. $S_{T,i}$ is a measure of the output variance in case all parameters except for x_i are kept constant. $S_{1,i}$ instead is the expected reduction in output variance in case x_i is kept constant [47]. For example if there are three input parameters (A, B, C), the *total effect* of parameter A is:

$$S_T(\mathrm{A}) = S_1(\mathrm{A}) + S_2(\mathrm{AB}) + S_2(\mathrm{ABC}) \tag{5.8}$$

, where $S_T(\mathrm{A})$ denotes the total sensitivity index for parameter A, $S_1(\mathrm{A})$ denotes the *first order* sensitivity index for parameter A, and $S_2(\mathrm{AB})$ denotes the second order sensitivity index for parameters A and B, and so on. The second order indices would provide an indication of the level of interactions between the two parameters. If no higher order interactions take place, the difference between S_T and S_1 would be zero. The method requires to repeatedly carry out MCS. For first and total order sensitivity index computation, the computational cost is $n(k+2)$, with n being the MCS sample size, and k being the number of input parameters.

Steps for Implementation of Sobol Method: The procedure of computing the Sobol indices as implemented by Bilal (2014) [7] is provided here. The model output function, $y = f(x)$, and an input factor space Ω^k is considered.

1. Select the total number of simulations to run.
2. Select the input parameters for the sensitivity analysis and assume a range for the input variables
3. Select a probability distribution for the parameters.
4. Run the Monte Carlo Simulation and calculate the mean, f_0 and variance, D of the parameters according to :

$$f_0 = \int f(x)dx \approx \frac{1}{N}\sum_{k=1}^{N} f(x_k)$$

$$D \approx \frac{1}{N}\sum_{k=1}^{N} f^2(x_k) - f_0^2$$

   , where N is the sample size of the MC simulation.
5. Compute the partial variance or first order effects for each parameter by fixing the values of that parameter i and varying the rest of the parameters:

$$D_i \approx D - \frac{1}{2N}\sum_{k=1}^{N}[f(x_k) - f(x_{ik} - x'_{-ik})]^2 \tag{5.9}$$

   , where $x_{-i} = (x_1, ..., x_{i-1}, x_{i+1}, ..., x_m)$ is the combination complementary to x_i.

6. The total sensitivity effect for each parameter is finally found:

$$D_{tot} \approx \frac{1}{2N} \sum_{k=1}^{N} [f(x_k) - f(x_{ik}^{'}, x_{-ik}^{'})]^2 \tag{5.10}$$

7. Sort the parameters according to their sensitivities.

5.3.3. SA Implementation

For the GSA, the two-step approach is implemented. The Morris analysis is conducted for the full set of uncertain input parameters ($k = 32$). An r number of repetitions are measured for each parameter [8]. Influence of variation of input on the output is quantified using the elementary effect, μ^*. With p (number of levels in which the uncertainty interval is split into) being set at 64, and r (number of repetitions are measured for each parameter) being set at 100, a total of 3300 ($r(k+1)$) evaluations of the climate impact model are required. In the second step of the GSA, the top 10 identified parameters identified from the Morris analysis are used to run a Sobol sensitivity analysis. The two quantities of interest estimated for each parameter are the total sensitivity index, $S_{T,i}$, and the first order sensitivity index, $S_{1,i}$. Higher order interactions are not investigated in this study, due to the observed small relative difference between the first and total order indices. The size of n is set at 2^{10} (=1024), allowing for sufficient convergence of the sensitivity indices, as verified in Section 6.3. The *SALib* sensitivity analysis library is utilized for the Python implementation of the GSA methods. For the LSA, variability in output ATRRP is measured by implementing the different RCPs, as outlined in Section 4.2.7, one-at-a-time.

6

Verification

6.1. Random Sample Generation

The choice of random sampling method was made between standard random sampling and quasi-random sampling. Due to the large dimensionality of the UQ problem given the total of 32 inputs, the advantage of using the quasi-random sampling requires verification. This is because the upper bound of the Monte Carlo (MC) error is expected to increase in proportion with the dimension [67]. Verification is performed by comparing the convergence of the MC error when using standard- and Sobol quasi-random sampling with increasing sample size. The MC error is expressed as the absolute difference between the MC estimate of the $ATRRP$, $\hat{\mu}_n$ and the expected $ATRRP$, μ, as given in Equation 6.1. The expected value is computed using the deterministic climate impact model (i.e. without considering uncertain input parameters as random variables). Both values are computed for the climate-optimized aircraft design.

$$\epsilon = \mid \hat{\mu}_n - \mu \mid \tag{6.1}$$

The convergence of the two methods is compared by plotting the MC error against sample size. For Sobol quasi-random sampling, the samples must be generated for a sample size of base 2, 2^m. Hence, the MC estimate is computed using discrete sets of input samples generated with increasing m. For random sampling, the sample size may have any size. Hence, the MC estimate is computed on the continuously increasing set of input samples. The comparison of convergence is shown in the log-log plot Figure 6.1:

The slope of the best fit line in the log-log plot of sample size against MC error indicates the convergence rate, p, being the order at which the MC error, approaches zero with increasing sample size. When using random sampling, p is shown to be -0.59, while for quasi-random sampling, p is -0.95. This numerical experiment firstly verifies that the constructed MCS UQ framework correctly and accurately propagates the uncertainties. Secondly, it is verified that the Sobol quasi-random sampling method allows for improved convergence of the MCS, and hence should be used for the UA, as well as in the RBDO and when carrying out the variance-based GSA.

6.2. Input Parameter Distribution Choice

For the characterisation of scientific uncertainty, input parameters for the climate impact model are identified as being uncertain. These parameters are represented using a probabilistic framework and are assigned a probability distribution according to uncertainty characterisation in literature. The lack of scientific knowledge implies that there is additional uncertainty introduced due to assumption about uncertainty distribution itself. Therefore the sensitivity of climate impact model output with respect assigned input uncertainty distribution is investigated.

The output statistics of the $ATRRP$ of the climate optimized aircraf obtained for varying input distribution choices are given in Table 6.1. After evaluating the set of input parameter distributions of the current uncertainty characterisation (as summarised in Section 4.2), a set of input parameters where all distributions are triangular, and a set where all distributions are uniform is evaluated. For triangular

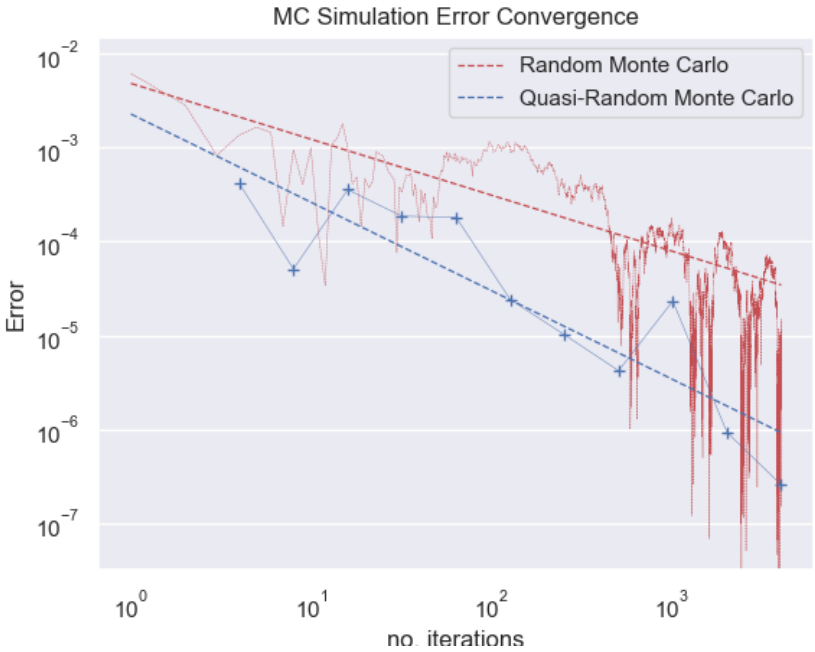

Figure 6.1: Convergence of MC estimate of the climate-optimized aircraft design ATRRP μ using random and Sobol quasi-random sampling

distribution, the upper and lower maximum values are set as the 5 and 95 percentile of the normal or log-normal distributions. This is similarly done when setting the input distribution as uniform.

Table 6.1: Sensitivity of Statistics of ATRRP of climate optimized aircraft design with respect to input parameter distribution choice

Statistic	Baseline Distribution	Triangular Distribution	Uniform Distribution
Mean, μ [%]	56.9	56.5	56.9
Median [%]	54.2	55.9	63.0
Skeweness, $\tilde{\mu}$	0.341	0.259	1.49
St. dev, σ [%]	26.9	16.7	52.9
90 % likelihood range [%]	[17.3, 98.9]	[30.0, 85.3]	[17.2, 185]

The output variability is most sensitive to the choice in input distribution when uniform distributions are implemented, given by the doubling of the standard deviation with respect to the baseline case. Usage of a triangular distribution significantly reduces the standard deviation by 35 %. This is expected, as the tail end of the distribution is cut off. Similar reduction is observed in the 90 % likelihood range, for which the change occurs for the greater part due to an increase in the lower bound.

6.3. GSA Two-Step Approach

As explained in Section 5.3, the *two-step* approach is implemented in order to reduce the total required computational effort when running the Sobol GSA. In order to verify whether screening parameters causes a reduction in the variance of the $ATRRP$, the cumulative density function (CDF) obtained from the MCS using the full parameter set and the top 10 most influential parameters according to the Morris method is compared. The CDF of the $ATRRP$ of the climate optimized aircraft design obtained from a MCS using an n of 2^{12}, sampled using Sobol quasi-random sequence is shown in Figure 6.2. It is observed that the CDFs match nearly identically, hence the substantial part of the uncertainty is accounted for by the set of screen parameters using the Morris method.

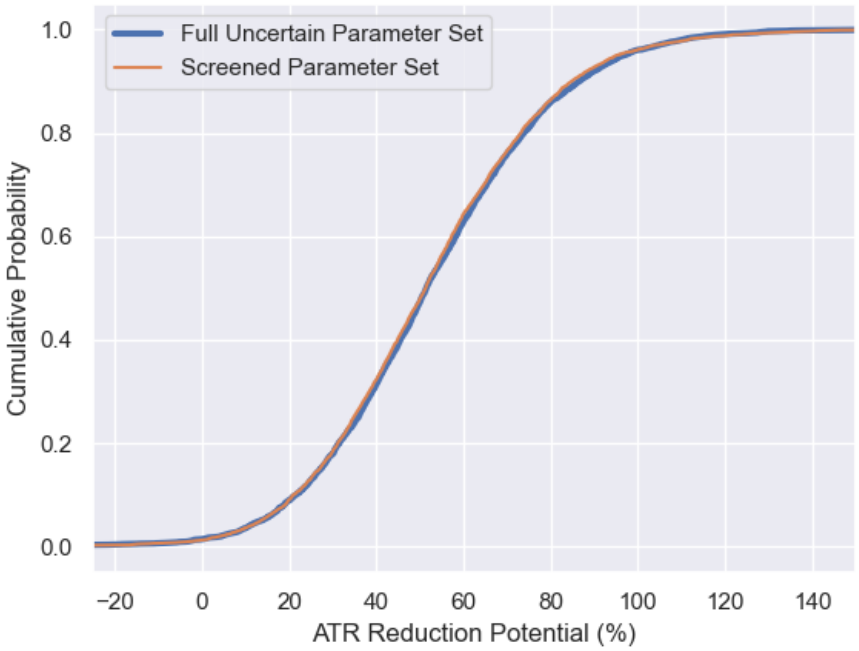

Figure 6.2: Comparison of Cumulative Density Function of ATR Reduction Potential of Climate Optimized Aircraft Design using Full and Screened Parameters Sets

The number of MC evaluations required when using the Morris method is controlled with the number of repetitions, r, which is set at 100. The greater this parameter, the higher the degree of convergence of the elementary effects, μ^*. The degree of convergence of the sensitivity indices, $S1$ and ST using the Sobol method is similarly dependent on the defined MCS sample size, n, which is set at 4096. In order to verify whether the size of r and n provide sufficient convergence for the Morris and Sobol analysis respectively, the 90 % confidence interval of the outputs provided by the SA software, *SALib*, are analyzed. It is verified that confidence intervals for μ^* and ST are all within 10 % of the estimated value. This level of convergence is deemed sufficient in order to confidently draw conclusions from GSA results.

6.4. RBDO Sample Size Determination

For every solution evaluated by the GA, the robustness objective is evaluated, namely the ATRRP σ. This requires a MCS, for which Sobol quasi-random samples are used to render improved convergence. In order to not cause prohibitive computational cost, the sample size is adjusted such that the ATRRP σ is estimated to a sufficient degree of accuracy. The convergence of the standard deviation estimate of the MC simulation using Sobol quasi-random sampling for increasing sample size is plotted in Figure 6.3, showing that the deviation of the σ estimate falls below 0.5 % of the final value at a sample size of 2^{12}. This is deemed a sufficient level of accuracy, and hence is used for the MC uncertainty quantification within the GA.

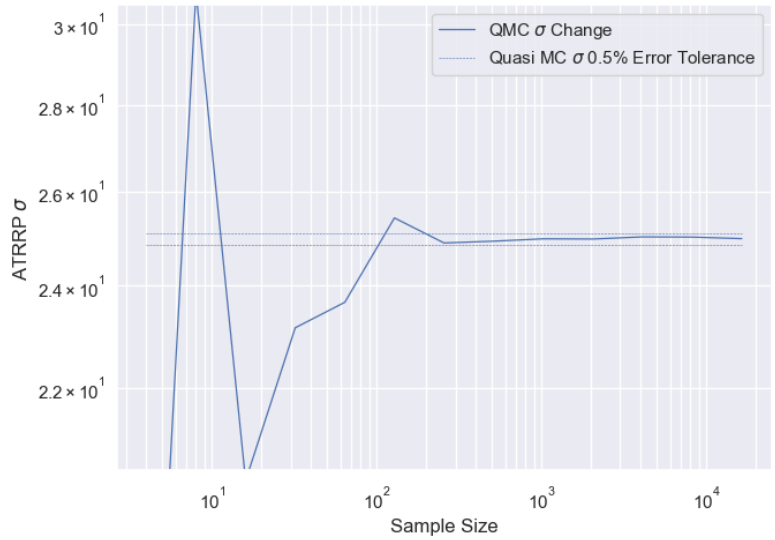

Figure 6.3: Convergence of Monte Carlo Standard Deviation Estimate of TR Reduction Potential of Climate Optimized Aircraft Design

6.5. NSGA-II Convergence

The hyper-volume metric is a measure of the area of the objective space dominated by the approximation Pareto set of solutions with respect to a reference point [85]. The reference point is defined as the set of worst objectives value possible of both ATR and ATRRP σ, corresponding to the ATR of the DOC-optimized aircraft and the ATRRP σ of the ATR-optimized aircraft. Figure 6.4 gives the plot of the hyper-volume for increasing function evaluations. It is observed that by the final function evaluation, corresponding to the generation size of 15, the hyper-volume has reached an asymptotic value. The change in hypervolume is below 5e-4 over the last 7 generations. This verifies that a satisfactory degree of convergence is attained, indicating that further iterations of the GA will not lead to significant improvement in the approximated Pareto set.

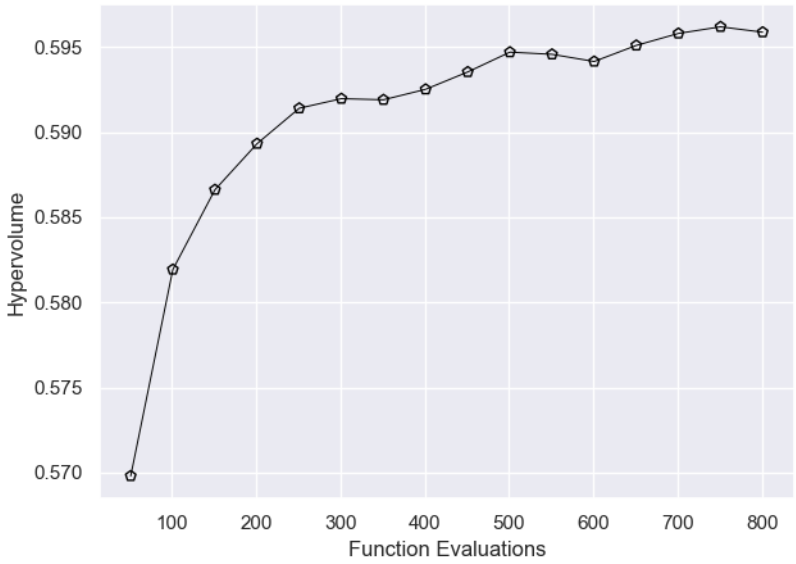

Figure 6.4: Hypervolume Convergence of Robustness-Based Climate Optimization using NSGA-II Algorithm

7

Results

This chapter presents the results of the investigation of uncertainties. Firstly the deterministic optimisation results of the climate-optimised and cost-optimised aircrafts are introduced in Section 7.1. In Section 7.2, the quantification of impact of climate model uncertainties on the average temperature response potential (ATRRP) of the climate-optimised aircraft design is quantified. Subsequently, Section 7.2 presents the robustness-based optimization results, where different robust climate-optimized conceptual aircraft designs are identified. Global and local sensitivity analysis results are thereafter presented in Section 7.4.

7.1. Deterministic Optimisation Results

The optimisation results without the consideration of uncertainties are summarised in this section. The deterministic optimization of the climate-optimized aircraft, as well as the cost-optimised aircraft are presented here. The cost-optimized aircraft is very relevant fore the remained of the uncertainty investigation in this study given it is used as bases of comparison when of the climate impact performance for a given aircraft design.

The top level requirements of the deterministic optimization are defined for the maximum structural payload, the harmonic range, the approach speed and the take-off length, as specified in Table 7.1. The values utilized in the climate optimization study by Proesmans & Vos [52] are adapted. These requirement values are similar to existing single-aisle, medium range aircraft such as Boeing 737 or Airbus A320. The maximal structural payload of 18.2 metric tons is approximated given a 180 passenger high-density cabin configuration in economy seats.

Table 7.1: Top Level Requirement of Deterministic Optimization

Requirement [unit]	Value
Maximum structural payload [kg]	18200
Harmonic range [km]	3200
Approach speed [m/s]	70.0
Take-off length (ISA conditions) [m]	2100

A commencement of fleet operation in the year 2020 is assumed, with a maximal productivity level of 3.95 $\cdot 10^12$ RPK per year reached by 2050. This maximal level of productivity is assumed constant between the year 2050 to 2055. By the year 2085, a termination of fleet operation is assumed. Climate impact due to the operation of the fleet are however further evaluated until the year 2120. The mission profile is characterised having a harmonic range of 3200 km (making it a medium-range aircraft), with an additional 460 km loiter phase and a 35 minute turnaround time.

The deterministic optimisation results and have close resemblance with those obtained in the study by Proesmans & Vos [52]. The same optimisation framework, top level requirements and productivity levels are utilized, hence this is anticipated. To give an overview of the climate impact performance of both aircraft, the contribution to the total ATR according to the different emission species, as well

as the operating cost performance, are shown in Table 7.2. In addition, an overview The DOC- and ATR- optimised aircraft designs resulting from the deterministic optimisation are briefly summarised, via the respective design variable values given in Table 7.3. More comprehensive overview of the climate optimization results can be consulted in the report by Proesmans & Vos [52].

Table 7.2: Components of the total ATR of the climate- and cost- optimized aircraft designs

	ATR [mK]							**DOC**
	Total	CO_2	NO_x	H_2O	SO_4	CO	Contrails	$[USD/pax \cdot nm]$
ATR-optimized	10.9	11.3	-0.398	0.129	-0.0621	0.0490	0.00	0.139
DOC-optimized	25.4	11.1	0.684	0.127	-0.0611	0.0483	13.5	0.126

Table 7.3: Design variable values of the climate- and cost- optimized aircraft designs

	Cruise altitude $[km]$	**Cruise Mach**	**BPR**	**OPR**	**TT4** $[K]$	**WS** $[kN/m^2]$	**AR**	$C_{\mathbf{L,max}}$
ATR-optimised	7.54	0.6	10.7	45.7	1479	6.06	11.6	2.8
DOC-optimised	9.97	0.7	7.00	44.3	1530	5.65	11.2	2.7

The total ATR of the climate-optimized aircraft is reduced by 57% compared to the cost-optimized aircraft. This reduction is primarily achieved via the reduction of the contrail contribution, which reduces from 53 % of the total ATR to zero. The absolute ATRRP of contrails is hence 13.5 mK. NO_x and CO_2 have ATRRP of secondary magnitudes, with NO_x having an absolute ATRRP of 1.08 mK and CO_2 having a reduction potential of 0.2 mK. The impact of H_2O, CO and SO_4 on the ATRRP are shown to be negligible. It is also shown that the total ATR and DOC are conflicting design objectives, with the DOC reducing by 10.3 % for the cost-optimized aircraft. The reduction in total ATR was achieved primarily by operating at decreased cruise Mach and altitude of 0.6 and 7.54 km respectively, and an increased OPR of 45.7. More discussion with regards to design variable change, its impacts on the climate performance and also on the resultant uncertainty in ATRRP is provided in Section 7.2.1.

7.2. Uncertainty Analysis Results

Figure 7.1 shows the distribution of output ATRRP for the climate-optimized aircraft obtained from the MCS using 2^{14} Sobol samples. To normalize the output, the ATRRP is expressed as percentage of the ATR of the DOC-optimized aircraft design. The absolute and normalized output distribution statistics are presented in Table 7.4.

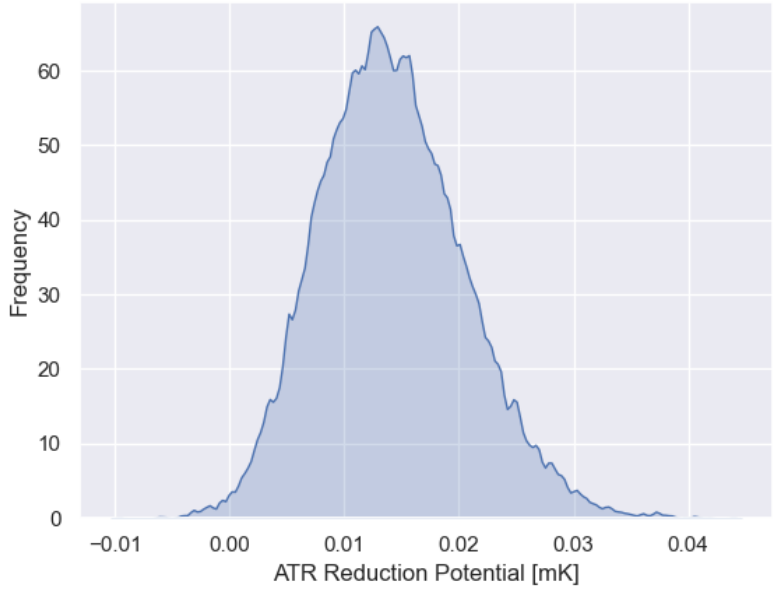

Figure 7.1: Probability Density Plot of ATRRP of climate-optimized Aircraft Design

Table 7.4: Average temperature response reduction potential (ATRRP) mean, median, standard deviation and 90% likelihood range

	Mean, σ	**Median**	**St. dev, σ**	**90 % likelihood range**
Absolute [mK]:	14.2	13.8	6.38	[4.38, 25.2]
Normalized [%]:	55.5	54.2	25.0	[17.3, 98.9]

The individual components of the ATR are divided into the different emission species. The confidence interval of the components of the normalized ATRRP for the climate-optimized aircraft design are given in the violin plot in Table 7.5. The probability distribution of the individual components of the ATRRP are graphically represented in the violin plot in Figure 7.2. The ATRRP shows to have a 90 % confidence interval from 4.48 to 25 mK, corresponding to 17.3 to 98.9 % of the ATR of the cost-optimized aircraft.

Table 7.5: Mean, standard deviation and 90 % likelihood range of the individual components of the ATRRP

	ATRRP Mean, μ [%]	ATRRP St. Dev, σ [%]	ATRRP 90 % Likelihood Range [%]
Total	55.6	25.0	[17.2, 98.9]
CO_2	-1.49	0.109	[-1.67, -1.31]
NO_x	2.90	2.35	[-0.342, 7.13]
H2O	-0.0163	0.00866	[-0.0332, -0.00504]
Soot	-0.00653	0.0111	[-0.0228, -4.74e-4]
SO4	0.00827	0.0200	[2.90e-4, 0.0311]
Contrails	52.0	28.9	[11.9, 95.2]

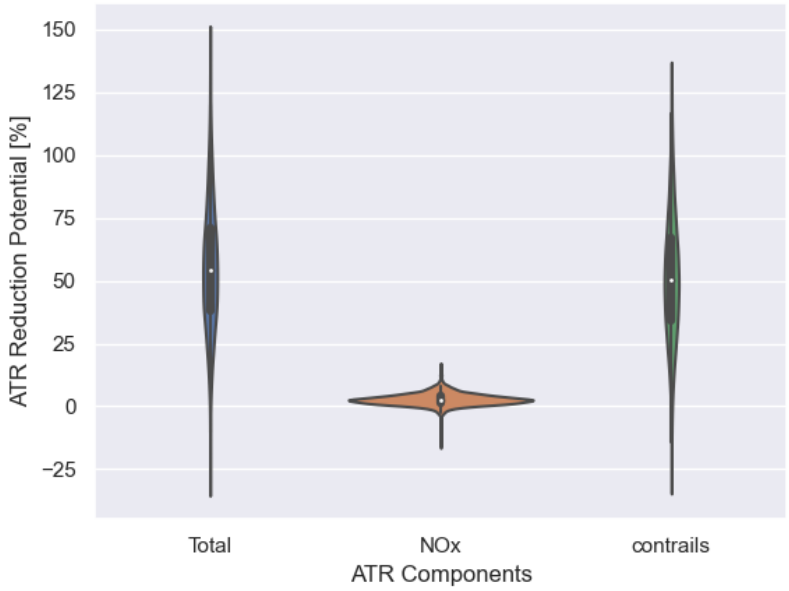

Figure 7.2: Probability distribution of components of the ATRRP of climate-optimized Aircraft Design

The size of the ATTRP uncertainty of contrails are shown to be predominantly larger compared to the rest of the emission species, with a 90% likelihood range spanning from 11.9% to 95 % of cost optimized aircraft ATR as computed in the deterministic case. ATRRP of NO_x and CO_2 additionally have significant uncertainties, although being an order of magnitude smaller than that of contrails. The size of the uncertainty range seems to be mainly be driven by the absolute magnitude of the ATRRP of the species. Contrail thereby has the largest ATRRP σ component.

The size of the ATRRP σ compared to the ATRRP μ is referred to as a coefficient of variation (CV). It can be seen as an indicator of how uncertain the input parameters are for that species. This seems to be a secondary driver to their overall ATRRP uncertainty. For example, although that soot and sulphate have largest CVs of 1.67 and 2.5, their absolute ATRRP σ size is negligible. From the components having significant contribution to ATRRP (namely contrails, NO_x, and CO_2), NO_x appears to have largest CV as its ATTRP σ is close to the value of its ATTRP μ. Contrails also have significant CV (ATTRP σ being 55% of ATTRP μ), while CO_2 has significantly the lowest CV (ATTRP σ 7% of ATTRP μ).

7.2.1. Uncertainty Analysis of ATR-DOC Pareto Front

To understand how to uncertainty in ATRRP varies in the trade-off between climate impact and operating costs, the MCS is performed on the different Pareto optimal aircraft designs. These Pareto optimal solutions are obtained from the multi-objective optimization for minimal ATR and DOC. Figure 7.3 gives the size of the 90 % confidence interval of the ATRRP for the various Pareto-optimal designs.

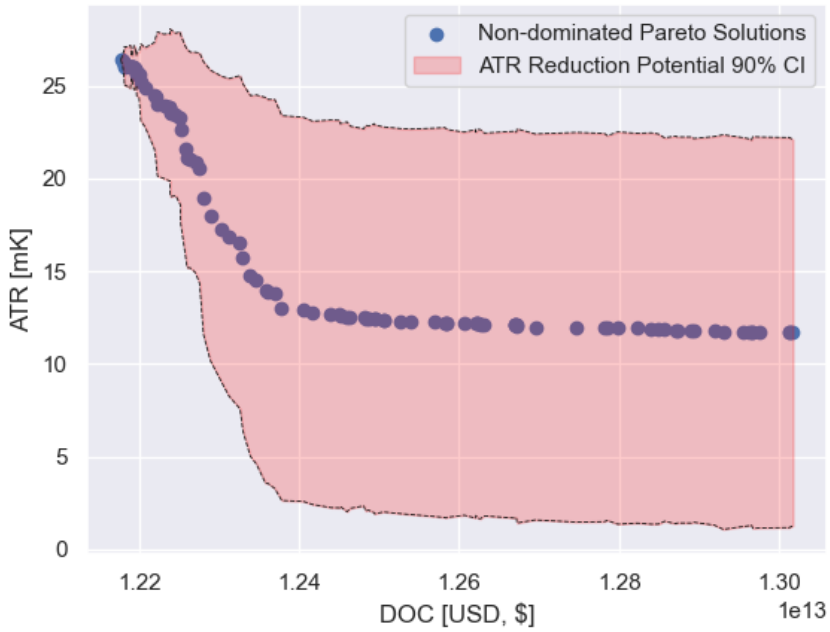

Figure 7.3: Pareto Optimal set of solutions of ATR & DOC multi-objective optimization together with the respective 90 % Likelihood Range of the ATRRP

It can be observed that a near direct correlation is present ATR and variability in ATRRP, given by the size of the likelihood range. This is confirmed by plotting the ATR against the estimated ATRRP σ, as shown in Figure 7.4.

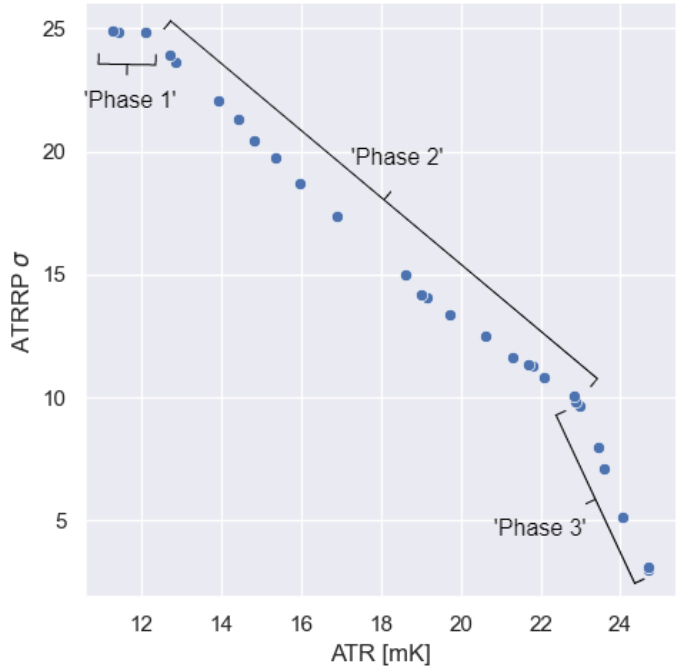

Figure 7.4: Change in ATRRP standard deviation for varying ATR computed for the Pareto-optimal set of designs from the ATR & DOC multi-objective optimization

The different regions of Pareto front presented in Figure 7.4 can be identified from the changes in the slope of the front. Namely, the first phase spans between ATR values of 10.9 and 12.2 mK, and sees negligible improvement in ATRRP σ. The second phase is between ATR of 12.2 and 23.1 mK, where now the ATTRP σ sees a reduction. The third and final phase is identifiable from the steepening of the slope of the of the Pareto front. This phase spans between ATR values of 23.1 and 25.5 mK. To additionally gain insight into the changes that occur throughout the Pareto front, the contribution from different emission species towards the total ATR across the ATR-DOC Pareto front is plotted in Figure 7.5.

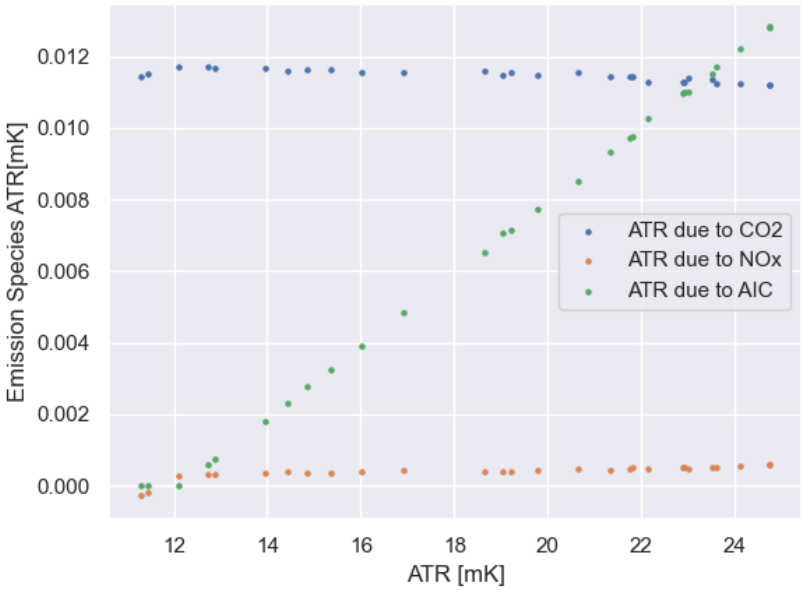

Figure 7.5: Contribution to the total ATR according to the individual emission Species

The aircraft-induced contrail impact goes from having a zero contribution towards the total ATR in the first phase of the Pareto front, between 10.9 mK to 12.2 mK, to having a positive contribution of almost 50% of the total ATR. This increase increase in contrail ATR correlates with the decrease in ATRRP σ. NO_x goes from having a negative ATR of -0.4 mK to a positive ATR of 0.7 mK. This change predominantly takes place in the first phase of the Pareto front, after which it increases at a slower rate. CO_2 contribution also sees an increase in the first phase from 11.4 to 11.7 mK. Throughout the second and third phase it linearly decreases to a value of 11.2 mK.

To better understand what causes the uncertainty to vary, the change in design variable values are plotted, for the ATR- and DOC- Pareto optimal set of solutions. Groups of design variables are subdivided into the operational design variables, engine design variables, and airframe design variables.

Operational Design Variables

In the first phase, between 10.9 mK to 12.2 mK, the cruise height increases from 7.5 to 8.5 km, as shown in Figure 7.7. The first implication is that the SFC of the engine increases, causing an increase in fuel consumption from from 9.7 to 9.96 metric tons, and hence a growth in CO_2 contribution from 11.2 to 11.7 mK. This increases the magnitude of the CO_2 ATRRP, therefore increasing the contribution towards total ATRRP σ. The second implication is that forcing factors of O_{3S} grows from 0.8 to 1.05. This makes the warming term of the NO_x dominate, thereby increasing the NO_x contribution to the total ATR. This reduces the magnitude of the NO_x ATRRP, thereby reducing the contribution to total ATRRP σ. The negligible observed change in ATRRP σ in the first phase shows that the positive CO_2 and negative NO_x contribution to the uncertainty balance each other out.

In the first phase, the ambient temperature below the cruise altitudes of 8.5 km, according to ISA relations, is above 235 Kelvin. According to the contrail formation criteria, this is not sufficiently cold for

persistent contrail formation to occur. This explains the contrail contribution to the ATR remaining zero. Persistent contrail formation to take place as cruise altitude increases above 8.5 km, in the second and third the phases of the Pareto front. As the ambient temperature continues to decrease, the probability of ice supersaturation and hence of persistent contrail formations rises. The cruise altitude increase also increases the contrail radiative forcing factor from 1 to 1.2, driving the growth in contrail ATR from 0 to approximately 60% of the total ATR.

In the third phase of the Pareto front, between ATR values of 23.1 and 25.5 mK, a steepening of the slope of the Pareto front is observed in Figure 7.4. This coincides with the cruise altitude surpassing 9.3 km. Past this altitude, the contrail forcing factor becomes correlated with the forcing factor defined at level 3 (at $h_{cr} = 10.5km$), in addition to that at level 2 (at $h_{cr} = 9.3km$). As the DOC-optimized aircraft has a cruise altitude of $10km$, it is likewise strongly correlated with the forcing factor at level 3. This signifies that past cruise altitude of 9.3 km, ATR uncertainty becomes correlated to a higher degree with that of the DOC-optimized aircraft, and the uncertainty in the ATRRP of the design solution reduces at a faster rate with increasing ATR. A takeaway here is that the shape of the Pareto front is very dependant on the formulation of uncertainties, specifically of that of the forcing factors. This is a limitation of the overall uncertainty characterisation methodology.

The cruise Mach sees a steep increase in the first phase between 10.9 mK and 12.2 mK, from Mach 6.3 to Mach 7.0, as shown in Figure 7.7. The driver behind this change is the increase in flight altitude, which increases the speed at which optimum L/D is achieved. Increasing the cruise Mach number additionally causes increase in SFC due to loss in net thrust, adding to the observed growth in fuel consumption mass and CO_2 contribution. Throughout the rest of the Pareto front, Mach 7.0 remains constant. Another direct consequence of flying faster is the decrease in block time, being the main driver of the DOC. This impact can be read from the steep rise in DOC for ATR below 15 mK from the ATR and DOC Pareto front presented in Figure 7.3.

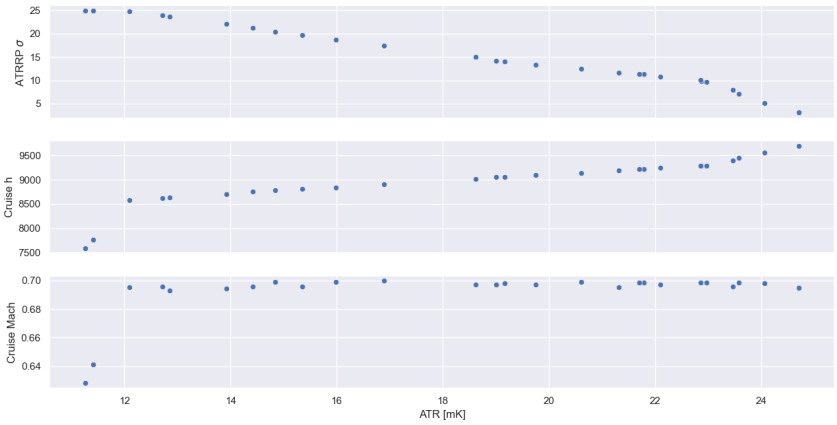

Figure 7.6: Change in operational design variable values for the Pareto-optimal set of designs from the ATR & DOC multi-objective optimization

Engine Design Variables

In the first phase, between 10.9 mK to 12.2 mK, the OPR and turbine inlet temperature TT4 see significant increases, as shown in Figure 7.7. The OPR increases from 37.8 to 44.1, and the TT4 increases from 1450 to 1510 K. As a consequence, the pressure and temperature ahead of the combustor, p_4 and T_4 both increase. This drives the increase in NO_x emission index and contributes to the observed reduction in NO_x ATRRP. Additionally, the increase in OPR serves to increase the thermal and hence total efficiency of the turbofan (from 29.8 to 31.0 %). This compensates for the increase in SFC due to larger cruise Mach and altitudes, and limits both the CO_2 ATR its contribution to the ATRRP σ in this initial phase.

Conversely, a reduction in BPR is observed in the first phase (between 10.9 mK to 12.2 mK), from 9.95 to 7.61, as shown in Figure 7.7. The BPR decrease drives the loss in propulsive efficiency (from 74.5 to 72.1 %), decreasing the slope of the hot exhaust air mixing line, and hence also the probability

of contrail formation. However as the ambient conditions for contrail formation are not met in this phase, hence the change in BPR has no impact on contrail ATR contribution, and hence the ATRRP σ also remains relatively unchanged. In the second and third phase of the ATR- and DOC- Pareto front (from 12.2 mK and above), the engine parameters see little change.

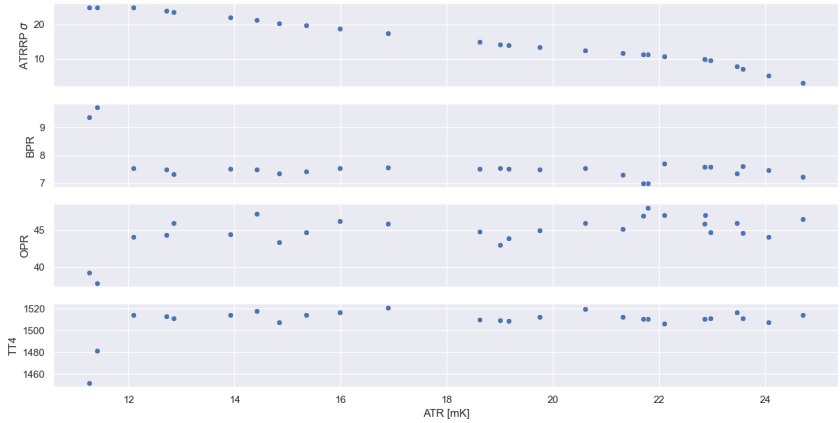

Figure 7.7: Change in operational design variable values for the Pareto-optimal set of designs from the ATR & DOC multi-objective optimization

Airframe Design Variables

The observed trends in the airframe design variables are displayed in Figure 7.8. A significant decrease in wing loading from 6.09 to 5.74 kN/m^2, in aspect ratio from 12 to 10, and in $C_{L,\text{max}}$ from 2.8 to 2.71, are observed observed in the initial phase of the ATR- and DOC- Pareto front, between 10.9 and 12.2 mK. These changes are likely a consequence of the increase in cruise Mach number, as was observed in Figure 7.6, hence requiring more sweep back. Higher sweep in turn reduces the allowed aspect ratio. The larger sweep back angle additionally reduces reduction in the allowable maximum lift coefficient, $C_{L,\text{max}}$.

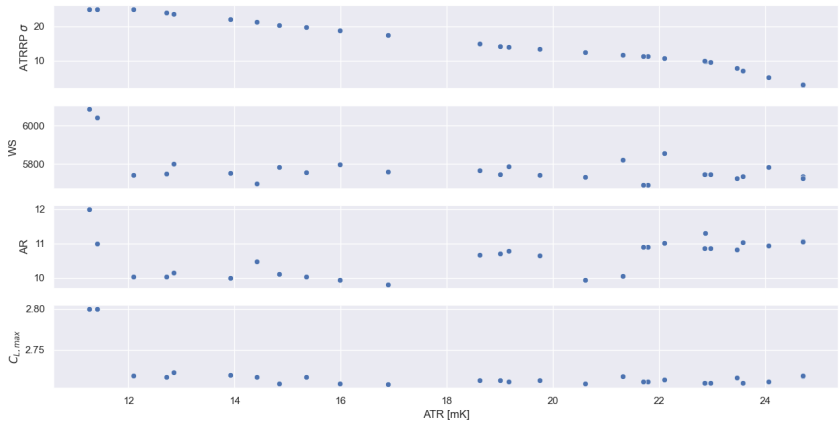

Figure 7.8: Change in operational design variable values for the Pareto-optimal set of designs from the ATR & DOC multi-objective optimization

The question remains whether at a given ATR, the ATRRP σ can further be reduced. This justifies the next stage of the uncertainty investigation, where a robustness based optimization is performed to find the Pareto-optimal solutions for minimal ATR and ATRRP σ.

7.3. Robustness-Based Optimization Results

The RBDO is carried out using the NSGA-II, to find the Pareto optimal front in the trade-off between ATR and ATRRP. This serves to answer the question of what aircraft design modification can be made to improve the robustness of the climate-optimized aircraft design. The optimizer parameters are specified in Table 5.2. The population was initialized using the Pareto set of design solutions belonging to the ATR- and DOC- multi-objective deterministic optimization, as given in Figure 7.3. The algorithm was allowed to iterate over 15 generations, for a population size of 50. The Pareto front to which the population converges to is compared to the initialized population in Figure 7.9. The blue line is indicative of the initial population, and the orange line is indicative of the robust Pareto optimal set of solutions.

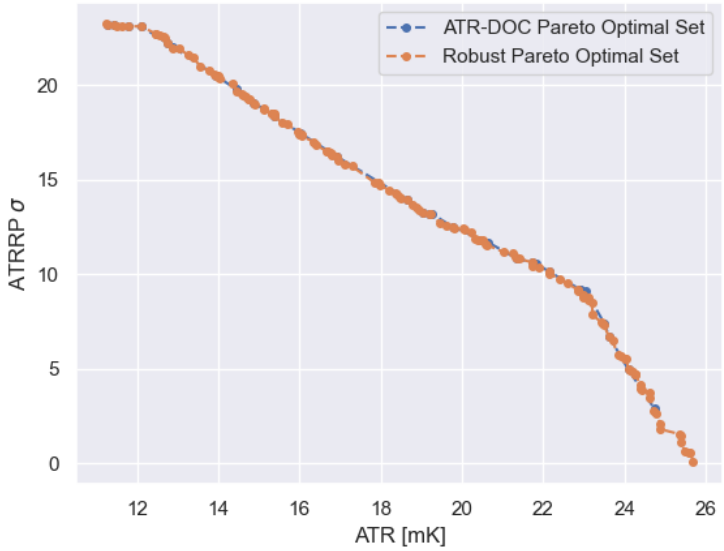

Figure 7.9: Pareto frontier set of robust climate-optimized solutions

From Figure 7.9, it is observed that the Pareto front belonging to the initialized set of solutions clearly coincides with the Pareto front belonging to the robust-optimized design points. Hence, it is evident that the GA was not capable of finding design solutions that provide improvement from a robustness perspective compared to the ATR- and DOC- Pareto optimal design solutions. The advancement in the Pareto front takes place at the extremes of the front. The first extreme of the robust Pareto front corresponds to the climate-optimal solution, while the second corresponds to the minimal ATRRP σ solution, which is identical to the minimal DOC- solution. This is to be expected, as the solution proving least uncertainty in climate impact reduction potential with respect to the cost-optimal aircraft is the cost-optimized aircraft itself. The change in aircraft design between the initialized and robustness-optimized sets are presented, with respect to operational, engine, and airframe design variables, in 7.10a, 7.10b, and in 7.10c, respectively. Due to negligible change in objective value change throughout the robustness-based optimization, the change in design variable values is likewise very small. The full set of objective function and design variable values for the robust-optimal Pareto set are provided in Table C.

The manner in which robustness improvement was expected to be attained was through trading off ATR of species having small ATRRP uncertainty, such as CO 2, with components presenting larger uncertainty in ATRRP, such as contrails and NO_x. The larger uncertainty in temperature response of NO_x and contrails is verified in their respective ATRRP 90% likelihood ranges presented in Table 7.5. Having greater contribution towards total ATR from species having high uncertainty would signify that the ATRRP of those components is smaller, and hence the overall ATTRP uncertainty is reduced. It would have been expected for the ATR contributions of both contrails and NO_x to be increased simultaneously as their respective ATR contribution increase is correlated, whilst the CO_2 ATR contribution is inversely correlated, especially for total ATR values greater than 12.2 mK. These correlations are

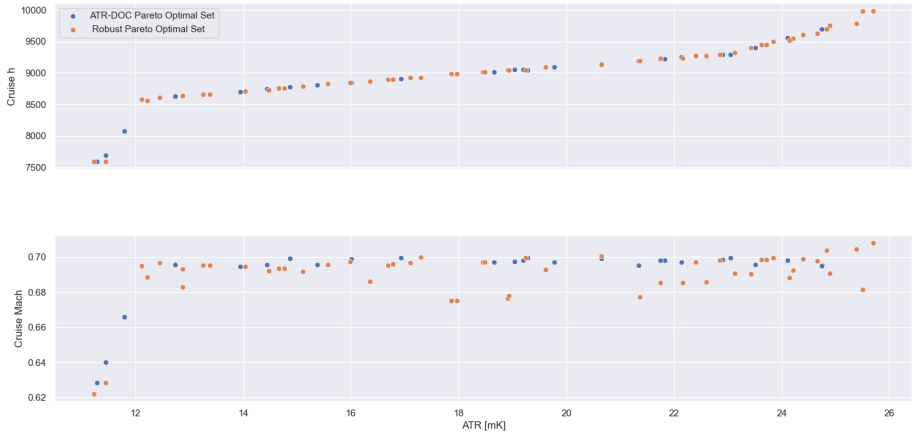

(a) Operational Design Variables

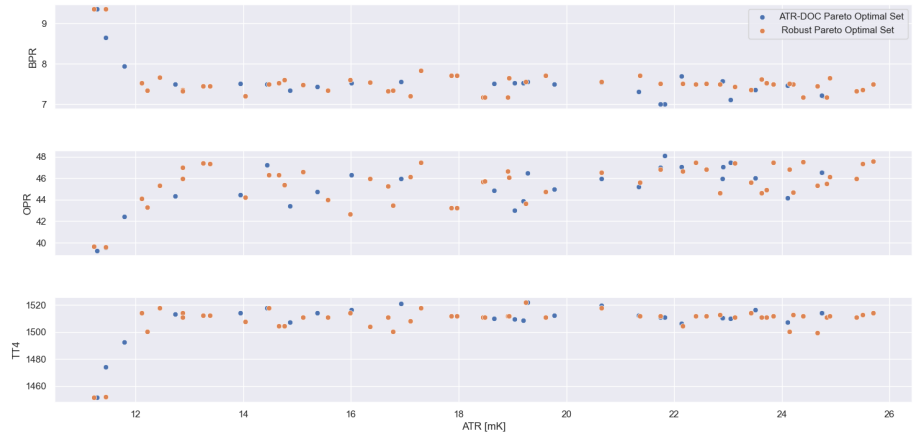

(b) Engine Design Variables

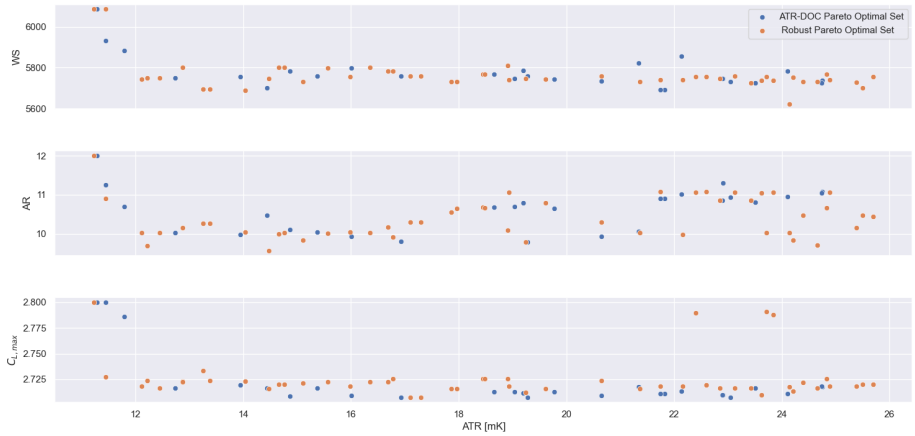

(c) Airframe Design Variables

Figure 7.10: Change in design variable values for the robust Pareto-optimal population compared to the ATR & DOC multi-objective optimization set of solutions

shown in Figure 7.5. It is evident however that the optimizer was not able to achieve this robustness improvement.

7.3.1. Optimal Solution Selection

The question of what aircraft design changes would give most optimal trade off of ATR reduction potential and robustness is now looked into. Ro order select an optimal solution from the array of Pareto optimal solutions, the *GRA* and *TOPSIS* methods are implemented. This is due to their simplicity, applicability, and lower number of required user inputs [77]. Both methods suggest that the ideal solution is found at the extremes of the Pareto front, i.e. at the corresponding single-objective optimization solutions for minimal ATR and DOC. This is shown in 7.11a and 7.11b. This is plausible since the Pareto front is concave, as can be observed in Figure 7.9. This signifies that the nearest distance to the ideal point, being the combination of the best value of each objective in the set of Pareto solutions, is at the extremes points.

When using the TOPSIS method, a range of weights are assigned, representing the relative importance of the climate impact objective over the robustness objective. (a) shows that for weights of 0.7 and above, the ATR-optimized design solution results as the optimal design. For relative weights of 0.6 and below, the minimal σ solution, corresponding to the DOC-optimized design point, is optimal. Hence for equal preference of criteria, minimal σ solution is favorable. When using the GRA method, the ATR-optimized design solution results as the optimal solution, as shown in (b). It can be inferred that the there is no design solution to the multi-objective optimization problem that would give a more optimal trade-off between ATR and ATTRP σ than the single-objective optimization solutions for minimal ATR and DOC.

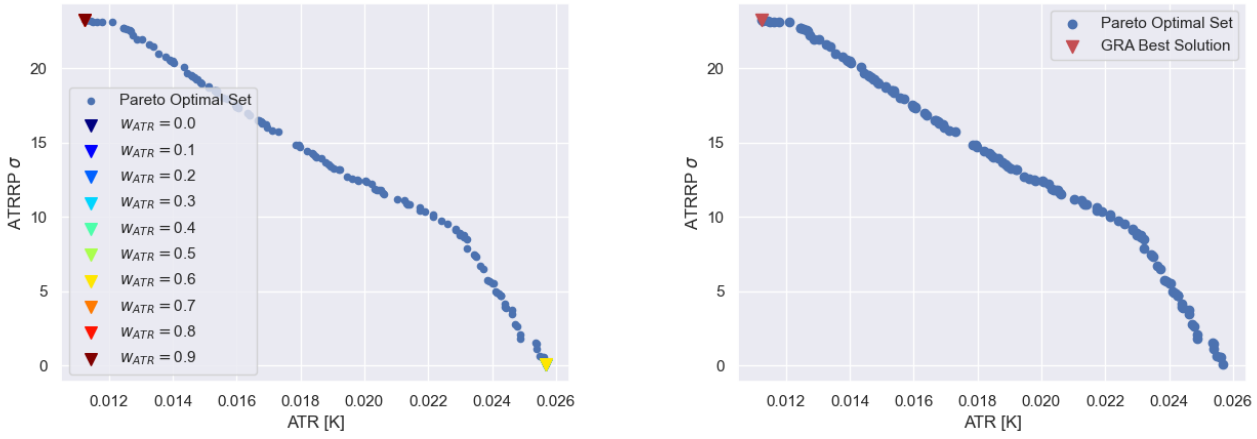

(a) TOPSIS method

(b) GRA method

Figure 7.11: Selection of optimal solutions from Pareto set using TOPSIS and GRA methods

In order to choose optimal solutions it was instead decided to further investigate performance an array of design points from the robust Pareto set of solutions. These points correspond to the midpoint and endpoints of the three phases of the Pareto front, as identified in Figure 7.4. The performance indicators of the optimized design at various stages of the Pareto front, utilizing the climate- and cost-optimized solutions as references, are laid out in Table 7.6. The table furthermore presents the changes in design variables values. It was shown that the robustness-optimized set of solutions did not show any meaningful change with respect to the set of solutions belonging to the ATR- & DOC- Pareto optimal set of solutions. Hence the discussion of the change in operational, engine, and airframe design variable values across the ATR- & DOC- Pareto optimal set of solutions presented in Section 7.2.1 directly applies to the values presented here for the array of robust solutions.

For the array of solutions, the objective functions values are furthermore traded off against the operating costs. The optimality of the trade-off between ATR, ATRRP σ, and DOC is quantified making use of the GRC metric. The greater the value of GRC, the closer the solution is to the ideal, defined

as the point having the minimal value found for each objective out of the complete set of solutions. As shown in Table 7.6, from the array of robust solutions, the GRC is highest for the robust solution # 1, at ATR=12.2 mK. Compared to the climate-optimized aircraft, this design point comprises of an increase in cruise altitude to 8.5 km, where contrail formation just start occur. Cruise Mach and OPR are additionally increased to 0.69 and 43.3, respectively. This drives marginal increase in CO_2, and NO_x ATR, while significantly reducing the block time and hence cutting the operating costs by 8.6 %.

Table 7.6: Change in objective function value, operating cost, design variables, and aircraft design performance indicators of selection of solutions from the robust climate-optimal Pareto of solutions

		Climate-optimized solution	Robust Solutions #1	#2	#3	#4	Cost-optimized solution
Objective Function Values	Total ATR$[mK]$	10.9	12.2	17.3	23.1	24.4	25.4
	ATRRPσ	25.0	24.8	16.8	9.31	4.45	0
Operating Cost Trade-Off	DOC$[USD/pax \cdot nm]$	0.140	0.128	0.127	0.128	0.127	0.126
	GRC	0.0385	0.0443	0.0429	0.0418	0.0420	0.448
Design Variables	Cruise h [km]	7.54	8.56	8.93	9.32	9.60	9.98
	Cruise M	0.600	0.689	0.700	0.691	0.699	0.700
	BPR	10.7	7.35	7.81	7.44	7.17	7.00
	OPR	45.7	43.3	47.5	47.4	47.5	44.3
	TT4 [K]	1479	1500	1517	1510	1511	1530
	W/S $[kN/m^2]$	6.06	5.70	5.76	5.56	5.73	5.65
	AR	11.6	9.70	10.3	11.1	10.5	11.1
	$C_{\text{L,max}}$	2.8	2.72	2.71	2.72	2.72	2.80
Performance Indicators	MTWO [metric tons]	66.6	66.1	66.2	65.7	65.8	65.4
	OEM [metric tons]	35.9	34.8	35.5	35.2	35.1	34.9
	$S[m^2]$	108	112	113	112	113	114
	$(L/D)_{cr}$	18.2	17.0	17.6	18.1	18.0	18.5
	$(T/W)_{TO}$	0.316	0.311	0.312	0.311	0.309	0.295
	$TSFC_{cr}[10^{-5}kg/(Ns)]$	1.44	1.60	1.57	1.57	1.59	1.61
	$N_{\text{AC, max}}$	16635	15280	15168	15360	15281	15315

7.3.2. Separate GA Run using 40 Generations

A separate RBDO was conducted, utilizing the NSGA-II utilizing the same parameters as indicated in Table 5.2. However, the generation size was increased from 15 to 40. Contrary to current RBDO results, improvement in robustness was observed. Although robustness change is very small in magnitude, comparatively significant changes were observed in design variable values, which are hence worth discussing. However, the algorithm did not converge after 15 generations as was proven for the current RBDO results (as verified in Figure 6.4. The hyper volume showed linear increase throughout the entire span of the algorithm iterations. Larger number of generations the NSGA-II would be required in order to present converged results, which however would fall outside the time frame of this research. Since convergence was not fully achieved, a qualitative, rather than quantitative, description of the results is provided in this subsection.

After 40 generations, the Pareto front showed improvement in the robustness dimension (ATRRP σ), ranging from 4 to 6 % for ATR values larger than 12.2 mK. The ATR component of less uncertain species such as CO_2 are traded off for ATR components of more uncertain species such as contrails, thereby obtaining robustness improvement. CO_2 ATR, proportional to fuel consumption, was reduced by the optimizer by significantly reducing cruise Mach from 0.695 to 0.638 (thereby reducing the SFC), and in addition choosing significantly larger values of $C_{L,\text{max}}$ and AR. The latter changes reduce the lift induced drag and hence fuel consumption at the low velocities. The increase in contrail and NO_x ATR was attained by increasing marginally the cruise altitude by less than 0.1 km for the Pareto set of solutions, thereby increasing the species forcing factors. Additionally, selecting larger BPR (from 7.5 to 9.4), specifically in ATR ranges between 12.2 and 15.5 mK, increases the propulsive efficiency and probability of contrail formation.

The improvement in robustness, however, comes at a price. Deterioration in the operating cost is

observed for the Pareto set of solutions giving the reported robustness improvement, with the DOC increasing by approximately 7 %. Hence the increase in DOC is- marginally greater than the increase in robustness. Moreover, with DOC being a primary design objective for aircraft designers, the price for the small gain in robustness would not be justified.

7.4. Sensitivity Analysis Results

The sensitivity analysis results are subdivided into GSA and LSA results, presented in Section 7.4.1 and Section 7.4.2 respectively.

7.4.1. Global Sensitivity Results

The GSA looks at identifying and quantifying the impact of main sources of uncertainty towards the ATRRP variability of the climate-optimized aircraft design and the selected robust design solutions defined in Table 7.6. The two-step approach is used for the GSA in order to limit the required computational cost. The key uncertain climate impact model parameters using the Morris method are identified, after which their contribution towards the output variance are quantified using the Sobol method. The number of repetitions r for the Morris analysis is set to 100. For the 10 most influential parameters, the Sobol analysis is carried out using a Monte Carlo sample size n of 1024, thereby requiring $n(10+2) = 12288$ climate model evaluations. Running the GSA on the full set of parameters would require $n(32+2) = 34816$ model evaluations, hence the computational cost is reduced by approximately 75% by utilizing the two-step approach. The GSA results showing the Morris rank, μ^* and Sobol first and total sensitivity indices for all scenarios are presented in Figure 7.12.

The GSA results of all design solutions show that the Morris rank, represented by μ_*, is indicative of total and first order ranks of Sobol indices. For the climate-optimized aircraft design solution, the contrail radiative efficiency A_{AIC} is shown to be the single predominant source of uncertainty. Other parameters having contribution are the altitude-dependent contrail radiative efficiencies $\frac{RF_{AIC}}{L_{ref}}(h)$, at altitude levels 2 and 3 (h = 7.5km, h = 10.5km), as well as the contrail efficacy, f_{AIC} and radiative forcing due to doubling of atmospheric CO_2 concentration compared to pre-industrial times, RF_{2xCO_2}. These contributions however are comparatively very small, as the sum of their ST and $S1$ are less than 10 % percent of that of the sum of all sensitivity indices.

The robust solution # 1 displays near identical GSA results as the climate optimized aircraft. The added contributions towards the ATR due to CO_2 and NO_x emissions for the robust solution # 1 hence do not show any change in the input parameters' relative importance towards the ATRRP uncertainty. This again reflects how NO_x and CO_2 input parameter importance is far outweighed by the contrail terms.

At robust solution # 2 (ATR = 17.3 mK), the contrail radiative efficiency prevails as one of the main influential parameters. However, relative to the rest of the parameters, the forcing factor at altitudes levels 2 and 3 show to have growing influence. This is explained by the fact that unlike the climate optimized aircraft, the robust aircraft is flying at an altitude where persistent contrails are formed, and hence the forcing factor at altitude levels 2 and 3 directly affect the variability in the contrail ATR term.

For robust solution # 3 ($ATR = 23.1mK$) and # 4 ($ATR = 24.4mK$), the growth in relative importance of contrail forcing factors at levels 2 and 3 is continued. Whilst the sensitivity index of contrail radiative efficiency A_{AIC} is now smaller than the contrail forcing factors, it remains an important source of uncertainty. The difference between total and first order indices of the contrail radiative efficiency, representing the degree of interaction with other parameters, is close to 50 % of the ST, whilst in prior solutions was negligible. Relative importance of interaction effects, with other terms involved in the contrail ATR computation, such as forcing factors and efficacy, are more significant compared to previous robsut solutions.

7.4.2. Local Sensitivity Analysis

In the second stage of the sensitivity analysis, a local sensitivity analysis is carried out to measure the impact of different future global CO_2 concentration scenarios (RCPs) on the ATRRP. Table 7.7 gives the change in ATR for the DOC- and ATR- optimized designs, the resultant ATRRP computed for various RCPs, and the ATRRP when normalized by the ATR of the DOC-optimized aircraft design.

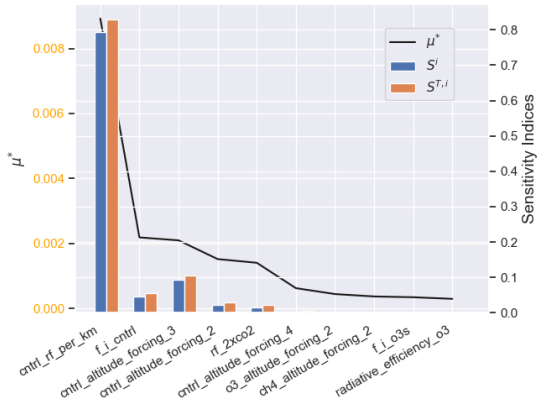

(a) Climate-optimized Solution, ATR = 10.9 mK, σ = 25.0

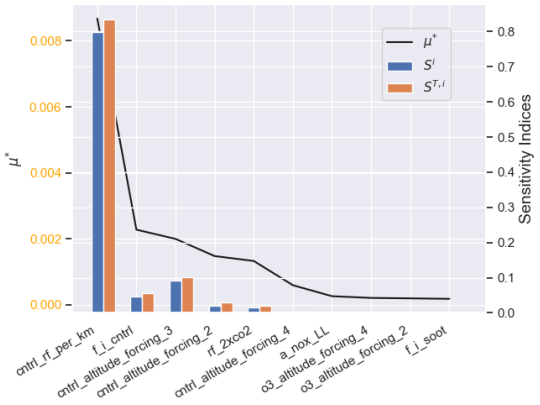

(b) Robust Solution 1, ATR = 12.2 mK, σ = 24.8

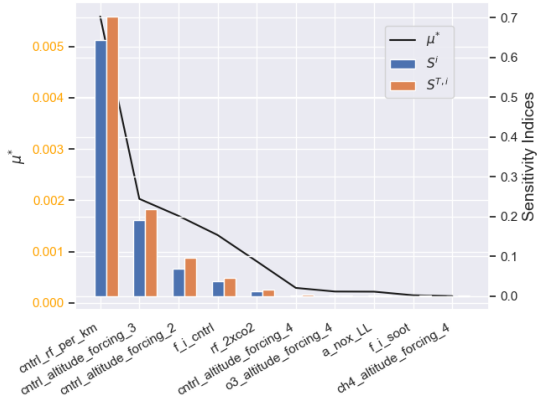

(c) Robust Solution 2, ATR = 17.3 mK, σ = 16.9

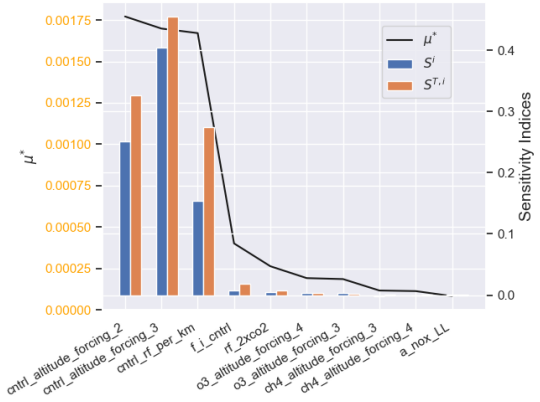

(d) Robust Solution 3, ATR = 23.1 mK, σ = 9.31

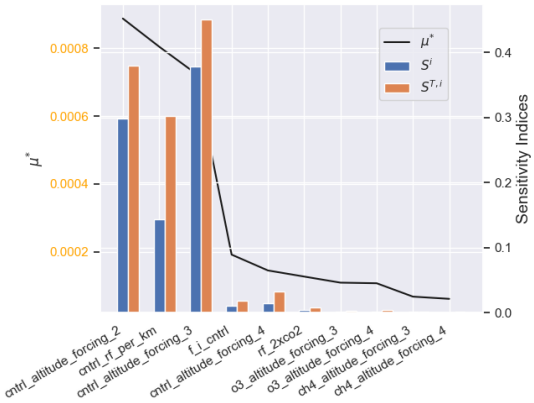

(e) Robust Solution 4, ATR = 24.4 mK, σ = 4.45

Figure 7.12: Global Sensitivity Analysis Results using the Morris method and the Sobol variance based method showing the most influential uncertain parameters with respects to the ATRRP σ for the different robust climate-optimized aircraft designs

Table 7.7: Change in ATR and ATRRP for different averafe global atmospheric CO_2 concentration scenarios

Representative CO_2 Concentration Pathway (RCP)	ATR (DOC-optimized) $[mK]$	ATR (climate-optimized) $[mK]$	ATRRP $[mK]$	ATRRP (Normalised)	ATRRP σ (Normalised)
Constant CO_2	0.0255	0.0109	0.0146	0.569	25.1
RCP 2.6	0.0246	0.0101	0.0145	0.559	26.0
RCP 4.5	0.0223	0.0145	0.0146	0.654	28.5
RCP 6.5	0.0218	0.0146	0.0146	0.672	29.3
RCP 8.0	0.0196	0.00534	0.0147	0.746	32.5

Although absolute change in ATTRP stays constant, variation future projected global atmospheric CO_2 concentration $\chi_{CO_2,0}$ decreases the CO_2 contribution to the total ATR for both the DOC- and climate- optimized aircrafts by up to 50% compared to the constant CO_2 scenario. This is shown in Table 7.7. Although this is a considerable sensitivity, the absolute ATRRP experiences a negligible change of 1.5 %. This is due to since CO_2 contribution remaining roughly the same for both aircraft designs. However, normalising the ATRRP gives a more notable increase of 33.5 %. The normalised ATRRP σ, likewise, increases by a similar order of magnitude. The scenario uncertainty, hence, largely influences the estimation of the relative ATRRP for a given climate-optimized aircraft design, as well as the relative variability due to lack scientific level of understanding.

The question remains of how variation in global atmospheric CO_2 concentration scenario would affect the RBDO results, given the RBDO was performed assuming using a constant atmospheric concentration. It was shown here that a reduction in atmospheric CO_2 concentration considerably reduces the estimated CO_2 ATR. It would also signify that aircraft design changes that lead to changes in CO_2 emissions, now have smaller relative impact on the ATR. To be recalled is the fact that the expected manner in which the RBDO would find robustness improvement is by trading off a portion of low-uncertainty CO_2 ATR for more uncertain NO_x or contrail ATR. Therefore the loss in sensitivity of ATR to CO_2 emission due to the increase in global atmospheric CO_2 concentration would not help the achieve this improvement in robustness. Hence the RBDO results are expected to remain unchanged with respect to those observed in this study.

8

Conclusions and Discussion

8.1. Conclusions

The objective of this research was to evaluate the robustness of the climate optimized medium-range single aisle turbofan aircraft design by identifying and quantifying the aircraft emission and climate modelling uncertainties and evaluating their impacts on the Multidisciplinary Design Optimization study. This was successgully carried out by answering the research question and respective sub-question, which for clarity are re-stated below along with the found outcomes.

1. Based on present day level of scientific understanding, what is the uncertainty in ATRRP of the climate optimized aircraft design?

   (a) What is the 90% likelihood range in the normalized ATRRP of the climate optimized aircraft design?

   The development of a summary of best estimates and probabilistic description of uncertain parameters of the Linear Climate Model (LCM) based on the present day level of scientific understanding was first carried out. Scientific uncertainty is identified for the carbon impulse response function parameters, species radiative efficiencies, the NO_x and contrail altitude forcing factors, methane perturbation lifetime, and species efficacies. Uncertainty analysis is implemented using Monte Carlo simulations, showing that the variability in the ATRRP is significant, having a 90% likelihood ranging between 17.2 and 98.9 % of cost optimized aircraft ATR as computed in the deterministic case.

   (b) What is the confidence interval of the emission species normalized ATRRP for the climate optimized aircraft design?

   The ATTRP uncertainty is predominantly largest for the contrails, having a 90% likelihood range for the ATRRP spanning from 11.9% to 95.2 % of cost optimized aircraft ATR as computed in the deterministic case. ATRRP of NO_x and CO_2 additionally have significant uncertainties, although being an order of magnitude smaller than that of contrails. The size of the uncertainty range is driven by the absolute magnitude of the ATRRP of the species.

   (c) How does the confidence interval in ATRRP vary throughout the different Pareto-optimal aircraft designs in the trade-off between ATR and DOC?

   Uncertainty analysis is carried out on the set of Pareto-optimal aircraft design solutions belonging to the trade-off between ATR and DOC. For initial ATR increase of 10.9, 12.2 mK, negligible change in ATRRP uncertainty is observed. For ATR values above 12.2 mK, the ATR increase coincides with increase in the contrail ATR, which in turn is shown to linearly correlate with the ATRRP σ decrease.
2. What aircraft design modifications can be made to improve the robustness of the climate optimized aircraft design?

(a) For the set of Pareto optimal solutions of the multidisciplinary optimization of ATR and ATRRP standard deviation, what is the relationship between design variable values and of ATRRP variability?

A heuristic approach using a genetic algorithm was implemented for the robustness-based optimization. Compared to the design solutions belonging to ATR- and DOC- Pareto optimal set, the RBDO was not capable of finding design solutions that provide improvement from a robustness perspective. Hence, the design variables of the RBDO solutions likewise comparatively did not differ substantially. The ATR increase is shown to be linearly correlated with the ATRRP σ decrease, when operating conditions allow for contrail formation, namely at cruise altitudes above 8.5 km. The growing forcing factor and probability of formation of contrails with increasing cruise altitude drives the increase in ATR and decrease in ATTRRP σ. At cruise altitudes below 8.5 km, the ATR increase is caused by increases in NO_x and CO_2 emissions, both driven by increases in cruise Mach, OPR, and TT4. However this is shown to have negligible influence on the overall variability in ATRRP .

(b) What robust design solutions would provide optimal performance when further traded off with DOC?

An array of solutions reflecting different decision maker preferences in the trade-off between climate impact and robustness are identified. When further trading off performance of the solutions with operating costs, the robust solution having ATR of 12.2 mK is found most optimal. Compared to the climate-optimized aircraft, this design point comprises of an increase in cruise altitude to 8.5 km, where contrail formation just start occur. Cruise Mach and OPR are additionally increased to 0.69 and 43.3, respectively.

3. What are the most relevant sources of uncertainty to the performance of the climate optimized aircraft design?

(a) What is the composition percentage of the variance in ATR reduction attributed to the different uncertain inputs?

A GSA was firstly implemented to quantify the apportion of ATRRP σ variance according to the climate impact model input parameters for the set of robust Pareto optimal points. The uncertain parameters showing largest influence on the output variability are the contrail-related radiaitive efficiency and forcing factors. For all analysed robust solutions, the proportion of first and total order sensitivity indices due to these parameters is more than 90 %.

(b) What is the sensitivity to variation in average global atmospheric CO_2 concentration projections within the year 2100?

An LSA is performed to analyse the impact of scenario uncertainty in the background CO_2 concentration level on the ATRRP of the climate-optimized design. Although absolute change in ATTRP stays constant, future global atmospheric CO_2 concentration projections decrease the CO_2 contribution to the total ATR for both the DOC- and climate- optimized aircrafts by up to 50% with respect to the constant global atmospheric CO_2 concentration scenario.

8.2. Discussion

This section looks to answer the question of to what extent one can safely apply the conclusions from this study for future conceptual aircraft design endeavors. In addition, the question of what research efforts are to be undertaken in order increase the confidence in results is resolved by providing research recommendations. Firstly, the limitations of the linear climate model (LCM) used in the study is assessed, which is followed by the limitations of the uncertainty characterisation method. Lastly, a discussion on the sources of scientific uncertainty that require most research effort are discussed.

8.2.1. Linear Climate Model Development

In order to evaluate the results obtained in this study, one must highlight the inaccuracies currently existing in the methodology used for computing the RF response due to contrails. As the GSA demonstrated, the terms associated with the contrail RF estimation have largest influence on the uncertainty on the performance. Hence the development of a more accurate contrail RF estimation is required in order to increase confidence in future climate optimization design study results.

The inaccuracy pertains to the formulation of the radiative efficiency parameter, A_{AIC}, and forcing factor parameter, s_{AIC}, inside the LCM used to compute the contrail RF. A_{AIC} currently is derived from the report by Lee et al. (2021) [37], which expresses the average global RF of global aviation due to linear contrails and cirrus cloudiness arising from them, per unit distance travelled [37]. The LCM used in the current study however requires A_{AIC} to be expressed per unit of linear contrail coverage instead of distance travelled, since the term is multiplied by the computed total linear contrail distance of the aircraft operation. Consequently, the forcing factor must characterise the deviation of the globally averaged RF per unit of linear contrail coverage as function of altitude. In the current formulation, as derived from the data obtained by Radel and Shine (2008) [56], the normalization is performed using the flown distance as function of altitude.

The first implication of this incorrect formulation of the parameters is that the radiative efficiency parameter A_{AIC} is underestimated. The second implication is that the forcing factor is greatly overestimated at altitudes where deviation of RF response from the global average is positive, and is underestimated in regions where the opposite holds true. This is the case because the deviation from globally averaged RF per flown kilometre with altitude is mainly due to variation in persistent contrail formation probability, rather than change in radiative transfer properties. In light of the aforementioned source of inaccuracy in the contrail RF estimation method, it is recommended for contrail radiative efficiency, A_{AIC} and forcing factor $s_{AIC}(h)$ to both be evaluated as function of contrail coverage distance, instead of the total distance flown.

8.2.2. Uncertainty Characterisation Methodology Recommendation

The employed uncertainty characterisation method aims at accurately identifying and quantifying the uncertainties incorporated in the usage of the LCM for the forwards looking climate impact assessment. The accuracy of this method however will have implications on the overall validity of the method. Some of the identified shortcomings of the current uncertainty characterisation method are discussed here.

The first concern with regards to the current uncertainty characterisation is related to the formulation of the RF computation within the LCM, previously discussed in Section 8.2.1. As suggested, a radiative efficiency parameter that is normalised by the linear contrail distance would require its uncertainty to likewise reflect only the radiative response to the presence of contrails cirrus. This would only include uncertainty in the radiative transfer scheme and the in-homogeneity of ice clouds within the grid box as implemented in the GCMs [37]. The uncertainty regarding the derived contrail cover would need to be imposed on the 3 criteria used for determination of formation of persistent contrails at each phase of the flight profile. The first criteria is the Schmidt-Appleman criteria, requiring the exhaust air to reach saturation with respect to water vapour in the mixing process in order for contrail formation to occur. Secondly, the ambient static temperature is required to be below 235 Kelvin. Lastly, for contrail formation to persist, the mixed exhaust must have a relative humidity with respect to ice of more than 100%, i.e. supersaturation. Application of this contrail prediction model is believed to be limited by its reliance on accurate input data [13]. To quantify the uncertainty, a recommendable method would be to assign probabilistic description to the contrail formation prediction model inputs. These firstly include the engine propulsive efficiency η, used to determine the mixing line of exhaust for the Schmidt-Applmena criteria. Secondly are the combustion parameters: emission index of water EI_{H2O}, specific combustion heat of jet fuel, Q, again required to determine the Schmidt-Appleman criteria. Thirdly are the atmospheric conditions predicted via ISA relations namely the total pressure p and temperature T_a. Lastly, the relative humidity RH, which currently is assumed constant.

The second shortcoming of the uncertainty characterisation method is the fact that currently it is only aimed to quantify the degree of scientific and scenario uncertainty within the input parameters of the LCM. However the degree of modelling uncertainty is not taken into consideration. This relates to the impact of inexact modelling approach for estimating the climate impacts. LCMs replicate the globally averaged results of the Global Climate Models (GCMs) on which they are based. As only first-order effects are captured, they greatly simplify the physics and chemistry of aircraft-induced climate change.

Effects of varying background concentrations, latitude and longitude, timing, and interaction with other pollutants not measured [65]. Hence additional modelling uncertainty is to be considered, and lack thereof suggests that the current quantified uncertainty in ATRRP of the climate optimized aircraft may be underestimated.

In terms of the uncertainty characterisation methodology use to ”

8.2.3. Future Uncertainty Reduction Work

A benefit of the GSA carried out in this study is that it identifies what the most influential uncertain parameters are. This gives an indication of where further reduction in scientific level of understanding can give most additional confidence in climate impact aircraft optimization, and hence communicate the areas in which further research is needed.

The radiative efficiency and forcing factor parameters, in the manner they are currently implemented in the LCM, are identified as having largest impact to uncertainty. Hence those parameters are primarily discussed. The sources of uncertainty of radiative efficiency is connected with the upper tropospheric water budget and contrail prediction scheme, and secondly with the radiative response to the presence of contrail and cirrus cloudiness. The sources of uncertainty related to the former, as identified in the report by Lee et al. (2021) [37], are as follows:

- Knowledge of the ambient conditions where contrails are observed, due to the low vertical resolution of the satellite imaging. This leads to poor ability to statistically predict supersaturation conditions.
- Ice crystal number of young contrails being dependant on the level of water supersaturation and soot emissions.
- The adjustment of natural clouds due to the presence of persistent contrails.
- Dependence of contrail cirrus RF estimate on the initial contrail ice crystal radii and cross sectional areas.

The sources of uncertainty related to the radiative response to the presence of contrails are [37]:

- Uncertainty in the radiation scheme within the GCMs
- Effect of the overlap contrail-cloud and contrail-contrail overlap on the RF response [60]
- The estimation within GCMs of the RF due to very small ice crystals ($< 5\mu m$)

These sources of uncertainty are common also to contrail forcing factor uncertainty. However the the computation of contrail cover by Radel & Shine (2008) to derive the forcing factor does not utilize the full process-based simulation of the micro-physical processes and contrail spreading as utilized in study by Lee et al. (2021) to derive the AIC radiative efficiency [56]. Instead, only the probability of ice supersaturation is used to predict contrail formation, which is then multiplied by a normalization factor so that it yields the observed cover from available satellite measurements. Hence an important additional uncertainty comes into play, related to the sparseness of the satellite measurements[56]. To reduce this source of uncertainty, the computation of contrail formation as function of altitude requires to be evaluated using the same process-based simulation approach as utilised by Lee et al. (2021) [37].

Lastly we discuss NO_x. Whilst the GSA suggested that NO_x components to have negligible impact to output uncertainty, the Morris analysis still included their impacts in the top 10 parameter rank. The current uncertainty estimates are based on study by Lee et al. (2021), where variability due to inter-model differences of numerous GCMs, as well as differing global emission inventories are quantified [37]. For the forward-looking climate impact analysis in this study however, it should only be required that the uncertainties of the NO_x terms evaluate the inter-model differences of the GCMs. In order to quantify the uncertainty in the NO_x emissions, it would be necessary assign a separate probabilistic description to the NASA ECCP semi-empirical analytical model used to estimate the NO_x EI. This would call for the need of an experimental study of the predictive performance of the model, as function of altitude, specific humidity, and thrust setting.

Future CO_2 Atmospheric Concentration Scenario The results from the LSA (Section 7.4) gave indication that the scenario uncertainty pertaining to the future atmospheric CO_2 concentration has a

significant impact on the estimated contribution by CO_2 on the total ATR of the aircraft design. Hence for a potential aircraft where climate impact is minimized via carbon emission reduction, the sensitivity due to this scenario uncertainty is very significant. This calls for the need to develop a 'most likely scenario' together with an uncertainty range of the atmospheric CO_2 concentration at every year until the year 2120. A manner to do this by defining a most likely scenario and a likelihood range with use of an expert elicitation methods, for the inputs for the different assessment modules within the GCMs, used to estimate the RCPs. The modules are model representations of the global economy, energy systems, and agriculture and land use [45]. For example, an input for the global economy module would be the predicted growth in passenger kilometers in transport or space conditioning for buildings [9]. Although being a very complex endeavor, this would allow designers to have a more confident idea of the magnitude in which the scenario uncertainty impacts the estimated CO_2 temperature response of the proposed aircraft design.

A

Literature Overview of Linear Climate Model Uncertainty

Best estimates and likelihood ranges according to different sources in scientific literature are summarised in this chapter. Values for the emission indices are given in Table A.1. Values for carbon dioxide impulse response function parameters are given in Table A.3. Values of parameters related to NO_x-induced RF response are given in Table A.2. Values of parameters related to RF of short lived emission species, namely H_2O, CO, SO_4, and contrails, are summarised in Table A.4. Lastly, the values of species efficacy parameter for all emission species are provided in Table A.5.

Table A.1: Best estimates and likelihood range of the Emission Index (EI) of various emission species

Parameter	Best Estimate	Uncertainty Interval	Source	Distribution Source
EI (CO_2) [kg/kg fuel]	3.16	[3.148,3.173]	Barrett et al. (2010)	Barrett et al. (2010)
	3.155	N/A	Kim et al. (2007)	N/A
	3.16	Within 1 %	Lee et al. (2021)	Lee et al. (2021)
EI (NO_x) [kg/kg fuel]	Analytical expression (NASA's ECCP program)	+- 15 %	Lukachko (1997)	Lukachko (1997)
EI (Water Vapour) [kg/kg fuel]	1.247	N/A	Kim et al. (2007)	N/A
	1.238	N/A	Eyers et al. (2004)	N/A
	1.231	[1.197,1.258]	Barrett et al. (2010)	Barrett et al. (2010)
EI (Soot) [g/kg(fuel)]	0.025	[0.01, 0.1]	Lee et al. (2010)	Lee et al. (2010)
	0.03	[0.01, 0.07]	Lee et al. (2021)	Barrett et al. (2010)
EI (S02) [g/kg(fuel)]	0.2	N/A	IPCC (1999)	N/A
	0.8	[0.6,1.0]	Lee et al. (2010)	Lee et al. (2010)
	1.176	[0.752,1.592]	Wilkerson et al. (2010)	Barrett et al. (2010)
	1.2	[1.1,1.5]	Lee et al. (2021)	Barrett et al. (2010)

Table A.2: Best estimates and 90 % likelihood range of the radiative forcing response of NO_x

Parameter	Best Estimate	90% Likelihood Range	Source	Distribution Source
CO_2 Radiative Forcing [Wm^{-2}]	LinClim SCM	Normal: +- 20%	Sausen-Schumann (2000)	Sausen-Schumann (2000)
	Average of three SCMs (including LinCLim)	Normal: +- 15%	Lee et al. (2021)	Lee et al. (2021)

Table A.3: Best estimates and 90 % likelihood range of the radiative forcing response of Carbon Dioxide

Parameter	Best Estimate	90% Likelihood Range	Source	Distribution Source
Radiative efficiency (NO_x-O_{3S}) $[mWm^{-2}/(Tg(NOx))]$	10.1	lognormal: [32%-314%]	Sausen et al. (2005)	Lee et al. (2009)
	7.64	lognormal: [64%-155%]	Lee et al. (2021)	Lee et al. (2021)
Radiative efficiency (NO_x-Long term O_{3S}) $[mWm^{-2}/(Tg(NO_x))]$	-0.121	lognormal: [32%-314%]	Marais et al. (2008)	Lee et al. (2009)
	-0.200	lognormal: [70%-188%]	Lee et al. (2021)	Lee et al. (2021)
Radiative efficiency (NO_x-CH_4) $[mWm^{-2}/(Tg(NO_x))]$	-0.513	lognormal: [16.7%-600%]	Marais et al. (2008)	Lee et al. (2009)
	-0.401	lognormal: [70%-188%]	Lee et al. (2021)	Lee et al. (2021)
Radiative efficiency (NO_x-SWV) $[Wm^{-2}/(Tg(NO_x))]$	-0.0710	lognormal: [70%-188%]	Lee et al. (2021)	Lee et al. (2021)
Methane Perturbation Time (years)	12	normal: +-15%	IPCC (2007)	IPCC (2007)
	11.07	N/A	Marais et al. (2008)	N/A
Correlation Factor (Short term -Long term NO_x RF)	-0.5	N/A	Dallara (2011)	N/A
	-0.7	N/A	Lee et al. (2021)	N/A

Table A.4: Best estimates and 90 % likelihood range of the radiative forcing response of short lived emission species

Parameter	Best Estimate	90% Likelihood Range	Source	Distribution Source
Radiative efficiency (Statospheric H_2O) $[mWm^{-2}/(Tg(H_2O))]$	0.00743	lognormal: [13.8%,724%]	IPCC (1999)	Lee et al. (2009)
	0.00520	normal: [40%,160%]	Lee et al. (2021)	Lee et al. (2021)
Radiative efficiency (Sulphate) $[mWm^{-2}/(Tg(SO_4))]$	-100	lognormal: [16.5%,610%]	IPCC (1999)	Lee et al. (2009)
	-19.9	lognormal: [10.6%, 425%]	Lee et al. (2021)	Lee et al. (2021)
Radiative efficiency (Soot) $[mWm^{-2}/(Tg(CO))]$	50.0	lognormal: [16.5%,610%]	IPCC (1999)	Lee et al. (2009)
	101	lognormal: [35.1%, 256%]	Lee et al. (2021)	Lee et al. (2021)
Radiative efficiency (Contrail cirrus) $[Wm^{-2}/km(AIC)]$	1.19×10^{-12}	lognormal: [37.9%,263.4%]	Lee et al. (2009)	Lee et al. (2009)
	1.82×10^{-12}	normal: [29.%,169.7%]	Lee et al. (2021)	Lee et al. (2021)

Table A.5: Best estimates and Likelihood Range of Species Efficacy Values

	Best Estimate	**90% Likelihood Range**	**Source**	**Distribution Source**
f_{CO_2}	1	normal: [+-5 %]	Ponater et al. (2008)	Lee et al. (2021)
$f_{O_{3S}}$	1.37	66 % likelihood range: +-30%	Ponater et al. (2008)	Grewe & Stenke (2008)
$f_{O_{3L}}$	1.18	66 % likelihood range: +-30%	Lee et al. (2021)	Grewe & Stenke (2008)
f_{CH_4}	1.18	66 % likelihood range: +-10%	Ponater et al. (2008)	Grewe & Stenke (2008)
f_{H_2O}	1.14	66 % likelihood range: +-30%	Ponater et al. (2008)	Grewe & Stenke (2008)
f_{SO_4}	0.9	normal: [0.412,1.39]	IPCC (2007)	IPCC (2007)
	1	N/A	Lee et al. (2021)	N/A
f_{CO}	0.7	lognormal: [0.212,2.31]	IPCC (2007)	IPCC (2007)
	1	N/A	Lee et al. (2021)	N/A
f_{AIC}	0.59	66 % likelihood range: +-10%	Ponater et al. (2008)	Grewe & Stenke (2008)
	0.42	normal: +-40%	Lee et al. (2021)	Lee et al. (2021)

B

Sensitivity Index Value and Confidence Intervals

Climate-Optimal Solution, ATR = 10.9 mK

Table B.1: Top 10 most influential parameters for climate optimized Solution, with respective Morris elementary effect, first and total order Sobol Sensitivity Indices, and 90 % confidence intervals of estimates

Parameter	Morris μ^*	Morris μ^* Conf	S1	S1 Conf	ST	ST Conf
A_{AIC}	8.92e-3	3.13e-4	9.54e-4	2.79e-3	1.22e-3	1.79e-4
f_{AIC}	2.18e-3	1.25e-4	7.94e-1	7.94e-2	8.30e-1	7.08e-2
AIC altitude forcing 3	2.09e-3	2.46e-4	1.44e-3	3.50e-3	1.46e-3	1.54e-4
AIC altitude forcing 2	1.52e-3	1.30e-4	6.32e-4	2.42e-3	7.71e-4	1.49e-4
RF_{2xCO2}	1.40e-3	8.24e-5	2.14e-2	1.54e-2	2.86e-2	4.85e-3
AIC altitude forcing 4	6.20e-4	5.03e-5	9.46e-2	2.67e-2	1.05e-1	1.92e-2
O_{3S} altitude forcing 2	4.38e-4	3.11e-5	4.12e-3	6.17e-3	4.68e-3	7.02e-4
CH_4 altitude forcing 2	3.65e-4	2.05e-5	8.44e-4	2.20e-3	4.60e-4	7.18e-5
$f_{O_{3S}}$	3.41e-4	3.11e-5	4.54e-2	1.97e-2	5.51e-2	6.94e-3
$A_{O_{3S}}$	2.91e-4	2.44e-5	1.61e-2	1.22e-2	2.15e-2	2.47e-3

Robust Solution #1, ATR = 12.2 mK

Table B.2: Top 10 most influential parameters for robust solution at ATR=12.2 mK, with respective Morris elementary effect, first and total order Sobol Sensitivity Indices, and 90 % confidence intervals of estimates

Parameter	Morris μ^*	Morris μ^* Conf	S1	S1 Conf	ST	ST Conf
A_{AIC}	8.68e-3	2.85e-4	4.11e-4	1.69e-3	3.18e-4	3.53e-5
f_{AIC}	2.27e-3	1.28e-4	7.99e-1	8.10e-2	8.35e-1	7.08e-2
AIC altitude forcing 3	1.99e-3	1.30e-4	4.48e-4	1.59e-3	4.45e-4	4.98e-5
AIC altitude forcing 2	1.47e-3	1.02e-4	3.31e-4	1.92e-3	4.35e-4	5.01e-5
RF_{2xCO2}	1.33e-3	8.51e-5	2.11e-2	1.24e-2	2.90e-2	4.46e-3
AIC altitude forcing 4	5.90e-4	4.23e-5	9.09e-2	2.60e-2	1.01e-1	1.70e-2
O_{3S} altitude forcing 2	2.57e-4	9.58e-6	3.54e-3	5.53e-3	4.01e-3	6.19e-4
CH_4 altitude forcing 2	2.04e-4	1.81e-5	5.04e-4	2.52e-3	8.41e-4	1.97e-4
$f_{O_{3S}}$	1.91e-4	1.62e-5	4.57e-2	2.35e-2	5.55e-2	7.16e-3
$A_{O_{3S}}$	1.76e-4	1.23e-5	1.49e-2	1.13e-2	2.02e-2	2.39e-3

Robust Solution #2, ATR = 17.3 mK

Table B.3: Top 10 most influential parameters for robust solution at ATR=17.3 mK, with respective Morris elementary effect, first and total order Sobol Sensitivity Indices, and 90 % confidence intervals of estimates

Parameter	Morris μ^*	Morris μ^* Conf	S1	S1 Conf	ST	ST Conf
A_{AIC}	5.59e-3	1.72e-4	6.22e-4	1.96e-3	5.61e-4	5.21e-5
AIC altitude forcing 3	2.03e-3	1.77e-4	6.43e-1	7.35e-2	7.03e-1	6.88e-2
AIC altitude forcing 2	1.70e-3	1.63e-4	9.93e-5	1.60e-3	2.81e-4	4.94e-5
f_{AIC}	1.33e-3	8.22e-5	7.71e-4	2.64e-3	1.16e-3	1.31e-4
RF_{2xCO2}	8.13e-4	5.37e-5	6.84e-2	2.81e-2	9.55e-2	1.62e-2
AIC altitude forcing 4	2.94e-4	2.30e-5	1.91e-1	4.73e-2	2.18e-1	3.64e-2
O_{3S} altitude forcing 2	2.24e-4	1.54e-5	2.19e-3	4.59e-3	2.40e-3	3.90e-4
$A_{O_{3L}}$	2.21e-4	8.66e-6	-4.48e-4	2.91e-3	1.52e-3	3.03e-4
f_{soot}	1.51e-4	1.21e-5	3.69e-2	1.58e-2	4.64e-2	6.28e-3
CH_4 altitude forcing 4	1.34e-4	7.18e-6	1.11e-2	1.18e-2	1.67e-2	2.06e-3

Robust Solution #3, ATR = 23.1 mK

Table B.4: Top 10 most influential parameters for robust solution at ATR=23.1 mK, with respective Morris elementary effect, first and total order Sobol Sensitivity Indices, and 90 % confidence intervals of estimates

Parameter	Morris μ^*	Morris μ^* Conf	S1	S1 Conf	ST	ST Conf
AIC altitude forcing 2	1.77e-3	1.43e-4	2.24e-4	1.60e-3	3.30e-4	4.44e-5
AIC altitude forcing 3	1.70e-3	1.33e-4	1.53e-1	4.85e-2	2.74e-1	4.08e-2
A_{AIC}	1.67e-3	1.32e-4	-1.71e-3	2.18e-3	6.02e-4	8.68e-5
f_{AIC}	4.01e-4	3.48e-5	-8.44e-4	2.00e-3	5.51e-4	6.52e-5
RF_{2xCO2}	2.63e-4	2.49e-5	2.76e-3	4.72e-3	2.50e-3	3.30e-4
O_{3S} altitude forcing 4	1.92e-4	1.34e-5	3.46e-3	4.80e-3	2.83e-3	3.80e-4
O_{3S} altitude forcing 3	1.86e-4	1.13e-5	2.52e-1	4.86e-2	3.26e-1	4.10e-2
CH_4 altitude forcing 3	1.17e-4	7.77e-6	4.04e-1	9.34e-2	4.55e-1	7.39e-2
CH_4 altitude forcing 4	1.13e-4	7.09e-6	8.14e-3	1.43e-2	1.82e-2	2.68e-3
$A_{O_{3L}}$	8.29e-5	8.50e-6	4.30e-3	7.56e-3	6.95e-3	9.76e-4

Robust Solution #4, ATR = 24.4 mK

Table B.5: Top 10 most influential parameters for robust solution at ATR=23.1 mK, with respective Morris elementary effect, first and total order Sobol Sensitivity Indices, and 90 % confidence intervals of estimates

Parameter	Morris μ^*	Morris μ^* Conf	S1	S1 Conf	ST	ST Conf
AIC altitude forcing 2	1.77e-3	1.43e-4	2.24e-4	1.60e-3	3.30e-4	4.44e-5
AIC altitude forcing 3	1.70e-3	1.33e-4	1.53e-1	4.85e-2	2.74e-1	4.08e-2
A_{AIC}	1.67e-3	1.32e-4	-1.71e-3	2.18e-3	6.02e-4	8.68e-5
f_{AIC}	4.01e-4	3.48e-5	-8.44e-4	2.00e-3	5.51e-4	6.52e-5
RF_{2xCO2}	2.63e-4	2.49e-5	2.76e-3	4.72e-3	2.50e-3	3.30e-4
O_{3S} altitude forcing 4	1.92e-4	1.34e-5	3.46e-3	4.80e-3	2.83e-3	3.80e-4
O_{3S} altitude forcing 3	1.86e-4	1.13e-5	2.52e-1	4.86e-2	3.26e-1	4.10e-2
CH_4 altitude forcing 3	1.17e-4	7.77e-6	4.04e-1	9.34e-2	4.55e-1	7.39e-2
CH_4 altitude forcing 4	1.13e-4	7.09e-6	8.14e-3	1.43e-2	1.82e-2	2.68e-3
$A_{O_{3L}}$	8.29e-5	8.50e-6	4.30e-3	7.56e-3	6.95e-3	9.76e-4

C

Robustness-Based Optimization Results

Table C.1: Objective function and design variable values of the Pareto optimal set of solutions of the robustness-based climate optimization using 15 generations of the NSGA-II algorithm

ATR $[mK]$	ATRRP σ	$C_{L,max}$	WS	AR	BPR	PR$_{fan}$	PR$_{lpc}$	PR$_{hpc}$	TT4	Cruise h [m]	Cruise M
11.2	23.2	2.8	6087	12.0	9.36	1.44	1.51	18.2	1452	7590	0.622
11.5	23.2	2.73	6087	10.9	9.36	1.44	1.51	18.2	1452	7590	0.628
12.1	23.2	2.72	5744	10.0	7.53	1.64	1.48	18.2	1514	8578	0.695
12.2	23.1	2.72	5750	9.70	7.35	1.65	1.43	18.3	1500	8564	0.689
12.4	22.7	2.72	5750	10.0	7.67	1.66	1.50	18.1	1518	8609	0.697
12.9	22.3	2.72	5800	10.2	7.36	1.70	1.51	18.3	1514	8633	0.683
12.9	22.0	2.72	5800	10.2	7.33	1.67	1.51	18.3	1511	8641	0.693
13.3	21.6	2.73	5694	10.3	7.46	1.67	1.50	18.9	1512	8661	0.695
13.4	21.4	2.72	5694	10.3	7.46	1.67	1.50	18.9	1512	8661	0.695
14.0	20.4	2.72	5689	10.0	7.21	1.67	1.46	18.1	1508	8712	0.695
14.5	19.8	2.72	5747	9.56	7.50	1.69	1.50	18.3	1518	8726	0.692
14.7	19.4	2.72	5800	10.0	7.53	1.63	1.53	18.6	1504	8761	0.694
14.8	19.2	2.72	5800	10.0	7.60	1.63	1.50	18.6	1504	8762	0.694
15.1	18.8	2.72	5732	9.83	7.49	1.63	1.58	18.1	1511	8786	0.692
15.6	18.0	2.72	5797	10.0	7.35	1.64	1.48	18.1	1511	8822	0.696
16.0	17.5	2.72	5757	10.0	7.60	1.69	1.40	18.1	1514	8845	0.697
16.4	17.1	2.72	5800	10.0	7.54	1.67	1.51	18.3	1504	8866	0.686
16.7	16.5	2.72	5783	10.2	7.33	1.67	1.48	18.3	1511	8896	0.695
16.8	16.3	2.73	5783	9.91	7.35	1.65	1.43	18.3	1500	8894	0.696
17.1	15.8	2.71	5757	10.3	7.21	1.66	1.46	18.9	1508	8927	0.697
17.3	15.7	2.71	5759	10.3	7.83	1.66	1.51	19.0	1518	8927	0.700
17.9	14.8	2.72	5732	10.6	7.72	1.62	1.43	18.6	1512	8987	0.675
18.0	14.7	2.72	5732	10.6	7.72	1.62	1.43	18.6	1512	8987	0.675
18.5	14.1	2.73	5766	10.7	7.17	1.71	1.45	18.4	1511	9016	0.697
18.5	14.0	2.73	5766	10.7	7.17	1.71	1.45	18.4	1511	9018	0.697
18.9	13.6	2.73	5810	10.1	7.17	1.71	1.48	18.3	1512	9040	0.676
18.9	13.4	2.72	5739	11.1	7.65	1.67	1.48	18.7	1512	9045	0.678
19.2	13.2	2.71	5747	9.79	7.56	1.68	1.46	17.9	1522	9047	0.700
19.6	12.6	2.72	5744	10.8	7.72	1.63	1.48	18.6	1511	9095	0.693
20.6	11.6	2.72	5759	10.3	7.56	1.68	1.46	19.0	1518	9136	0.700
21.4	11.0	2.72	5732	10.0	7.72	1.71	1.43	18.6	1512	9189	0.677
21.7	10.4	2.72	5739	11.1	7.52	1.67	1.50	18.7	1512	9234	0.685
22.2	10.2	2.72	5739	10.0	7.52	1.67	1.50	18.6	1504	9234	0.685
22.4	9.8	2.79	5755	11.1	7.49	1.67	1.50	19.0	1512	9269	0.697
22.6	9.5	2.72	5756	11.1	7.52	1.67	1.50	18.7	1512	9269	0.686
22.8	9.2	2.72	5747	10.9	7.50	1.66	1.46	18.4	1513	9292	0.698
23.1	8.7	2.72	5759	11.1	7.44	1.69	1.50	18.7	1511	9316	0.691
23.4	7.5	2.72	5726	10.9	7.36	1.71	1.48	18.0	1514	9394	0.690
23.6	6.7	2.71	5737	11.0	7.62	1.68	1.45	18.3	1511	9451	0.699
23.7	6.5	2.79	5755	10.0	7.53	1.67	1.48	18.2	1511	9446	0.698
23.8	5.7	2.79	5738	11.1	7.49	1.67	1.50	19.0	1512	9501	0.699
24.1	5.5	2.72	5620	10.0	7.52	1.67	1.50	18.7	1500	9519	0.688
24.2	5.0	2.71	5754	9.84	7.50	1.66	1.46	18.4	1513	9542	0.692
24.4	4.1	2.72	5731	10.5	7.17	1.66	1.59	18.0	1512	9604	0.699
24.7	3.7	2.72	5732	9.70	7.46	1.67	1.50	18.1	1499	9625	0.698
24.8	2.9	2.73	5766	10.7	7.17	1.71	1.45	18.4	1511	9698	0.704
24.9	2.1	2.72	5739	11.1	7.65	1.67	1.48	18.7	1512	9757	0.691
25.4	1.5	2.72	5727	10.2	7.33	1.67	1.51	18.3	1511	9785	0.704
25.5	0.6	2.72	5700	10.5	7.36	1.66	1.58	18.1	1513	9984	0.681
25.7	0.1	2.72	5756	10.4	7.50	1.66	1.58	18.1	1514	9978	0.708

Bibliography

[1] European Union Aviation Safety Agency. “Updated analysis of the non-CO2 climate impacts of aviation and potential policy measures pursuant to EU Emissions Trading System Directive Article 30(4)”. In: Commission to the European Parliament and the Council (Brussels, Belgium, Nov. 23, 2020). 2020.

[2] Huseyin Ahmetoglu and Ridvan Saracoglu. “A Review of Multi Objective Optimization”. In: Conference: 3rd International Conference on Advanced Technology & Sciences (Konya, Turkey, July 1, 2016). 2016.

[3] Arora Arnadottir, Michał Czepkiewicz, and Jukka Heinonen. “Climate change concern and the desire to travel: How do I justify my flights?” In: *Travel Behaviour and Society* 24 (2021), pp. 282–290. DOI: 10.1016/j.tbs.2021.05.002.

[4] S. Barrett et al. *Guidance on the Use of AEDT Gridded Aircraft Emissions in Atmospheric Models.* US Federal Aviation Administration, 2010.

[5] Koen Barten. “Contrail mitigation through flight planning K.P.” MA thesis. Delft University of Technology, 2017.

[6] N. Baudoui. “Aerosol-Cloud Interaction”. In: *Encyclopedia of Atmospheric Sciences (Second Edition)* (2015), pp. 76–85. DOI: 10.1016/B978-0-12-382225-3.00054-2.

[7] Nasir Bilal. *Implementation of Sobol’s Method of Global Sensitivity Analysis to a Compressor Simulation Model*. International Compressor Engineering Conference, 2014.

[8] Loïc Brevault, Mathieu Balesdent, and Jérôme Morio. *Aerospace System Analysis and Optimization in Uncertainty*. Springer Optimization and Its Applications. Springer, 2020. ISBN: 978-3-030-39125-6.

[9] KV. Calvin et al. “RCP4.5: a pathway for stabilization of radiative forcing by 2100”. In: *Climatic Change* 109 (2011), pp. 77–94. DOI: 10.1007/s10584-011-0151-4.

[10] N. Chandrasekaran and Abhijit Guha. “Study of Prediction Methods for NOx Emission from Turbofan Engines”. In: *JOURNAL OF PROPULSION AND POWER* 28.1 (2012), pp. 27–58. DOI: 10.2514/1.B34245.

[11] K. Dahlmann et al. “Climate-Compatible Air Transport System—Climate Impact Mitigation Potential for Actual and Future Aircraft”. In: *Aerospace* 3 (2016), p. 38. DOI: 10.3390/aerospace3040038.

[12] Kalyanmoy Deb et al. “A Fast and Elitist Multiobjective Genetic Algorithm: NSGA-II”. In: *IEEE Transactions on Evolutionary Computation* 6.2 (2002), pp. 182–197. DOI: 10.1109/4235.996017.

[13] David Duda and Patrick Minnis. “Basic Diagnosis and Prediction of Persistent Contrail Occurrence Using High-Resolution Numerical Weather Analyses/Forecasts and Logistic Regression. Part I: Effects of Random Error”. In: *Journal of Applied Meteorology and Climatology* 48 (2009), pp. 1770–1788. DOI: 10.1175/2009JAMC2056.1.

[14] C.J. Eyers et al. *AERO2k Global Aviation Emissions Inventories for 2002 and 2025*. Deutsches Zentrum für Luft- und Raumfahrt, 2005.

[15] Jianqing Fan. *ORF 245: Fundamentals of Statistics*. Princeton University, 2020.

[16] Sarah J. Freeman. *Examining the Effects of Aviation NOx Emissions as a Short-Lived Climate-Forcer*. Manchester Metropolitan University, 2017.

[17] Jan S. Fuglestvedt et al. *Metrics Of Climate Change: Assessing Radiative Forcing And Emission Indices*. CICERO – Center for International Climate and Environmental Research, 2003.

[18] V. Grewe and A. Stenke. “AirClim: an efficient tool for climate evaluation of aircraft technology”. In: *Atmos. Chem. Phys.* 8 (2008), pp. 4621–4639.

[19] Volker Grewe. “Climate Impact of Air Traffic: Part IV”. In: *Tu Delft AE4462-17 Lecture Series* 4 (2021).

[20] Volker Grewe. “Climate Impact of Air Traffic: Part V”. In: *Tu Delft AE4462-17 Lecture Series* 5 (2021).

[21] Volker Grewe et al. *Climate impact evaluation of future green aircraft technologies*. Delft University of Technology, 2016.

[22] Marek W. Gutowski. “Leading Edge Computer Science Research”. In: Nova Science Publishers, 2005. Chap. Biology, Physics, Small Worlds and Genetic Algorithms.

[23] Brian Hayes. *Orderly Randomness - Quasirandom Numbers and Quasi-Monte Carlo*. IACS Seminar. 2015.

[24] Zhao Huan et al. “Introducing Robustness in Multi-Objective Optimization”. In: *Evolutionary Computation* 14.4 (2006), pp. 463–494. DOI: 10.1162/evco.2006.14.4.463.

[25] Zhao Huan et al. “Review of Robust Aerodynamic Design Optimization for Air Vehicles”. In: *Computational Methods in Engineering* 26 (2019), pp. 685–732. DOI: 10.1007/s11831-018-9259-2.

[26] Ruichen Jin, Xiaoping Du, and Wei Chen. “The Use of Metamodeling Techniques for Optimization Under Uncertainty”. In: *Structural and Multidisciplinary Optimization* 25.2 (2003), pp. 99–116. DOI: 10.1007/s00158-002-0277-0.

[27] Dahlmann K. et al. “Can we reliably assess climate mitigation options for air traffic scenarios despite large uncertainties in atmospheric processes?” In: *Transportation Research Part D* 46 (2016), pp. 40–55. DOI: 10.1029/2004JD004759s.

[28] Zoran S. Kapelan, Dragan A. Savic, and Godfrey A. Walters. “Multiobjective design of water distribution systems under uncertainty”. In: *Water Resources Research* 41 (2005). DOI: 10.1029/2004WR003787.

[29] Bernd Kärcher. “Formation and radiative forcing of contrail cirrus”. In: *NATURE COMMUNICATIONS* 9.1824 (2018). DOI: 10.1038/s41467-018-04068-0.

[30] Emre Kazancioglu et al. “Robust Optimization of an Automotive Valvetrain Using a Multiobjective Genetic Algorithm”. In: *Proceedings of the ASME Design Engineering Technical Conferences* (2003), pp. 97–108. DOI: 10.1115/DETC2003/DAC-48714.

[31] Andy J. Keane, Nair Prasanth, and Shahrokh Shahpar. “Robust Design of Compressor Fan Blades Against Erosion”. In: *Journal of Mechanical Design* 128.4 (2006), pp. 864–874. DOI: 10.1115/1.2202886.

[32] Brian Y. Kim et al. “System for assessing Aviation’s Global Emissions (SAGE), Part 1: Model description and inventory results”. In: *Transportation Research Part D* 12 (2007), pp. 325–346. DOI: 10.1016/j.trd.2007.03.007.

[33] Marcus O. Kohler et al. “Impact of perturbations to nitrogen oxide emissions from global aviation?” In: *JOURNAL OF GEOPHYSICAL RESEARCH* 113 (2008). DOI: 10.1029/2007JD009140.

[34] Abdullah Konak, David Coit, and Alice Smith. “Multi-objective optimization using genetic algorithms: A tutorial”. In: *Reliability Engineering and System Safety* 91 (2006), pp. 992–1007. DOI: 10.1016/j.ress.2005.11.018.

[35] Ian Kroo and Nicolas Antoine. “A Framework for Aircraft Conceptual Design and Environmental Performance Studies”. In: *AIAA Journal* 43.10 (2005), pp. 2100–2109. DOI: 10.2514/1.13017.

[36] D.S. Lee et al. “Aviation and global climate change in the 21st century”. In: *Atmospheric Environment* 43 (2009), pp. 3520–3537. DOI: 10.1016/j.atmosenv.2009.04.024.

[37] D.S. Lee et al. “The contribution of global aviation to anthropogenic climate forcing for 2000 to 2018”. In: *Atmospheric Environment* 244.117834 (2021). DOI: https://doi.org/10.1016/j.atmosenv.2020.117834.

[38] D.S. Lee et al. “Transport impacts on atmosphere and climate: Aviation”. In: *Atmospheric Environment* 44 (2010), pp. 4678–4734. DOI: 10.1016/j.atmosenv.2009.06.005.

[39] Joosung J. Lee et al. “System for assessing Aviation’s Global Emissions (SAGE), Part 2: Uncertainty assessment”. In: *Transportation Research Part D* 12 (2007), pp. 381–395. DOI: 10.1016/j.trd.2007.03.006.

[40] Dan Liu et al. “Considerations and Caveats when Applying Global Sensitivity Analysis Methods to Physiologically Based Pharmacokinetic Models”. In: *The AAPS Journal* 22.93 (2020), pp. 1–13. DOI: 10.1208/s12248-020-00480-x.

[41] Stephen P. Lukachko and Ian A. Waltz. *Effects of Engine Aging of Aircraft NOx Emissions*. Massachusetts Institute of Technology, Aero-Environmental Research Laboratory, 1997.

[42] Anuja Mahashabde et al. “Assessing the environmental impacts of aircraft noise and emissions”. In: *Progress inAerospaceSciences* 47 (2011), pp. 15–52.

[43] Karen Marais et al. “Assessing the impact of aviation on climate”. In: *Meteorologische Zeitschrift* 2.2 (2008), pp. 157–172. DOI: 10.1127/0941-2948/2008/0274.

[44] Karen Marais et al. “Overview of Greenhouse Gases”. In: *Meteorologische Zeitschrift* (2021). URL: https://www.epa.gov/ghgemissions/overview-greenhouse-gases.

[45] T. Masui et al. “An Emission Pathway for Stabilization at 6 W/m2 Radiative Forcing”. In: *Climatic Change* (2011). DOI: 10.1007/s10584-011-0150-5.

[46] Sigrun Matthes et al. “Effect of contrail overlap on radiative impact attributable to aviation contrails”. In: *Aerospace* 7.156 (2020). DOI: 10.3390/aerospace7110156.

[47] Georgios Mavromatidisa, Kristina Orehouniga, and Jan Carmelieta. “Uncertainty and global sensitivity analysis for the optimal design of distributed energy systems”. In: *Applied Energy* 214 (2018), pp. 219–238. DOI: 10.1016/j.apenergy.2018.01.062.

[48] Malte S. Meinshausen et al. “The RCP greenhouse gas concentrations and their extensions from 1765 to 2300”. In: *Climatic Change* 109 (2011), pp. 213–241. DOI: 10.1007/s10584-011-0156-z.

[49] TM Mohamed. *Fitting Probability Distributions of Annual Rainfall in Sudan*. Jazan University, 2015.

[50] Nadia A. Mohammed. “Comparing Halton and Sobol Sequences in Integral Evaluation”. In: *ZANCO Journal of Pure and Applied Sciences* 31 (2019), pp. 32–39. DOI: 10.21271/ZJPAS.31.1.5.

[51] Art B. Owen. “On dropping the First Sobol’ point”. In: *Stanford University* (2020). DOI: 2008.08051.

[52] Proesmans P. and Vos R. “Airplane Design Optimization for Minimal GlobalWarming Impact”. In: AIAA Scitech 2021 Forum (St. Gallen, Switzerland, Jan. 11–21, 2021). 2021.

[53] J.E. Penner et al. *Intergovernmental Panel on Climate Change Special Report*. Cambridge University Press, 1999.

[54] M. Ponater et al. “On contrail climate sensitivity”. In: *GEOPHYSICAL RESEARCH LETTERS* 32 (2005). DOI: 10.1029/2005GL022580.

[55] Michael Ponater et al. “Potential of the cryoplane technology to reduce aircraft climate impact: A state-of-the-art assessment”. In: *Atmospheric Environment* 40 (2006), pp. 6928–6944. DOI: 10.1016/j.atmosenv.2006.06.036.

[56] Gaby Radel and Keith P. Shine. “Radiative forcing by persistent contrails and its dependence on cruise altitudes”. In: *JOURNAL OF GEOPHYSICAL RESEARCH* 113 (2008). DOI: 10.1029/2007JD009117.

[57] K. Riahi et al. “RCP-8.5: Exploring the consequence of high emission trajectories”. In: *Climatic Change* (2011). DOI: 10.1007/s10584-011-0149-y.

[58] Martijn Roelofs and Roelof Vos. “Technology evaluation and uncertainty-based design optimization A review”. In: *AIAA Aerospace Sciences Meeting* 210059 ed. (2018). DOI: 10.2514/6.2018-2029.

[59] J. Roskam. “Airplane Design”. In: DARcorporation, 1985. Chap. Part VIII: Airplane Cost Estimation: Design, Development, Manufacturing and Operating.

[60] Inés Sanz-Morère et al. “Effect of contrail overlap on radiative impact attributable to aviation contrails”. In: *Atmospheric Chemistry and Physics* 21.3 (2021), pp. 1649–1681. DOI: doi.org/10.5194/acp-2020-181.

[61] R. Sausen et al. “Aviation radiative forcing in 2000: An update on IPCC (1999)”. In: *Meteorologische Zeitschrift* 14.4 (2005), pp. 555–561. DOI: 10.1127/0941-2948/2005/0049.

[62] ROBERT SAUSEN and ULRICH SCHUMANN. “Estimates Of The Climate Response To Aircraft Co2 And Nox Emissions Scenarios”. In: *Climatic Change* 44 (2000), pp. 27–58. DOI: 10.1023/A:1005579306109.

[63] U. Schumann. “The Impact Of Nitrogen Oxides Emissions From Aircraft Upon The Atmosphere At Flight Altitudes–Results From The Aeronox Project”. In: *Atmospheric Environment* 31.12 (1997), pp. 1723–1733. DOI: 10.1016/S1352-2310(96)00326-3.

[64] Ulrich Schumann. “On conditions for contrail formation from aircraft exhausts”. In: *Meteorologische Zeitschrift* 5 (1996), pp. 4–23. DOI: 10.1127/metz/5/1996/4.

[65] Emily Schwartz Dallara and Kroo Ilan M. “Metric for Comparing Lifetime Average Climate Impact of Aircraft”. In: *AIAA JOURNAL* 49.8 (2011). DOI: 10.2514/1.J050763.

[66] Mohammad Reza Setayandeh. “Surrogate Model–Based Robust Multidisciplinary Design Optimization of an Unmanned Aerial Vehicle”. In: *J. Aerosp. Eng.* 24.4 (2021). DOI: 10.1061/(ASCE)AS.1943-5525.0001272.

[67] William C Snyder. “Accuracy estimation for quasi-Monte Carlo simulations”. In: *Mathematics and Computers in Simulation (MATCOM)* 54.1 (2000), pp. 131–143. URL: https://EconPapers.repec.org/RePEc:eee:matcom:v:54:y:2000:i:1:p:131-143.

[68] S. Solomon et al. *Climate change 2007. The physical science basis*. Cambridge University Press, 2007.

[69] M.E.J. Stettler, S. Eastham, and S.R.H. Barrett. “Air quality and public health impacts of UK airports. Part I: Emissions”. In: *Atmospheric Environment* 45 (2011), pp. 5415–5424. DOI: 10.1016/j.atmosenv.2011.07.012.

[70] T.F. Stocker et al. *Climate Change 2013: the Physical Science Basis, Contribution of Working Group I to the Fifth Assessment Report of the Intergovernmental Panel on Climate Change*. Cambridge University Press, 2013.

[71] N.T. Thomopoulos. “Lecture 20: Bivariate Lognormal”. In: *Statistical Distributions* (2017). DOI: 10.1007/978-3-319-65112-5_20.

[72] S.F.G. Van Haver and R. Vos. *A Practical Method for Uncertainty Analysis in the Aircraft Conceptual Design Phase*. Delft University of Technology, 2014.

[73] A. Voulgarakis et al. “Analysis of present-day and future OH and methane lifetime in the ACCMIP simulations.” In: *Atmos. Chem. Phys.* 13 (2013), pp. 2563–2587. DOI: 10.5194/acp-13-2563-2013.

[74] DP van Vuuren et al. “RCP2.6: exploring the possibility to keep global mean temperature increase below 2°C”. In: *Climatic Change* (2011). DOI: 10.1007/s10584-011-0152-3.

[75] Qi Wang et al. “Parameterization of NSGA-II for the Optimal Design of Water Distribution Systems”. In: *Water* 11.971 (2019), pp. 1–14. DOI: 10.3390/w11050971.

[76] Ruihua Wang. “An Improved Nondominated Sorting Genetic Algorithm for Multiobjective Problem”. In: *Mathematical Problems in Engineering* 103 (2016), pp. 1–7. DOI: 10.1155/2016/1519542.

[77] Zhiyuan Wang and Gade Pandu Rangaiah. “Application and Analysis of Methods for Selecting an Optimal Solution from the Pareto-Optimal Front obtained by Multiobjective Optimization”. In: *Industrial Engineering and Chemical Research* 56 (2017), pp. 560–574. DOI: 10.1021/acs.iecr.6b03453.

[78] Gillian Mary Whelan et al. “The use of meteorological data to improve automated contrail detection in satellite imagery over Ireland”. In: Transport, Atmosphere and Climate Conference (Leicester, uk, Sept. 8, 2009–Sept. 11, 2021). 2009.

[79] Don Wuebbles et al. “Issues and Uncertainties Affecting Metrics for Aviation Impacts on Climate”. In: *AMERICAN METEOROLOGICAL SOCIETY* 49.8 (2010). DOI: 10.1175/2009BAMS2840.1.

[80] Jiaoshen Xu et al. “NSGA-II algorithm-based LQG controller design for nuclear reactor power control”. In: *Annals of Nuclear Energy* 169 (2022). DOI: 10.1016/j.anucene.2021.108931.

[81] Kais Zaman, Mark McDonald, and Sankaran Mahadevan. “Robustness-based design optimization under data uncertainty”. In: *Structural and Multidisciplinary Optimization* (2011). DOI: 10.1007/s00158-011-0622-2.

[82] Jiaxin Zhang. *Modern Monte Carlo Methods for Efficient Uncertainty Quantification and Propagation: A Survey*. Computer Science and Mathematics Division, Oak Ridge National Laboratory, 2020.

[83] X.-Y. Zhang et al. “Sobol Sensitivity Analysis: A Tool to Guide the Development and Evaluation of Systems Pharmacology Models”. In: *CPT: Pharmacometrics and Systems Pharmacology* 4.6 (2015). DOI: 10.1002/psp4.6.

[84] Changxin Zhu et al. “Uncertainty and its driving factors of airport aircraft pollutant emissions assessment”. In: *Transportation Research Part D* 94 (2021), pp. 1–17. DOI: 10.1016/j.trd.2021.102791.

[85] Eckart Zitzler and Lothar Thiele. “Multiobjective Evolutionary Algorithms: A Comparative Case Study and the Strength Pareto Approach”. In: *IEEE Transactions on Evolutionary Computation* 3.4 (1999), pp. 257–272. DOI: 10.1109/4235.797969.